学位論文

Structure and Formation Mechanism of Lead Perovskite Crystals

（鉛ペロブスカイト結晶の構造と形成機構）

平成 27 年 12 月博士（理学）申請

東京大学大学院理学系研究科

化学専攻

庄山 和隆

Abstract

The process where elements construct materials is a fascinating moment for materials scientists. In this thesis I will present unraveling of a crystal-to-crystal conversion, using methylammonium lead triiodide, normally called as lead perovskite, which is recently used as the photoactive layer of thin-film solar cells. The material itself is fascinating, allowing us to fabricate solar cells with > 20% power conversion efficiencies with a simple solution process. Yet, the course of action where elements construct the rigid framework remains elusive, obstructing scientists who are working on practical application of the material. The key finding in this thesis is puzzling out the whole chemical pathways during the conversion of lead(II) iodide and methylammonium iodide to lead perovskite. This information will serve as a milestone for those who are trying to solve reproducibility problem or morphology control of lead perovskite solar cells, further encourage scientists rationally design fabrication protocols, and most importantly contribute to the chemistry of solid-state reactions of various crystalline materials.

Acknowledgements

I here give my sincerest gratitude to Professor Eiichi Nakamura for his strict and critical advice throughout six years I spent under his guidance. His straightforward and tenacious approach encouraged me tackle difficult and arduous problems during my thesis research.

I could not complete this research without help from Dr. Yunlong Guo and Dr. Wataru Sato, thus hereby I give my deep appreciation to them. Their contribution to device fabrication as well as daily discussions were a necessary part of my thesis research.

I appreciate Professor Yutaka Matsuo for giving me instructions on X-ray crystallographic analysis, which include advice on displaying three-dimensional crystallographic data elegantly for easy understanding and formatting processes of CIFs.

In some of the experiments of IR and X-ray measurement I asked assistance from equipment manufacturers, Rigaku Corporation and JASCO Corporation. I thank Mr. Masaru Sudo from Rigaku Corporation for organizing measurement of reciprocal space mapping experiments with a hybrid pixel array detector. Technical staff in the company supported the measurement, thus I thank Dr. Takayuki Konya and Mr. Yuji Shiramata. Regarding IR measurement, I thank Ms. Hitomi Shiratori from JASCO Corporation for giving me some instructions on improving the data quality of IR spectra.

I had a chance to have valuable review comments from professors with various experiences to improve this thesis. In this regard, I show my appreciation to Professor Hiroshi Nishihara, Professor Hiroyuki Kagi, Professor Yasuhiro Yamashita, and Professor Shohei Tashiro. Their advice brought significant improvements to this thesis.

It was necessary for me to have close friends to whom I can talk freely on scientific questions as well as other personal issues. Thus I thank Dr. Naiti Lin, Dr. Emel Ay-Albrecht, Dr. Nopporn Ruangsupapichat, Dr. Shou-Fei Zhu, Dr. Qifan Yan, Dr. Rui Shang, and Dr. Lars Mattias Andersson.

Senior members in the lab often gave me various types of advice and instructions that arise from their professional experiences, thus I thank Dr. Hayato Tsuji, Dr. Koji Harano, Dr. Shunsuke Furukawa, Dr. Hideyuki Tanaka, and Dr. Laurean Ilies. I have also received assistance from the lab secretary thus I thank Mrs. Akemi Maruyama for her kind support.

Materials Education Program for the Future Leaders in Research, Industry, and Technology (MERIT) offered me a number of opportunities for acquiring a wide variety of knowledge over various disciplines, scientific communications, and expanding human relationship in the research and development field, as well as financial support. Thus here I thank the program director Professor Toshihiko Koseki, and program coordinator Professor Masashi Kawasaki. I am grateful for having had an instructor with whom I could have extra

discussion through this program, thus I thank Professor Takuzo Aida for his advice on my research as well as discussions on other non-research subjects.

Professor Frank Würthner hosted me as a visiting student for four months under the support of one of the course activities the MERIT program. I thank him for his generous support, giving me instructions on his chemistry, and providing nice arrangement over the four month of my stay. Regarding this I thank Dr. Matthias Stolte, and Ms. Sabine Seifert for instructing laboratory procedures as well as daily discussion. I could stay healthy and feel confortable during my stay in Germany partly due to support from lab members with various professional experiences, thus I thank Dr. Takeshi Maeda, Dr. Soichiro Ogi, Dr. Gustavo Fernández, Dr. Pawaret Leowanawat, Dr. Tao He, Dr. Naveen Kumar Allampally, and Dr. Agnieszka Nowak-Król. I also thank other members for having nice time with me during four months.

I thank all lab members for creating a witty and funny atmosphere in the Physical Organic Chemistry Laboratory in the Hongo campus of The University of Tokyo, where I spend six years during 2010 to 2016. Regarding this I have to mention that I had tremendously helpful trivial or non-trivial scientific discussions as well as other generous support with/from the following members, Dr. Hiroshi Okada, Dr. Tsuyoshi Suzuki, and Mr. Yuki Itabashi, thus hereby I thank them.

Finally I would like to thank my parents, Satomi and Takashi Shoyama for their support.

Tokyo, December 2015

Kazutaka Shoyama

Table of Contents

Chapter 1.

General Introduction

1.1 Introduction

Assembling of elements into a useful material form is an important process of materials chemistry.[1] The way in which we perform this formatting varies for individual materials.[2-5] Here we can consider two types of processing. One is to make a certain compound, and the other is to shape it into a particular functional form. One of the examples of the first type of processing is synthesis of organic materials.[6-11] In this case we employ synthetic skills where we dissolve ingredients in a solvent, add reagents to induce a reaction for forming/cleaving bonds, and then extract and isolate the desired compound. In this process we isolate a solid or liquid, or occasionally gas, of discrete molecules. They themselves are sometimes used directory such as detergents, food additives, or paint. They don't require post-synthesis process in which they are, for instance, forcibly confined in a limited space, deposited on a surface, or formed to nanoparticles. On the other hand in order to create more complicated materials we often need to fit compounds into a certain shape such as bulk solids, thin-films, or fine powders.[12-14] These operations are some of the examples of the second type of processing. Such application includes wafers, solar cells, and pharmaceutical drugs.

In any case, the information how elements move in the process of molding a particular material form is both scientifically and practically important. In organic chemistry, scientists pursue the details of how elements change their partners. In the course of such studies researchers have isolated intermediate species from the reaction mixture and determined their structures. Such structural information, when combined with kinetic or computational studies, can help researchers to obtain knowledge on possible reaction pathways. In such a way, in a number of cases we know how each reagent reacts on the substrate and in what order bonds form or cleave. This information leads to development of new reactions that give higher yields, better selectivity, and/or more environmental friendliness. On the other hand there is a paucity of information on reactions of crystalline inorganic solids. When we consider such reactions we most likely simply use diffusion theory. Since it happens in a solid, isolation of intermediates like organic reactions' case is scares.

In this thesis I will describe some details of a material formatting process that involves a crystal-to-crystal conversion reaction.[15-18] The focus of such study should be on a stereotypical and attractive material and also accompanied with suitable analysis methods. As such, I chose an inorganic-organic hybrid material, namely lead perovskite, which has the widely occurring perovskite crystal structure, and is envisaged as being used for renewable energy source. Focusing this material, I will elucidate the whole chemical pathways in which it is formed using X-ray diffraction analysis, which is a useful method for solid materials, as the key tool.

As I discussed earlier we should consider the difference of following two things, the creation of materials by simple bond formation/cleavage, and the process of forming materials into a certain shape. In the case of lead perovskite, the bond formation/cleavage process and shaping process take place at the same time. This makes the application of lead perovskite extremely difficult. The lack of chemical information has made the use of this material rather empirical and less practical. I conducted chemistry-oriented studies on lead perovskite to understand the process where each element is combined into a certain formula and fit into a certain shape.

1.2 Lead perovskite solar cells

In order to focus more on lead perovskite, I start from describing the structure of lead perovskite. The word perovskite itself denotes the crystallographic structure that employs a cubic or pseudo-cubic lattice, in which three components are placed. The chemical formula is usually presented as ABX_3, where A or B denotes a cation, and X denotes an anion. There are various combinations of components that give perovskite crystal structure both in nature[19-21] and materials science.[22-27] Materials that have perovskite structure have been appearing in a number of research topics including superconductors, ferroelectric materials, and various magnetic materials.[28] The perovskite material discussed here is almost exclusively a particular type of perovskite that is mostly used in thin-film solar cells, namely methylammonium lead triiodide ($CH_3NH_3^+PbI_3^-$; $MA^+PbI_3^-$; **PV**)[29] and its related formulae.

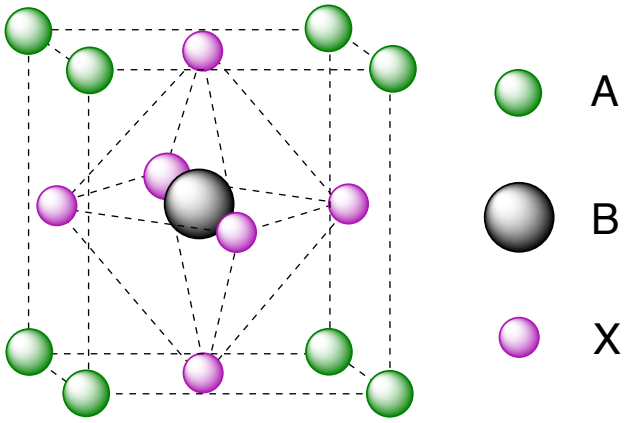

Figure 1.1. Crystal structure of perovskite.

These perovskites are first used in solar cells in 2009, reported by Miyasaka et al.[30] At this time the efficiency was around 4%, which is not much of practical value for commercial application. Then in 2012 several groups reported improved PCEs up to 12%.[31-34] Intense interest towards these materials increased the PCEs to more than 20% in 2015, which is comparable to several other types of promising solar cell technology.

There are a number of advantages of lead perovskites as an active material. They are reported to have high carrier diffusion lengths. This comes from their rigid inorganic

framework. In addition to excellent optoelectronic properties, lead perovskites are made from cheap materials such as simple amine and lead iodide (PbI_2; **PI**). This is a tremendous benefit for industrial applications. Deposition process is also simple. It does not require high-temperature curing. Only an annealing process at 100°C is required. The thin-films of lead perovskites are often deposited by solution process using a polar solvent such as dimethylsulfoxide (DMSO) or *N*,*N*-dimethylformamide (DMF).

On the other hand, there are some drawbacks. Morphology control remains difficult, as well as low reproducibility issue. This is to some extent imaginable since they have rigid Pb-I-Pb cubic lattice framework, which is easily constructed by a low temperature process. Lead is a rather toxic element. It can replace hydroxyapatite of human bones so that intake of this element exhibits considerable health problems.

Apart from solar cell studies of lead perovskites, there have been already a number of studies on lead perovskite and other related perovskites. The isolation and structure determination was already reported in 1950s.[35] Then, some of the basic properties such as magnetic susceptibility, phase transition temperature, enthalpy, and entropy have been reported.[36-43] These studies give, though they were not intended for solar cell application, useful information on elucidating the material forming process of solar cell thin-films.

1.3 Aim of this study

In this thesis I describe the chemical pathways occurring in the formation of lead perovskite, which relate irreproducibility and morphology control in the solar cell fabrication, as well as stability of perovskite materials all together. The following is the brief story line of this thesis. The chemical pathways were first studied in solution state where crystals of intermediates are isolated. Then the focus goes to the chemical reactions taking place in the crystal-to-crystal conversion. This elucidates the reason for irreproducibility in terms of chemical pathways. The morphology control is still yet solved at this stage since this chemical pathway study is in solution and crystal state, and studies in the thin-film state are still yet describe. It will be further discussed later after discussion on other solid-state properties. The phase transition of perovskite material is further discussed in relation to the solar cell device stability. Finally, combining all the chemical data obtained, I will discuss crystallization pathway that explains ways to control morphology of lead perovskite thin-films.

The first problem that this thesis addresses is related to the bond forming/cleavage process in which lead perovskite is formed. In Chapter 2 is presented the base information of chemistry-oriented studies of lead perovskite. This is very closely related to reproducibility or morphology control of perovskite-based solar cells. Earlier reports state there are large variations in the performance of perovskite-based solar cells. This issue would become

clearer if one would take a closer look on the chemistry behind this new technique, and if we consider large structural changes during the formation of lead halide perovskite solid. Common solution processes employ a mixture of lead(II) halide and ammonium salt and coat it on a surface.

The problem that comes next is stability. Some reports say that moisture can degrade lead halide perovskites. To our confusion, there are some reports that say the presence of moisture enhances the performance of solar cells based on lead perovskite. This dichotomy raises again a question of how this occurs. There have been several reports of the effect of water during the fabrication of solar cells. These reports well explain the effect of water from materials scientists' view; thoroughly scrutinized scanning electron microscopy (SEM) images that illustrate the improvement of morphology, photoluminescence studies that show enhanced luminescence thus more efficient charge collection. However the chemical picture of the effect still remains elusive. In Chapter 3 are presented the chemical pathways in the presence of water.

Concerning the stability issue, the phase transition of perovskite material will urge some explanations of the phase stability during operational conditions. The most commonly employed material, $CH_3NH_3PbI_3$, is known to undergo phase transition at 57 °C, which is in the range of solar cell operational conditions. In Chapter 4 will be presented phase stability of lead perovskite grains protected by a polymer polyvinylpyrrolidone (PVP) for enhancement of stability along with solar cell performance.

The utmost goal of the use of lead perovskite to solar cells would be to form a well-ordered single crystal thin-film on the substrate. For this purpose one needs to control the orientation and crystallization process. The clue to this goal will be presented in Chapter 5. Using the knowledge obtained in the solution study, by proper control of the solution film deposition process, well ordered dispersion of crystallites on flat substrates was achieved. There is also a prospect that the crystallite size can be enlarged by further control of the deposition process. This controlled deposition as well leads to improvement of solar cell performance.

The reproducibility issue and stability issue would certainly provoke concerns on the utilization of this class of materials into market. The long seller silicon solar cells have high stability and decent PCEs. The chemical information presented in this thesis will be combined together and conclusions on remaining tasks for us in this solar cell technology as well as pure scientific future views drawn by this thesis will be discussed in Chapter 6.

1.4 X-ray diffraction

In this study I frequently used various types of X-ray diffraction (XRD) technique. These include single crystal XRD analysis, fiber XRD analysis, thin-film XRD, and reciprocal space

mapping (RSM) of thin-films. I describe here some numerical and technical details that do not frequently appear in literature related to lead perovskite studies. Because of their frequent usage in literature in materials science field and availability of nicely arranged textbooks here I don't describe single crystal XRD analysis[44] and simple thin-film XRD analysis.[45] I here describe fiber XRD analysis (used in Chapter 2 and Chapter 3), the relationship of thermal factor and diffraction intensity (used in Chapter 4), and RSM (used in Chapter 5).

1.4.1 Fiber XRD analysis

Fiber XRD analysis is applied to, as it is named, fibers. The measurement configurations are similar to those of single crystal XRD and powder XRD. The notable difference is the dimensionality of the sample. In single crystal XRD the sample is fixed so that once you specify the three parameters of geometry of goniometer, the orientation of the sample is unique (the reason there are three parameters of the geometry is of course because the universe has three-dimensional space). In powder XRD it is not possible to get the orientation of the sample because there are multiple crystallites of random orientation. In fiber XRD, the fiber is set parallel to the rotation axis so that the diffraction occurring with respect to one of the crystallographic axes of the fiber is distinguished form that occurring with respect to other two axes. Thus fiber XRD, though not that much extent as single crystal analysis, can analyze the orientation of the fiber. Thus it gives more information than powder XRD analysis, but not as much as single crystal XRD analysis.

1.4.2 Variation of diffraction intensity by thermal factor

The diffraction intensity of X-ray is numerically calculated from the structure factor. However, the actual diffraction intensity is also dependent on other factors, such as thermal factor, and crystal mosaicity.[45] Here with regard to the discussions in following chapters, I describe the effect of atomic vibration on the intensity of diffraction

Unit cell structure factor of a scattering vector $\boldsymbol{q}$ is expressed as,

$$F^{\text{unit cell}}(\boldsymbol{q}) = \sum_j f_j(\boldsymbol{q}) e^{i\boldsymbol{q}\cdot\boldsymbol{r}_j}$$

where $\boldsymbol{r}_j$ refers to the position of atom j in the unit cell, $f_j(\boldsymbol{q})$ is the unit cell structure factor positioned at $\boldsymbol{r}_j$. When taking into account the atom vibration, it is expressed as,

$$F^{\text{unit cell}}(\boldsymbol{q}) = \sum_j f_j(\boldsymbol{q}) e^{-M_j} e^{i\boldsymbol{q}\cdot\boldsymbol{r}_j}$$

$$M_j = \frac{1}{2} q^2 \langle u_{q_j}^2 \rangle$$

where $\langle u_{q_j}^2 \rangle$ refers to temporal average displacement of atom j.

Thus even for the same degree of temporal average displacement the unit cell structure factor is lessen to a larger extent when the square of the scattering vector q^2 is higher. The

temporal average displacement is a measure of vibrational displacement of atoms, the unit cell structure factor is a measure of X-ray diffraction peak intensity, and the length of the scattering vector is correlated to diffraction angle in degree θ by $q = \left(\frac{4\pi}{\lambda}\right)\sin\theta$ where λ is the wavelength of X-ray used. Using these correlation the first sentence of this paragraph is equivalent to that as atom vibration becomes larger diffraction peaks at higher angles tend to lessen their intensity to larger extent than those at lower angles. This fact becomes important in the discussion in Chapter 4.

1.4.3 Reciprocal space mapping

X-ray diffraction serves as a useful tool for determining the orientation of materials formed as thin-films. There can be several measurement configurations, such as pole figure measurement, graze incident wide-angle X-ray scattering (GIWAXS), and reciprocal space mapping (RSM). Researchers in their distinctive fields have their own preference according to their research field. Pole figure measurement is used for thin-films that are two-dimensionally oriented thus need to know the exact orientation of the thin-film with respect to each of the two axes of the substrate.[46-48] GIWAXS is often used in the context of molecular assembly studies, in cases where molecules are ordered with respect to the normal of substrate but not to the axes parallel to the substrate.[49-53] RSM can gain similar information and have no draw back of blind region that occurs in the case of GIWAXS.[54-56] In the study in order to know the orientation of thin-films, this RSM was used.

In RSMs 2-D images of diffraction spots are presented. The scattering vectors lying along out-of-plane direction (q_z) occupy the *y*-axis of Cartesian coordinates, and those lying along in-plane direction (q_x) occupy the *x*-axis. The coordinate (x, y) corresponds to the diffraction intensity of (q_x, q_z). There is no blind region along the straight out-of-plane direction that present in GIWAXS patterns. This blind region comes from the incident angle of GIWAXS measurement, thus RSMs there is no such region because RSM measurement configuration does not require incident angle. This method is used in Chapter 5 for analysis of crystallite orientation of lead perovskite thin-films.

Chapter 2.

Chemical pathways that connect lead perovskite and lead(II) iodide via polymeric plumbate(II) fiber

2.1 Introduction

There is a significant difference between the structures of lead iodide (PbI_2; **PI)** and lead perovskite ($CH_3NH_3^+PbI_3^-$; $MA^+PbI_3^-$; **PV**). The crystal structure of **PI**[57] consists of two-dimensional (2-D) layered sheets of bipyramidal PbI_6 units. Each layer is separated from other layers by 6.8 Å. On the other hand the crystal structure of **PV** consists of cubic blocks of octahedral PbI_6 units that compose a three-dimensional (3-D) structure. There is any faint trace of 2-D layered structure of **PI** in **PV**, instead each cubic unit is separated by 6.3 Å to any of the three orthogonal basis directions of the crystal. For solar cell application, the conversion of 2-D **PI** to 3-D **PV** is accomplished by addition of methylammonium iodide ($CH_3NH_3^+I^-$; MAI) in the presence of a polar solvent, almost exclusively DMSO or DMF. The conversion process is simple. The reaction is in its chemical equation expressed as,

$$CH_3NH_3^+I^- + PbI_2 = CH_3NH_3^+PbI_3^-$$

A solution containing **PI** and MAI is deposited on a substrate and heated to 100 °C. The dramatic structural change occurs within less than an hour. This fact makes it easy to know that some of the problems concerning lead perovskite solar cells are reproducibility and morphology control. Earlier reports of lead perovskite solar cells suffered a large variation of performance.[58-60]

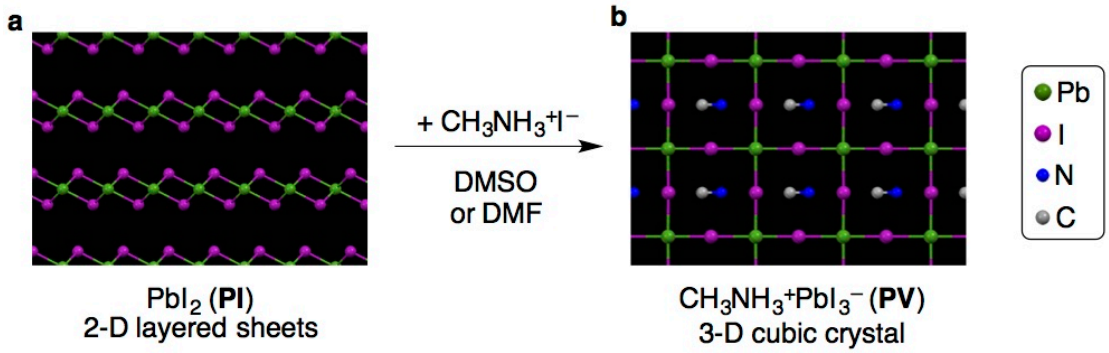

Figure 2.1. Crystal structures of **PI** and **PV**. **a**, 2-D layered sheets of **PI**. **b**, 3-D cubic crystal of **PV**.

There have been some clues that can help understand the chemical change during **PI** to **PV** conversion. There are some compounds containing substructures of **PI**, which are identified by crystallographic analysis. In 1980, far before **PV** was first applied to solar cells, a group of researchers isolated a polymeric strip of PbI_2 coordinated by DMSO.[61] The structure of PbI_2 unit of this complex is equivalent to diagonally cutting one $(PbI_2)_n$ unit of a bipyramidal PbI_2 sheet. In this regard, this structure can be categorized as one-dimensional (1-D) structure. After application of **PV** to solar cells is reported, some similar complexes were reported. These include a compound that possesses two $(PbI_2)_n$ units of bipyramidal PbI_2 coordinated by DMF[62] and that coordinated by iodine.[63] There is another complex only

characterized by infrared (IR) spectroscopy and elemental analysis, which was assigned as DMSO-PbI_2-MAI.[64] However, the connection of these complexes to **PI** or **PV** is still elusive.

In this chapter I will discuss the relationships between **PI** and **PV** connected by intermediate species that occurs in standard conditions of solar cell fabrication. The intermediated species possesses 1-D structures that are at the same time substructures of **PI**. Some of them are characterized for the first time in this work, and some others are reported previously by other researchers. The key discovery here is that atom movement during the conversion from **PI** to **PV** was solved for a freestanding intermediate crystal of **PV**. This is not merely a mechanistic study of this particular conversion, rather dubbed as mechanistic study of a crystal-to-crystal conversion where 2-D structure is converted to 3-D structure via 1-D structure. The information obtained here is further discussed in Chapter 3 for water system and Chapter 5 for film deposition process, and the perspective of the thesis is described in Chapter 6.

2.2 Results and discussion

2.2.1 Synthesis of intermediates and their inter-conversions

Synthesis of intermediates was performed in two solvent systems, DMSO and DMF. They are, for solar cell application, almost exclusively used. In early stages of solar cell application γ-butyrolactone (GBL) was also used, however, this solvent system is not used in recent reports.[30,33,58,65-68] The whole reaction is summarized in Figure 2.2. Intermediates shown in red boxes were characterized by X-ray crystallographic analysis previously by other researchers (**INT-1**, **-6**, **-7**) or for the first time in this work (**INT-2**, **-3**). Intermediates in blue boxes were assigned by fiber XRD study (*vide infra*). Most of the intermediates were isolated as fibrous crystals except **INT-1**, which had block crystal nature. The reactions in Figure 2.2 were traced by X-ray diffraction (XRD) patterns of resulting crystals (Figure 2.2c). Since DMF system is simpler than DMSO system this will be described first.

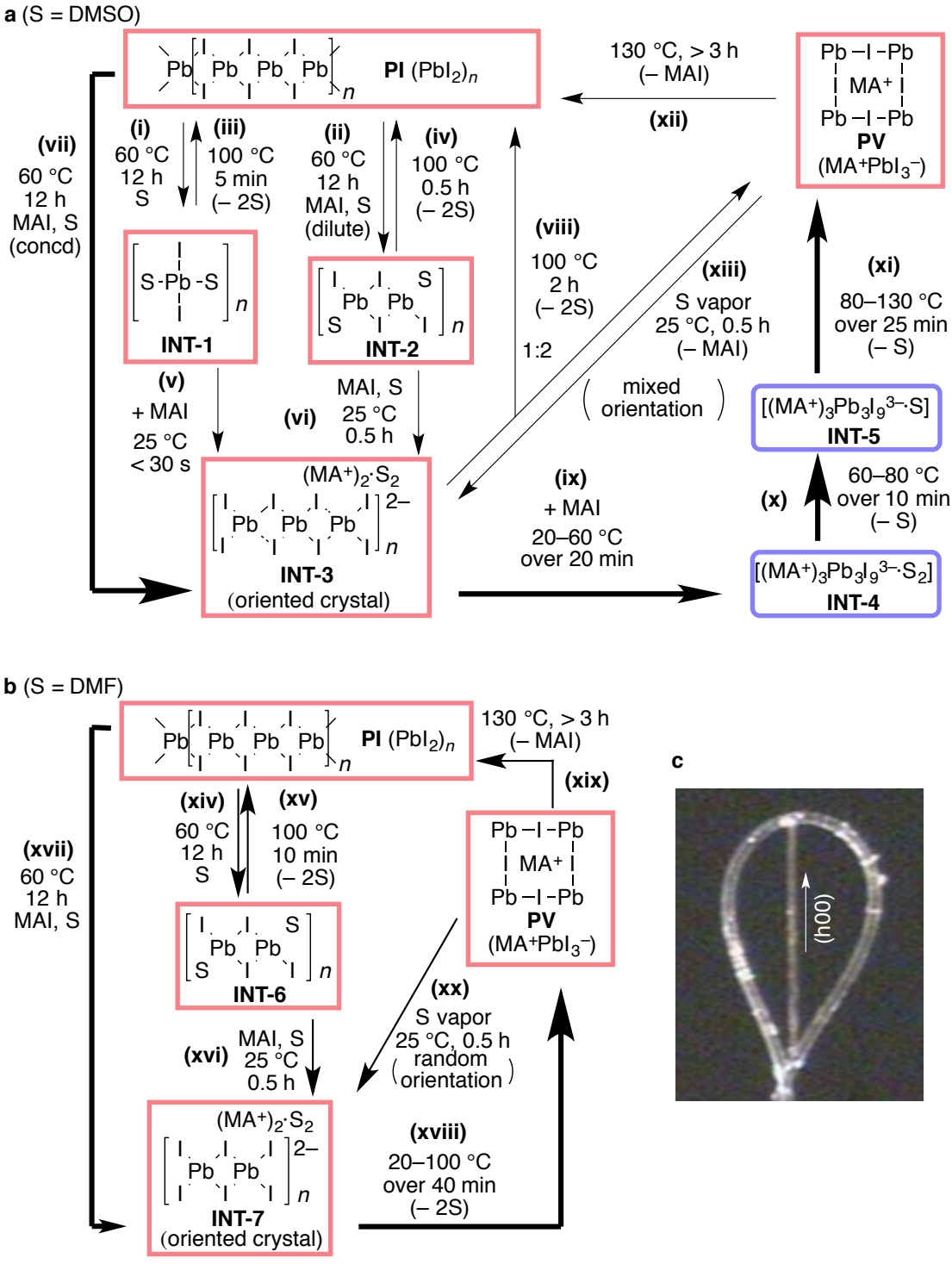

Figure 2.2. Chemical pathways in the inter-conversion of **PI** to **PV**. Pathways occurring in the solar cell fabrication conditions are shown by bold arrows. Compounds in red boxes are characterized by crystallographic analysis, those in blue boxes are characterized by fiber XRD analysis. **a**, DMSO system. **b**, DMF system. **c**, Optical microscopic image of **INT-3**.

Heating of a 30 wt% solution of **PI** in DMF at 60 °C subsequently cooled to room temperature produced di-nuclear plumbate **INT-6** ($(PbI_2)_2 \cdot DMF_2$) (Figure 2.2b, step xiv). Plumbate **INT-6** reverted to **PI** when heated at 100 °C by losing coordinating solvent

molecules (step xv). When **INT-6** was dipped in a solution of MAI in DMF it converted to another di-nuclear plumbate **INT-7** ($(MA^+)_2(PbI_3^-)_2{\cdot}DMF_2$), which is an iodine-coordinated version of **INT-6** (step xvi). Plumbate **INT-7** was also prepared in one step by heating of a 30 wt% solution of **PI** and MAI (1:1 mole ratio) in DMF at 60 °C subsequently cooled to room temperature (step xvii). Intermediates **INT-6** and **INT-7** had diameters ranging around several tens of micrometers. The chemical formula of **INT-7** has a ratio of lead and iodine equivalent to that of **PV**. This makes it easier to understand that heating of a fibrous crystal of **INT-7** at 100 °C produced a fibrous-shaped crystal of **PV** ($MA^+PbI_3^-$) (step xviii). The crystals of **PV** also decomposed to **PI** when heated at 130 °C rather gradually (step xix). An important finding is that when fibrous **PV** crystal was exposed to DMF vapor at room temperature it smoothly reverted to **INT-7** (step xx). This indicates that **INT-7** is the most stable chemical species in the system composed of an almost equivalent ratio of **PI** and MAI, and a necessary amount of DMF at room temperature. The quick conversion also indicates that these is close structural relationships between **PV** and **INT-7**, which I will discuss later in combination with fiber XRD patterns during the conversion to **PV**.

The chemical pathways in DMSO system are similar to DMF system except for a few important details. Heating of a 30 wt% solution of **PI** in DMSO/GBL (3:7 vol/vol ratio) at 60 °C subsequently cooled to room temperature produced block crystals of mono-nuclear plumbate **INT-1** ($PbI_2{\cdot}DMSO_2$) (Figure 2.2a, step i). In a similar manner, a 40 wt% solution of **PI** and MAI (mole ratio 1:1) produced di-nuclear plumbate **INT-2** ($(PbI_2)_2{\cdot}DMSO_2$) as fibrous crystals (step ii). Both of them reverted to **PI** upon heating at 100 °C by loss of coordinating solvent molecules (steps iii, iv). When **INT-1** was dipped in a solution of MAI in isopropyl alcohol it converted to tri-nuclear complex **INT-3** ($(MA^+)_2[(PbI_3^-)_2PbI_2]{\cdot}DMSO_2$), which has a polymeric structure of three consecutive PbI_2 units coordinated by two iodine atoms (step v). The same complex was obtained by coating **INT-2** with MAI and DMSO for a rather longer time than **INT-1** to **INT-3** conversion (step vi). The longer reaction time of **INT-2** to **INT-3** compared to **INT-1** to **INT-3** is possibly due to larger structural differences that make the conversion slower. Similar to the case of DMF system, **INT-3** was obtained in a single step from **PI** in the presence of MAI in a mixed solvent of DMSO/GBL (3:7 vol/vol ratio) (step vii). The chemical formula of **INT-3** ($(MA^+)_2[(PbI_3^-)_2PbI_2]{\cdot}DMSO_2$) consists of two equivalents of **PV** and one equivalent of **PI**. Thus when heated to 100 °C, **INT-3** converted to **PV** and **PI** with a ratio of 2:1 as evidenced by occurrence of XRD peaks of both compounds (step viii). When **INT-3** was supplied with MAI and heated to 100 °C it converted to **PV** without forming **PI** (step ix–xi). During this process two transient intermediates are observed in XRD patterns (**INT-4** and **INT-5**). This process was investigated in detail by fiber XRD analysis (*vide infra*). The obtained fibrous **PV** crystal decomposed to **PI** upon heating to 130 °C by loss of MAI (step xii). As is similar

to DMF system, fibrous **PV** crystals reverted to **INT-3** upon exposure to DMSO vapor at room temperature smoothly within 0.5 h (step xiii). This indicates that in DMSO system tri-nuclear complex **INT-3** is the most stable species in the presence of solvent.

2.2.2 Structures of chemical species occurring in PI to PV conversion

The structures of intermediate species have the trace of the features of the layered crystal structure of **PI**. The crystallographic structures of **PI** and intermediates are shown in Figure 2.3. Only two layers of polymeric plumbate are shown for each picture in Figure 2.3. The structure of **PI** consists of layers of $(PbI_2)_n$ sheets that compose the hexagonal crystal lattice. Each Pb–μ^2-I bond has a length of 2.98 Å. Plumbate **INT-1** is well described as mono-nuclear plumbate with each lead atom coordinated by two DMSO molecules. This corresponds to slicing one unit of PbI_2 from one $(PbI_2)_n$ layer of **PI** crystal. The Pb–I bond length of **INT-1**is 3.24 Å, which is slightly longer than **PI**, indicating loosening of Pb–I bonds due to absence of rigid bipyramidal covalent bonds as in the sheet of **PI** crystal. Plumbate **INT-2** is in the same manner described as di-nuclear plumbate with each terminal coordinated with DMSO molecules. The Pb–μ^2-I bond lengths are 3.30, 3.34 Å, the terminal Pb–I bond length is 3.16 Å, also indicating loosened nature of those bonds. Plumbate **INT-3** is different from **INT-1** and **INT-2** in the sense that it has no DMSO molecule directory coordinating to Pb center. Thus this compound is categorized as tri-nuclear plumbate coordinated with each terminal coordinated with an iodine atom. As such, in the crystal structure of **INT-3** tri-nuclear $[(PbI_3^-)_2PbI_2]$ structure does not coordinate with the sulfoxy group of DMSO and also separated from MA^+. Significantly longer Pb–μ^2-I bonds that connect one of the terminal and central lead atoms (3.47–3.49 Å) indicate weaker interatomic interaction that comes from dianionic nature of tri-nuclear plumbate. The two intermediates species of DMF system also has similar interactions in their crystal structures.

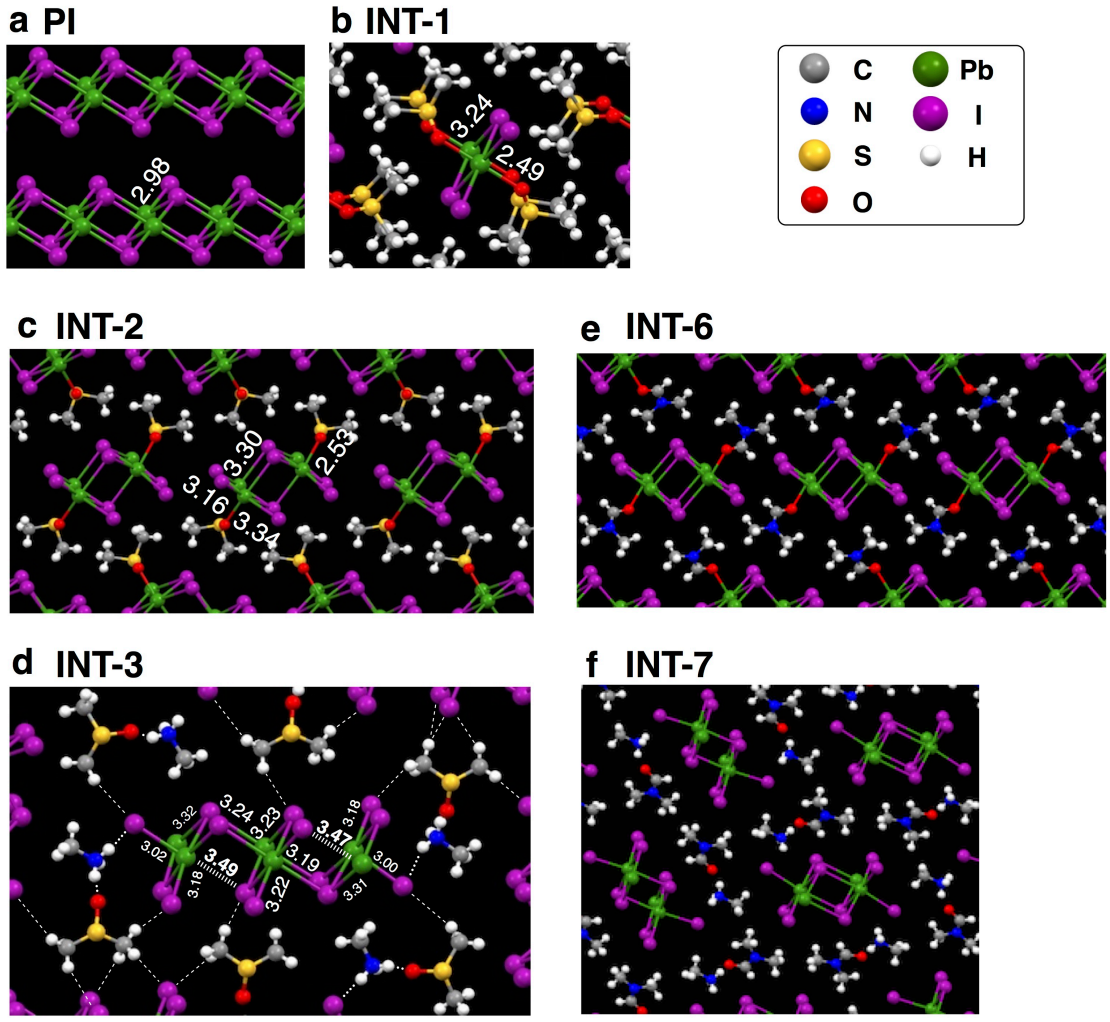

Figure 2.3. Crystallographic structures of **INT-1**–**3**, **-6**, **-7**. **a**, **PI**. **b**, **INT-1**. **c INT-2**. **d**, **INT-3**. **e**, **INT-6**. **f**, **INT-7**

There were found some differences between DMSO system and DMF system in the intermediate structures occurring in the chemical conversion. In order to discuss chemical structures, the complexes are categorized in terms of the number of lead atoms in each unit (mono-, di-, tri-nuclear) and coordinating molecules or atoms at both of the terminals of each unit (either iodide or solvent molecule). For instance, **INT-1** is a mono-nuclear complex coordinated with solvent molecules, and **INT-3** is a tri-nuclear complex coordinated with iodides. The differences between DMSO and DMF system in terms of this categorization is the occurrence of mono-nuclear complex in DMSO system, not in DMF in the same conditions, and occurrence of tri-nuclear complex coordinated with iodides in DMSO system instead of di-nuclear complex coordinated with iodides in DMF system. Seeing these facts one can propose the reason for these differences. It is that basicity of the solvent molecule differentiates the structural nature of possible complexes in the system. The basicity of solvent molecules can be estimated by their donor numbers.[69] The donor numbers of DMSO and DMF are 29.8 and 26.6, respectively. The higher donor number of DMSO destabilizes di-

nuclear complex **INT-2** by further coordinating it and produces mono-nuclear complex **INT-1**. The fact that tri-nuclear plumbate with iodide coordination (**INT-3**) is most stable in DMSO system is explained by the instability of di-nuclear counterpart due to electronic repulsion of negative charges that would enable DMSO molecules to coordinate to the terminal of it to produce **INT-2**.

2.2.3 Structural mapping of intermediates to PV

The facile inter-conversions of **INT-3** to **PV** and **INT-7** to **PV** indicate close structural relationship between them. An important clue to map atom motions is to know the correlation between initial crystal orientation of intermediates and that of resulting **PV** crystal. In the in-situ XRD analysis of the conversion of **INT-3** to **PV** it was shown that crystallographic *a*-axis, which is also the fiber axis, coincides with (110) normal of **PV** crystallographic lattice (discussed in section 2.2.4). This means that the direction along which tri-nuclear strips of plumbate in **INT-3** run corresponds to the (110) normal of **PV**. This correlation is shown in Figure 2.4. The crystallographic orientation of **INT-3** in Figure 2.4a corresponds to the orientation of **PV** in Figure 2.4b during the conversion of **INT-3** to **PV**. With this information on crystallographic orientation in hand one can deduce the whole atom movement during the conversion of **INT-3** to **PV**. In the bottom panel of Figure 2.4 are shown atom movements of 30 units of PbI_2 unit during the process of **PV** formation from **PI**. For ease of interpretation, in the figures only two layers of plumbate are shown, and iodine atoms are considered to follow the movement of lead atoms considering the lighter atomic weight of iodine compared to lead. In the process of **PI** to **INT-3**, the two layers of $(PbI_2)_n$ (30 units in total) shown in Figure 2.4d are either directory converted to the tri-nuclear plumbate strips of **INT-3** by addition of 20 MAI and 20 DMSO, or cut into pieces to yield mono-nuclear plumbate **INT-1** or di-nuclear plumbate **INT-2** and then to be converted to **INT-3** by addition of MAI. Figure 2.4e (the same region is shown in Figure 2.4a) shows the mapping of the tri-nuclear strips of **INT-3** onto the grid of the cubic lattice of **PV**. The cubic lattice is inclined by 45° laterally in accordance with the discussion on the orientation. During the conversion from **INT-3** to **PV**, each layer of the plumbate strip in Figure 2.4e is separated from other neighboring layers as shown by the arrows showing the motions of lead atoms to form two columns of consecutive three lead atoms (Figure 2.4f). At the same time the central lead atoms of tri-nuclear strips move along the fiber axis to form 45° between the terminal lead atoms (Figure 2.4g). This conversion occurs with addition of 10 MAI molecules and loss of 20 DMSO molecules. In the reverse process from **PV** to **INT-3**, two neighboring columns of three consecutive lead atoms come across together to form one column of tri-nuclear plumbate. This process is accompanied with loss of 10 MAI molecules and addition of 20 DMSO molecules.

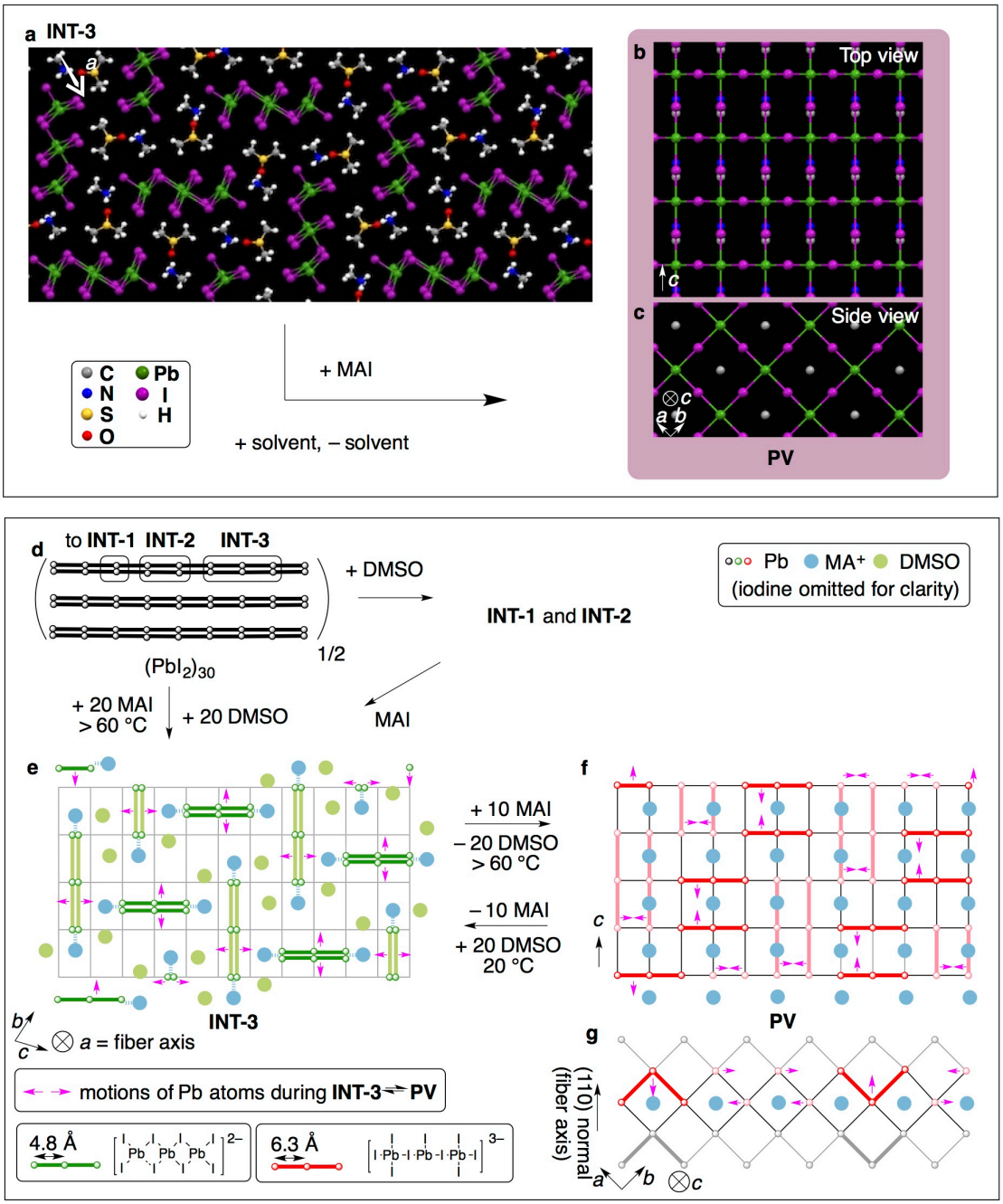

Figure 2.4. Structural correlation between **INT-3** and **PV**. Only two layers of plumbate is shown. (Top panel) Crystal structures of **INT-3** and **PV**. **a**, Crystal structure of **INT-3** seen along crystallographic *a*-axis, which runs along the fiber axis. **b**, Crystal structure of **PV** seen along the (110) normal. **c**, Seen along *c*-axis. (Bottom panel) Schematic images of **PI**, **INT-3**, and **PV** corresponding to the Top panel images. **d**, A selected area of **PI** layered crystal that converts to **INT-3** and **PV** shown in **Figure 2.4**e–g. **e**, **INT-3** mapped onto the cubic grid of **PV** in **Figure 2.4**f. **f**, The cubic lattice of **PV** that is inclined by 45° laterally. **g**, Side view of **Figure 2.4**f.

The same mapping can also be drawn for the DMF system (Figure 2.5). In this case the tri-nuclear strips that occurred in DMSO case is simply replaced with di-nuclear strips. There

is no addition of MAI during **INT-7** to **PV** conversion. Figure 2.5a and Figure 2.5b corresponds to the orientation correlation of the conversion. In Figure 2.5d–g are the atom movements of this conversion of a region of 30 units of PbI_2. The scheme is essentially the same as DMSO case except for difference of the number of lead atoms in the polymeric strips of each intermediate (**INT-3** or **INT-7**) and necessity of the supply of MAI.

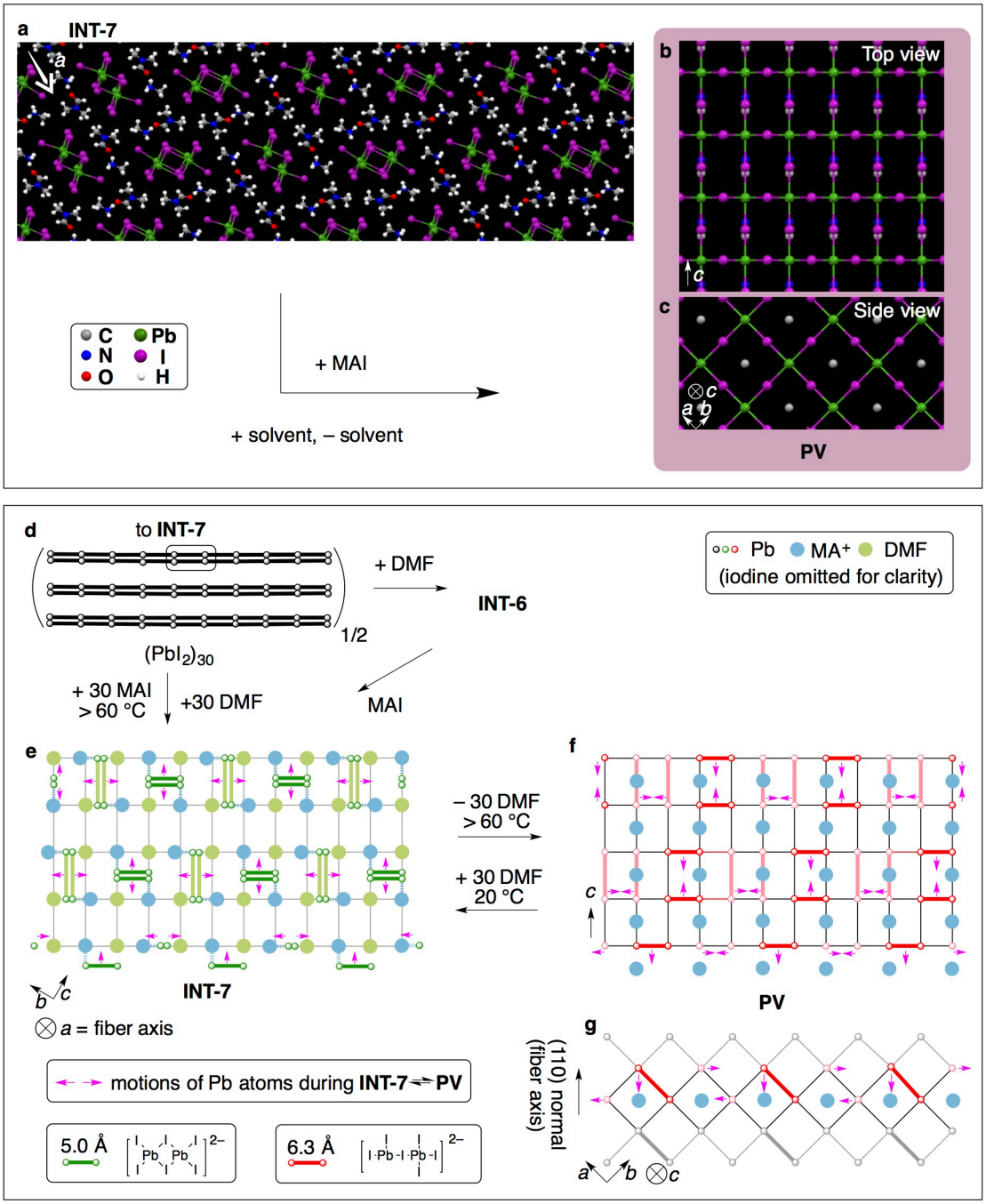

Figure 2.5. Structural correlation between **INT-7** and **PV**. Only two layers of plumbate is shown. (Top panel) Crystal structures of **INT-7** and **PV**. **a**, Crystal structure of **INT-7** seen along crystallographic *a*-axis, which runs along the fiber axis. **b**, Crystal structure of **PV** seen along the (110) normal. **c**, Seen along *c*-axis. (Bottom panel) Schematic images of **PI**, **INT-7**, and **PV** corresponding to the Top panel images. **d**, A selected area of **PI** layered crystal that

converts to **INT-7** and **PV** shown in **Figure 2.5**e–g. **e**, **INT-7** mapped onto the cubic grid of **PV** in **Figure 2.5**f. **f**, The cubic lattice of **PV** that is inclined by 45° laterally. **g**, Side view of **Figure 2.5**f.

Overall essentially the same reaction mechanism was found for two solvent systems, DMSO and DMF. This mapping is deduced based on the experimental fact that the fiber axis of **INT-7** and **INT-6** (which crystallographically corresponds to *a*-axis in both compounds) runs along the (110) normal of resulting **PV** crystal (section 2.2.4). This indicates that the resulting **PV** crystal has a crystallographic orientation that the cubic lattice inclined by 45° along the fiber axis. This will have a significant impact on the quality of the thin-films of **PV** obtained by solution process since different crystallographic orientations have different carrier transporting properties. This effect is further discussed in Chapter 5.

2.2.4 Fiber XRD analysis of conversions between intermediates and PV

Fiber XRD analysis[45] is a powerful method to study the anisotropic character of fibrous materials (see Section 1.4.1). Since fibers frequently occur in biological systems this method is occasionally performed for such compounds.[70] In fiber XRD analysis fibrous target material is held on a goniometer vertically. The sample was rotated during exposure to X-ray radiation. In this configuration the crystallographic planes running vertically against the ground give diffraction to lateral direction while those running horizontally give to vertical direction.

This method was used for in-situ measurement of the conversion between **INT-3** to **PV** or **INT-7** to **PV**. The measurement was performed for the temperature range of 20–130 °C for **INT-3** to **PV** conversion and 20–100 °C for **INT-7** to **PV** conversion (see Figure 2.2). The measurement temperature was gradually raised from 20 °C with a 10 °C step and 5 min interval.

Fiber XRD analysis revealed mainly four important facts of the conversion of intermediates (**INT-3** or **INT-7**) to **PV**. Fist of all, the correlation between the crystallographic orientation of initial **INT-3** or **INT-7** fibrous crystal and that of final fibrous **PV** is deduced. Secondly, the crystallographic orientation after the reversion of **PV** to **INT-3** or **INT-7** was investigated, the result of which needs careful description, as I will do later. Thirdly, the dependence of different solvent systems on the kinetics of the conversion was shown. In the forth place, in the case of DMSO system two transient intermediate species were observed (Figure 2.2a)

Figure 2.6a–d shows 2-D fiber XRD patterns during two cycles of **INT-3**–**PV** conversion. Figure 2.6a is the 2-D fiber XRD pattern of a bundle of **INT-3** fibers which were coated with MAI solution by capillary effect. The (0*kl*) diffractions such as (002), (021), and (022) were spotted on the horizontal line running through the center, indicating that the *a*-axis is running

vertically against the ground. The inset in Figure 2.6a shows Bravais, Friedel, Donnay and Harker (BFDH) crystal morphology of **INT-3** place in such orientation. When this fiber was heated to 100 °C it converted to **PV** and showed its (100) diffraction circle. On the circle were six high-intensity spots, two at the horizontal direction and four with 45° inclination. This indicates one of the three axes of cubic **PV** lattice runs along the horizontal line while other two running with 45° inclination against it. The inset of Figure 2.6 shows BFDH crystal morphology of **PV** lying in such orientation. Figure 2.6c shows 2-D fiber XRD pattern of **INT-3** fibers obtained by exposure of **PV** fibers to DMSO vapor at room temperature. On the diffraction circle of each of (002), (021), and (022) signals are four high-intensity spots. Two of them coincide with the horizontal line and other two with the vertical line. This fact indicates that the **INT-3** fibers obtained by reversion of **PV** partially run along the initial vertical direction and the other part along the horizontal direction. The inset of Figure 2.6c shows BFDH crystal morphology of **INT-3** under such condition. When **INT-3** obtained by reversion of **PV** was again heated to 100 °C it converted again to **PV** without any preferred orientation as it gave (100) diffraction circle without significant azimuthal intensity deviation.

Figure 2.6e–h shows the same experiment for a DMF fiber. Since **INT-7** to **PV** conversion does not require addition of MAI the fiber was not coated with MAI. Figure 2.6e shows 2-D fiber XRD pattern of a fibrous crystal of **INT-7**. The diffraction peaks of (0*kl*) such as (020), (011), and (021) were spotted on the horizontal line, indicating the same vertical orientation of the fiber as the DMSO fibers. When heated to 100 °C it converted to **PV** and showed (100) diffraction circle of the cubic crystallographic lattice. On the circle were eight high-intensity spots in contrast to six spots in the DMSO case. This indicates that resulting **PV** crystal has two orientations. One is the same as DMSO case as in the inset of Figure 2.6b, the other is **PV** cubic lattice laterally inclined by 45°. The inset of Figure 2.6f shows such two orientations. When reverted to **INT-7** by exposure to DMF vapor it lost crystallographic orientation completely and gave diffraction circles without azimuthal intensity deviation (Figure 2.6g). There was no orientation in the **PV** fiber obtained by heating regenerated **INT-7** (Figure 2.6h).

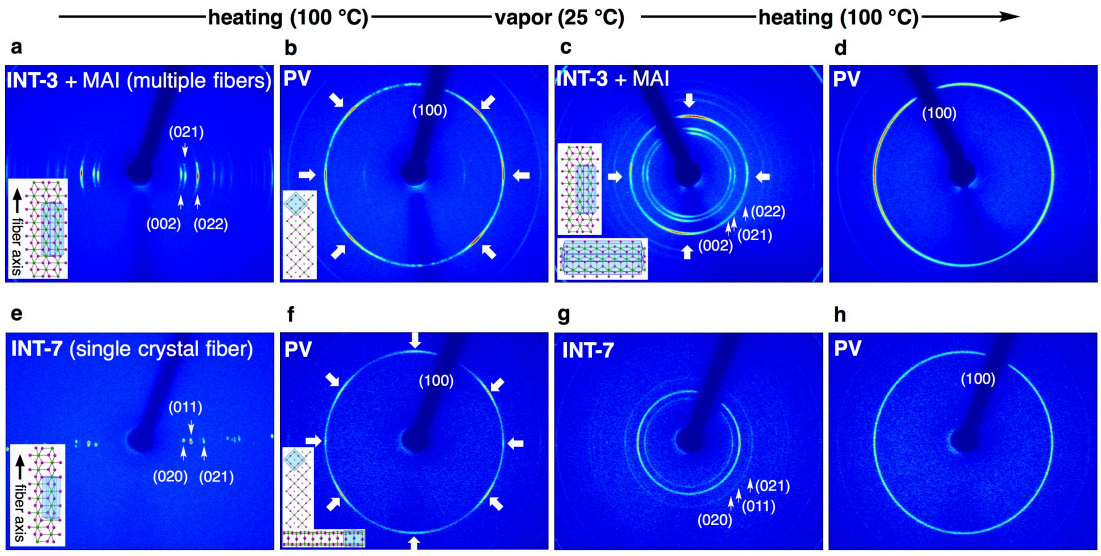

Figure 2.6. Fiber XRD patterns during the conversion of **INT-3** to **PV** and **INT-7** to **PV**. **a**, A bundle of multiple fibers of **INT-3** at 20 °C. **b**, **PV** obtained by heating of **INT-3** at 100 °C. **c**, **INT-3** fiber obtained by vapor exposure of a **PV** fiber. **d**, **PV** obtained by heating regenerated **INT-3**. **e**, **INT-7** fiber at 20 °C, **f**, **PV** obtained by heating of **INT-7**. **g**, **INT-7** fiber obtained by vapor exposure of a **PV** fiber. **h**, **PV** obtained by heating regenerated **INT-7**.

The differences of DMSO system and DMF system, namely the existence of two crystallographic orientations of **PV** obtained from **INT-7** (Figure 2.6f), and complete orientation loss of reverted **INT-7** (Figure 2.6g), help deduce the kinetic effect of solvent on the **PV** formation pathways. The two orientations of **PV** obtained from **INT-7** indicate that in this process of converting **INT-7** to **PV** the resulted **PV** during heating can revert to **INT-7** giving two different orientations as in the case of the reversion of **PV** to **INT-3** in DMSO system (Figure 2.6b to c). The fact that reverted **INT-7** by vapor exposure of **PV** has no orientation indicates that gradual deviation from the ideal orthogonal reversion orientation during the cycles of intermediate–**PV** inter-conversion occurred quicker than in the DMSO system. Those two experimental facts both suggest quicker intermediate–**PV** inter-conversion of DMF system compared to DMSO system. This is further supported by kinetic analysis of the **PV** formation process as described next.

Figure 2.7 shows kinetics of the conversions between **INT-3** and **PV**, and **INT-7** and **PV**. The kinetics in DMSO system is described first. Figure 2.7a shows 1-D XRD patterns during the conversion of **INT-3** to **PV**. Figure 2.7b shows intensity change at selected diffraction angles. When **INT-3** fibers were heated from 20 °C with a step of 10 °C for each 5 min, the (100) diffraction signal of **PV** appeared at 40 °C with a reduction of the intensity of **INT-3** peaks (2θ = 6.6, 7.1, and 9.2°). When further heated to 60 °C, an additional peak appeared at 2θ = 5.7°, indicating presence of a transient intermediate species. At 80 °C another peak appeared at 2θ = 7.9°, indicating presence of another transient intermediate species. These

transient intermediates occur during the evolution of **PV** diffractions signals, indicating that the conversion is composed of several element reactions that are governed by stepwise loss of solvent molecules under diffusion condition in the fibrous crystals. I note here passing by that the diffraction signals of these transient intermediates are sharp enough to support significant amount of these species are present in the crystals since a number of repeating units (> 100 nm, assuming from the limit of Scherrer's equation) The conversion completed at 130 °C. The conversion also completed at 100 °C when the sample was held at this temperature for an extended heating time (ca. 2 h). The same experimental conditions were used to monitor the conversion of **INT-7** to **PV** (Figure 2.7c, d). When heated from 20 °C, **PV** diffraction signal appeared at 60 °C. The conversion completed quickly when the temperature reached 100 °C. There was no transient intermediate species in DMF system.

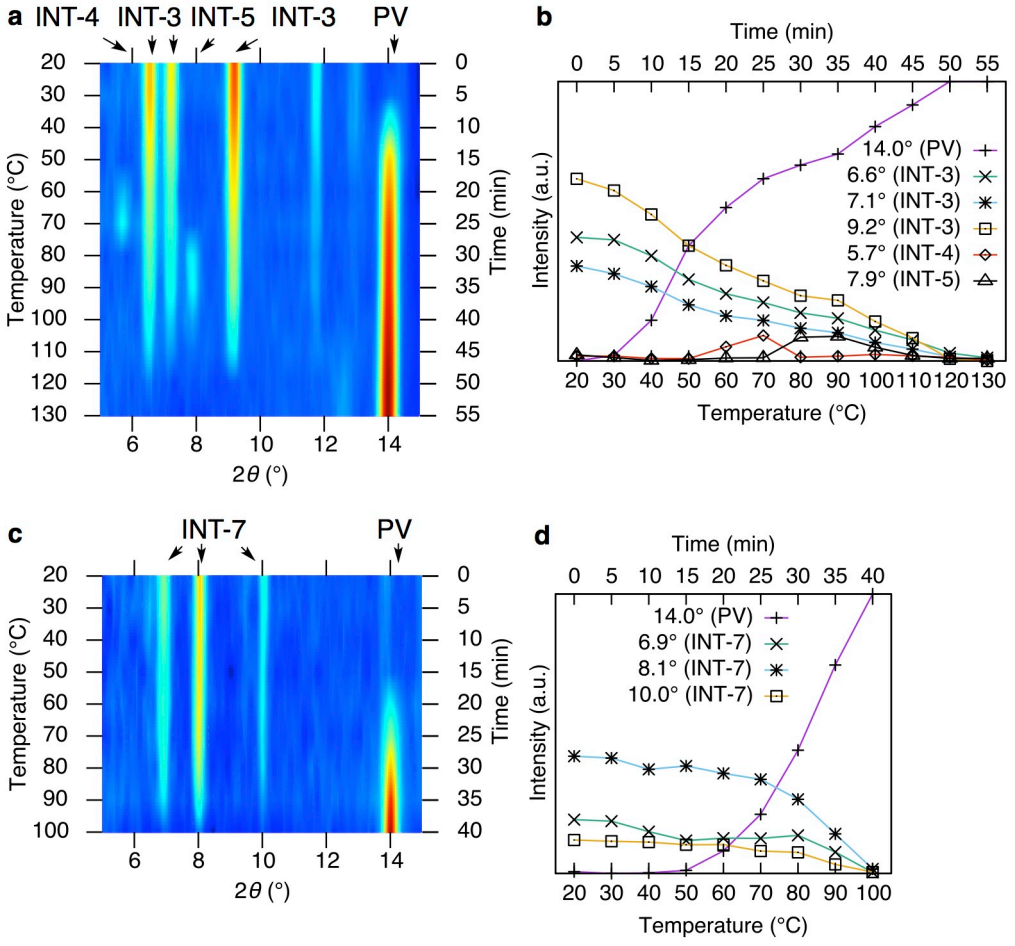

Figure 2.7. 1-D XRD traces of fiber XRD measurements in **Figure 2.6** and intensity profile at selected diffraction angles. **a**, VT fiber XRD measurement result of the conversion from **INT-3** to **PV**. **b**, Linear scale intensity profile at selected diffraction angles of **Figure 2.7**a. **c**, The same measurement data for **INT-7** to **PV** conversion as in **Figure 2.7**a. **d**, The profile of **Figure 2.7**c as in **Figure 2.7**a.

The quicker conversion of **INT-7** to **PV** than **INT-3** to **PV** (100 °C vs. 130 °C) indicates that this process is kinetically more facile. This experimental fact in the **INT-7** to **PV** conversion is in accordance with the occurrence of two orientations of **PV** in the first conversion cycle and complete orientation loss of **INT-7** regenerated by vapor treatment of **PV** fiber in this solvent system. In addition to these experimental results, the lower donor number of DMF compared to DMSO also supports quicker desorption of DMF from the plumbate crystal lattice.

The transient intermediates observed in DMSO system give some insight into the conversion process of **INT-3** to **PV**. Figure 2.8 shows 2-D fiber XRD patterns of two transient intermediates. The transient intermediate species that gives diffraction peak at 5.7° was named as **INT-4** and another one that gives a peak at 7.9° was named **INT-5**. Given that **INT-4** has lower angle diffraction than **INT-3** to a direction perpendicular to the *a*-axis, this transient intermediate has 0.18 nm longer cell lattice to a direction orthogonal to the *a*-axis than **INT-3**. This corresponds to diffusion of MAI into the crystal lattice of **INT-3** since **INT-3** ($(MA^+)_2[(PbI_3^-)_2PbI_2]\cdot DMSO_2$) needs to take up one equivalent of MAI to yield **PV** ($MA^+PbI_3^-$) as in the following chemical equation:

$$(MA^+)_2[(PbI_3^-)_2PbI_2]\cdot DMSO_2 + MA^+I^- = 3\ MA^+PbI_3^- + 2\ DMSO$$

Thus **INT-4** was assigned as $(MA^+)_3Pb_3I_9^{3-}\cdot DMSO_2$. After the evolution of **INT-4** diffraction signal, diffraction signal of **INT-5** appeared as **INT-4** signal disappeared. This **INT-5** diffraction was spotted to the direction orthogonal to *a*-axis of initial **INT-3** orientation. Considering the fact that the conversion of **INT-4** to **PV** requires loss of two equivalents of DMSO molecules, **INT-5** was assigned as $(MA^+)_3Pb_3I_9^{3-}\cdot DMSO_1$ (Figure 2.8b). This is equivalent to **INT-4** – DMSO. The signal of **INT-5** gradually disappeared as the conversion to **PV** completed. Overall, the conversion of **INT-3** to **PV** occurs by first diffusion of one equivalent of MAI into the crystal lattice of **INT-3** followed by successive loss of two equivalents of DMSO molecules.

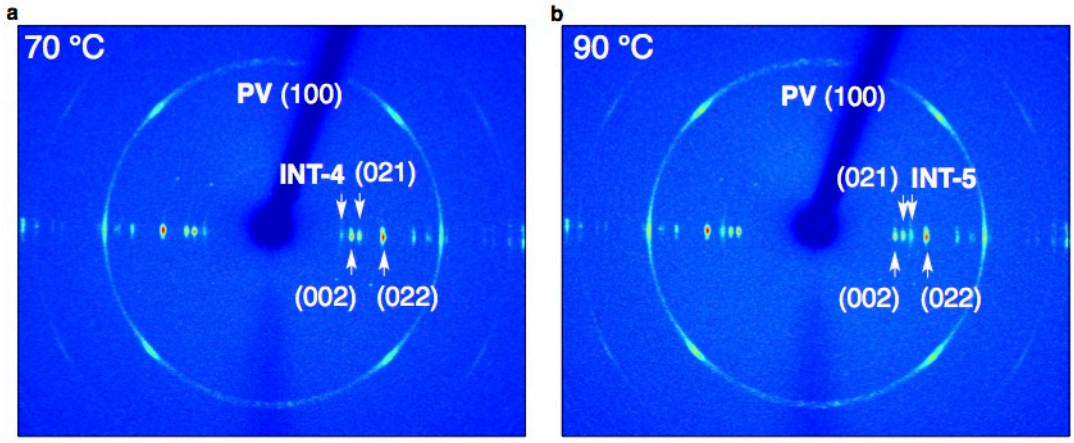

Figure 2.8. 2-D fiber XRD patterns of transient intermediates occurring in the conversion between **INT-3** and **PV**. **a**, **INT-4**. **b**, **INT-5**.

Fiber XRD analysis of **PV** formation process revealed in-depth views of this crystal-to-crystal conversion. Important focus point is crystal orientation during the conversions. In DMSO system, the conversion of fibrous plumbate **INT-3** resulted in oriented crystalline **PV** fiber. This fibrous **PV** has a crystalline nature, not poly-crystalline nature. The reversion of **PV** to **INT-3** still partly keeps initial crystal orientation, while partly running orthogonal to it. Second conversion of **INT-3** to **PV** results in near-complete loss of orientation due to successive gradual orientation loss. This orientation loss is quicker in DMF system, as in the first cycle it already started to give orthogonally aligned **PV**. The complete orientation loss occurred already in the reversion process of **PV** to **INT-7**, which is one step earlier than DMSO system. The quicker loss is chemically attributed to lower donor number of DMF than DMSO.

2.3 Conclusions

In this chapter, the whole chemical pathway of a system consists of **PI**, MAI, and a polar solvent, either DMSO or DMF were presented. These solvent systems are of significant interest among **PV**-based solar cell community, since recent reports on solution-processed **PV**-based solar cells almost exclusively use these solvent systems. The whole system consists of a series of equilibria involving reversible participation of solvent (shown schematically for DMSO system in Figure 2.9). In the middle of the conversion of a 2-D layered sheet crystal of **PI** (Figure 2.9a) to a 3-D cubic crystal of **PV** (Figure 2.9c) lies a 1-D fibrous crystal of intermediates (Figure 2.9b, d). Participation of solvent is required for the conversion of **PI** to intermediates, while removal of solvent is required for the conversion of intermediates to **PV**. Hence, the solvent is necessary for the conversion but should be removed in the end of **PV** formation. The conversion of intermediates to **PV** is reversible, during which single crystalline **PV** crystal exhibits polycrystalline nature (Figure 2.9e). This equilibrium in the

end forms larger **PV** crystals on a substrate scattered with fibrous intermediates (Figure 2.9f). The facile reversal of **PV** to either **INT-3** or **INT-7** provokes the importance of precise kinetic control of solvent removal when forming high-quality thin-films of **PV** by solution process. At temperatures higher than 130 °C the **PV** crystal decomposes by loss of MAI, which is another stability issue of **PV**.

The choice of solvent gave changes in the conversion rate of intermediates to **PV** and morphology of the resulting **PV** fibers. This will be further discussed in Chapter 3 along with the conversion in the system that contains water instead of DMSO or DMF.

The conversion of intermediates to **PV** was investigated in detail as an example of crystal-to-crystal conversions. Atom-to-atom mapping of intermediates and **PV** demonstrated 45° inclination of initial fiber axis and two of the three crystallographic axes of **PV**. This fact poses the importance of quick conversion of intermediates to **PV** when preparing high-quality **PV** thin-films, as I will discuss in Chapter 5.

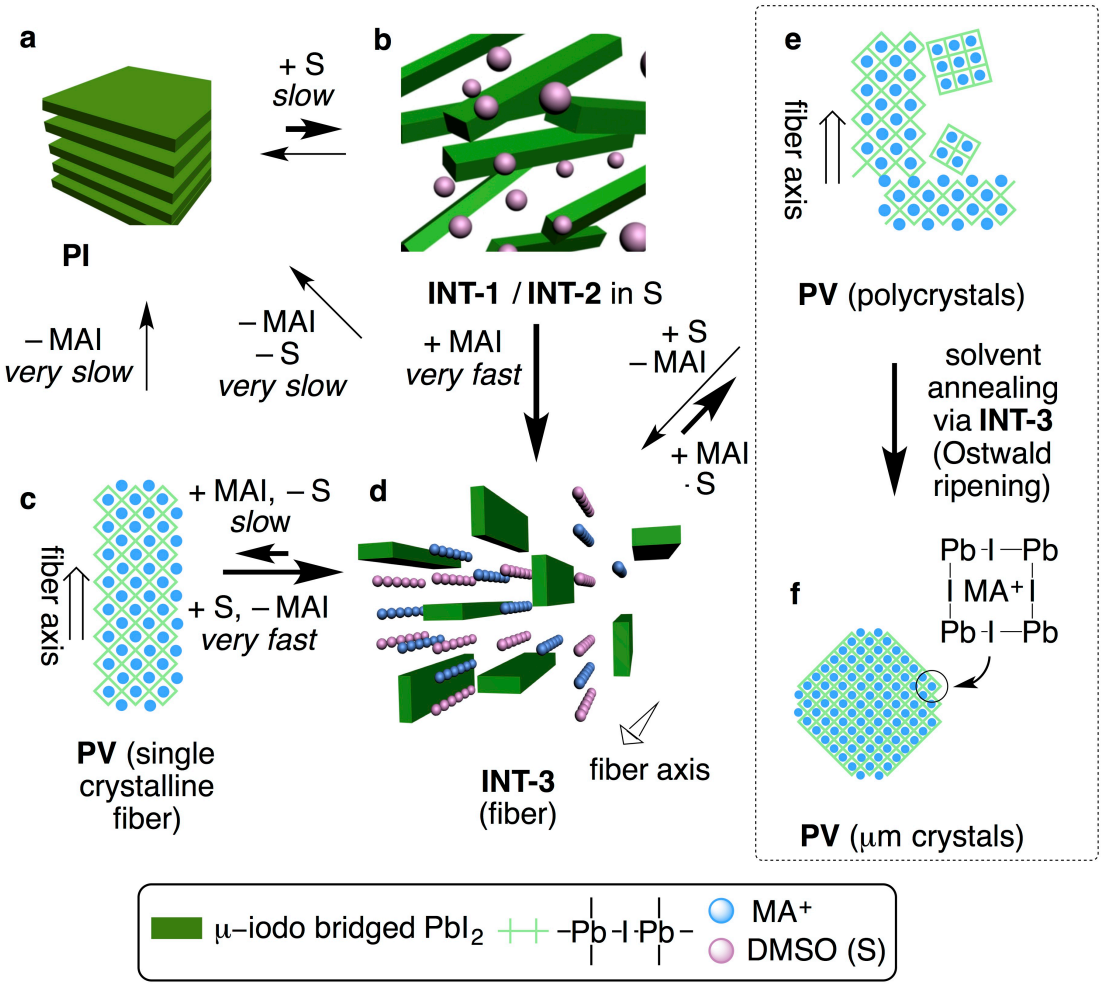

Figure 2.9. Schematic image of the chemical pathways in **PV** formation in DMSO system. a, Layered structure of **PI**. **b**, Fiber intermediate structure constructed in solvent. **c**, Final fibrous **PV** solid. **d**, 1-D fibrous crystal of the intermediate species. **e**, Polycrystalline **PV** as the result

of repeated inter-conversions between the intermediate species and **PV**. **f**, Larger crystal of **PV** as the result of Ostwald ripening process.

2.4 Experimental

2.4.1 Synthesis

2.4.1.1 Methylammonium iodide

A 33 wt% solution of methylammonium in ethanol (25 mL, 200 mmol) and a 57 wt% hydroiodic acid (26.4 mL, 200 mmol) were mixed at 0 °C in a flask. The mixture was stirred for 2 h then the solvent was removed under reduced pressure. The resulting crystalline powder was then recrystallized with ethanol, and dried under vacuum for 12 h at 60 °C to yield a white crystalline solid of methylammonium iodide (24.0 g, 75 % yield).

2.4.1.2 INT-1 [mono-nuclear strips of $(PbI_2)_n$, $PbI_2 \cdot DMSO_2$]

A 30 wt % PbI_2 solution was prepared by adding PbI_2 (448 mg) to DMSO/γ-butyrolactone (GBL) (1.0 mL, 3:7 vol/vol ratio) and it stirred for 12 h at 60 °C. The solution was then cooled to room temperature to obtain crystals of **INT-1**.

2.4.1.3 INT-2 [di-nuclear strips of $(PbI_2)_n$, $(PbI_2)_2 \cdot DMSO_2$].

A 40 wt % PbI_2/MAI solution was prepared by adding PbI_2 (555 mg) and MAI (192 mg) in DMSO/GBL (1.0 mL, 3:7 vol/vol ratio) and it stirred for 12 h at 60 °C. The solution was cooled to room temperature, and 10−20 vol % of toluene was added to obtain fibers of **INT-2**.

2.4.1.4 INT-3 [tri-nuclear strips of $(PbI_2)_n$ coordinated by two iodide ions, $(MA^+)_2[(PbI_3^-)_2PbI_2] \cdot DMSO_2$]

A 50 wt % PbI_2/MAI solution was prepared by adding PbI_2 (833 mg) and MAI (287 mg) in DMSO/GBL (1.0 mL, 3:7 vol/vol ratio) and it stirred for 12 h at 60 °C. The solution was cooled to room temperature to obtain fibers of **INT-3**.

2.4.1.5 INT-6 [di-nuclear strips of $(PbI_2)_n$, $(PbI_2)_2 \cdot DMF_2$]

A 30 wt % PbI_2 solution was prepared by adding PbI2 (405 mg) to DMF (1.0 mL) and it stirred for 12 h at 60 °C. The solution was then cooled to room temperature to obtain fibers of **INT-6**.

2.4.1.6 INT-7 [di-nuclear strips of $(PbI_2)_n$ coordinated by two iodide ions, $(MA^+)_2(PbI_3^-)_2 \cdot DMF_2$]

A 50 wt % PbI_2/MAI solution was prepared by adding PbI_2 (702 mg) and MAI (242 mg) in DMF (1.0 mL) and it stirred for 12 h at 60 °C. The solution was cooled to room temperature to obtain fibers of **INT-7**.

2.4.2 Crystallographic analysis

The diffraction images for X-ray crystallographic analysis were collected on a Rigaku Rapid II diffractometer equipped with an imaging plate (IP) using Cu Kα (λ = 1.5419 Å) radiation. For crystallographic analysis, the sample was removed from the mother liquor and put onto a glass slide. A crystal was chosen and then it was put on and taken off from a glass slide several times to remove liquid from its surface. The positional and thermal parameters were refined by the full-matrix least-squares method using SHELXL-2014/7 program.[71] The Yadokari-XG software was used for refinement of the structure.[72]

2.4.2.1 Crystallographic data of INT-1 (20 °C) (CCDC 1064049)

Formula	$C_2I_2O_2PbS_2$, $4(C_{0.50})$
Formula weight	605.15
Measurement temperature	293(2) K
Crystal system	Orthorhombic
Space group	*Cmmm*
Lattice parameters	a = 11.0774(7) Å
	b = 13.8442(8) Å
	c = 4.5169(3) Å
	α = 90°
	β = 90°
	γ = 90°
Volume	692.70(8) Å^3
Z value	2
Density (calculated)	2.901 g/cm^3
F(000)	520
Number of reflections measured	3710
Number of unique reflections	398
R_{int}	0.1488
Number of observed reflections ($I > 2\sigma(I)$)	385
Goodness of fit indicator	1.193
Final R_1 indices [$I > 2\sigma(I)$] (R_{obs}, wR_{obs})	0.0470, 0.1057
R indices [all data] (R_{all}, wR_{all})	0.0484, 0.1079
Largest diff peak and hole	2.193/−1.091 e·Å^{-3}

2.4.2.2 Crystallographic data of INT-2 (−150 °C) (CCDC 1063983)

Formula	$C_2H_6I_2OPbS$
Formula weight	539.12
Measurement temperature	123(2) K
Crystal system	Orthorhombic
Space group	*Pnma*
Lattice parameters	a = 17.7962(11) Å
	b = 4.5112(3) Å
	c = 11.1382(6) Å
	α = 90°
	β = 90°
	γ = 90°
Volume	894.20(9) $Å^3$
Z value	4
Density (calculated)	4.005 g/cm^3
F(000)	920
Number of reflections measured	5527
Number of unique reflections	905
R_{int}	0.0809
Number of observed reflections ($I > 2\sigma(I)$)	814
Goodness of fit indicator	1.202
Final R_1 indices [$I > 2\sigma(I)$] (R_{obs}, wR_{obs})	0.0758, 0.1716
R indices [all data] (R_{all}, wR_{all})	0.0833, 0.1769
Largest diff peak and hole	3.446/−3.499 $e \cdot Å^{-3}$

2.4.2.3 Crystallographic data of INT-2 (20 °C) (CCDC 1415481)

Formula	$C_2H_6I_2OPbS$
Formula weight	539.13
Measurement temperature	293(2) K
Crystal system	Orthorhombic
Space group	*Pnma*
Lattice parameters	a = 17.9494(9) Å
	b = 4.5326(2) Å
	c = 11.2165(6) Å
	α = 90°
	β = 90°
	γ = 90°
Volume	912.55(8) Å^3
Z value	4
Density (calculated)	3.924 g/cm^3
F(000)	920
Number of reflections measured	9143
Number of unique reflections	955
R_{int}	0.1011
Number of observed reflections ($I > 2\sigma(I)$)	826
Goodness of fit indicator	1.187
Final R_1 indices [$I > 2\sigma(I)$] (R_{obs}, wR_{obs})	0.0646, 0.1360
R indices [all data] (R_{all}, wR_{all})	0.0766, 0.1428
Largest diff peak and hole	2.076/−2.074 e·Å^{-3}

2.4.2.4 Crystallographic data of INT-3 (−150 °C) (CCDC 1063982)

Formula	I_8Pb_3, 2(C_2OS), 2(CN)
Formula weight	1832.97
Measurement temperature	123(2) K
Crystal system	Orthorhombic
Space group	$Cmc2_1$
Lattice parameters	a = 4.59140(10) Å
	b = 27.2463(5) Å
	c = 26.7574(5) Å
	α = 90°
	β = 90°
	γ = 90°
Volume	3347.32(11) $Å^3$
Z value	4
Density (calculated)	3.637 g/cm^3
F(000)	3072
Number of reflections measured	18021
Number of unique reflections	3472
R_{int}	0.1022
Number of observed reflections ($I > 2\sigma(I)$)	2740
Goodness of fit indicator	1.150
Final R_1 indices [$I > 2\sigma(I)$] (R_{obs}, wR_{obs})	0.0639, 0.1600
R indices [all data] (R_{all}, wR_{all})	0.0820, 0.1714
Largest diff peak and hole	4.354/−3.250 $e \cdot Å^{-3}$

2.4.2.5 Crystallographic data of INT-3 (20 °C) (CCDC 1415480)

Formula	I_8Pb_3, 2(C_2OS), 2(CN)
Formula weight	1832.97
Measurement temperature	293(2) K
Crystal system	Orthorhombic
Space group	$Cmc2_1$
Lattice parameters	a = 4.6216(7) Å
	b = 27.455(4) Å
	c = 26.933(4) Å
	α = 90°
	β = 90°
	γ = 90°
Volume	3417.5(9) $Å^3$
Z value	4
Density (calculated)	3.563 g/cm^3
F(000)	3072
Number of reflections measured	15373
Number of unique reflections	3307
R_{int}	0.1918
Number of observed reflections ($I > 2\sigma(I)$)	1000
Goodness of fit indicator	0.713
Final R_1 indices [$I > 2\sigma(I)$] (R_{obs}, wR_{obs})	0.0650, 0.1030
R indices [all data] (R_{all}, wR_{all})	0.2054, 0.1278
Largest diff peak and hole	2.131/−1.909 $e \cdot Å^{-3}$

2.4.3 Fiber XRD analysis

The diffraction images for fiber X-ray analyses were collected on a Rigaku Rapid II diffractometer equipped with an IP using Cu Kα (λ = 1.5419 Å) radiation. Diffraction images were taken under the following conditions: exposure time, 1 s/ °; $d\omega$, 180°. The fiber was placed with its fiber axis perpendicular to the horizontal line. The fiber was kept under nitrogen atmosphere during measurement. The measurement temperature was controlled by a heater attached to the nitrogen generator. Image acquisition took 5 min, 3 min for exposure, 2 min for IP reading.

2.4.3.1 Sample preparation method for conversion of INT-3 + MAI to PV

For **INT-3** fibers coated with MAI and DMSO, first, a bundle of fibers was removed from the mother liquor by tweezers and put on a glass slide. Then a sample loop was used to pick up multiple fibers without removing liquid from their surface, and the fibers were mounted on a goniometer.

2.4.3.2 Sample preparation method for conversion of INT-3 to PV and PI

For **INT-3** fibers without MAI and DMSO, first, a sample loop was used to pick up a single fiber. To remove liquid from the surface, the fiber was dipped into a droplet of dichloromethane and then mounted on a goniometer.

2.4.3.3 Conversion from INT-3 to PV

The conversion from **INT-3** to **PV** was performed in the following manner. **INT-2** fibers were put on a glass slide without removing the solvent surrounding them. The sample was left under ambient conditions until most of the solvent evaporated (for 2 h) to obtain **INT-3** fibers covered with MAI. A bundle of fibers aligned in the same direction was then taken by a sample loop and mounted on a goniometer. **INT-3** fibers were heated from 20 to 100 °C with an interval of 5 min for each 10 °C. Conversion to **PV** was completed around 0.5 h after the temperature reached 100 °C. The conversion quickly finished at 130 °C.

2.4.3.4 Conversion from INT-7 to PV

The conversion from **INT-7** to **PV** was studied in a similar manner as for **INT-3**−**PV** conversion. **INT-7** fibers were prepared directly from solution. A single **INT-7** fiber was heated from 20 to 100 °C with an interval of 5 min for each 10 °C. The conversion completed when the temperature reached 100 °C.

2.4.3.5 Vapor treatment experiment

For the vapor-treatment experiment the **PV** fiber sample was prepared from **INT-3** or **INT-7** as described above. The **PV** fiber sample was kept for 0.5 h under nitrogen saturated with DMSO or DMF vapor. The fiber XRD measurement was performed at 20 °C. Conversion to **PV** finished at 100 °C.

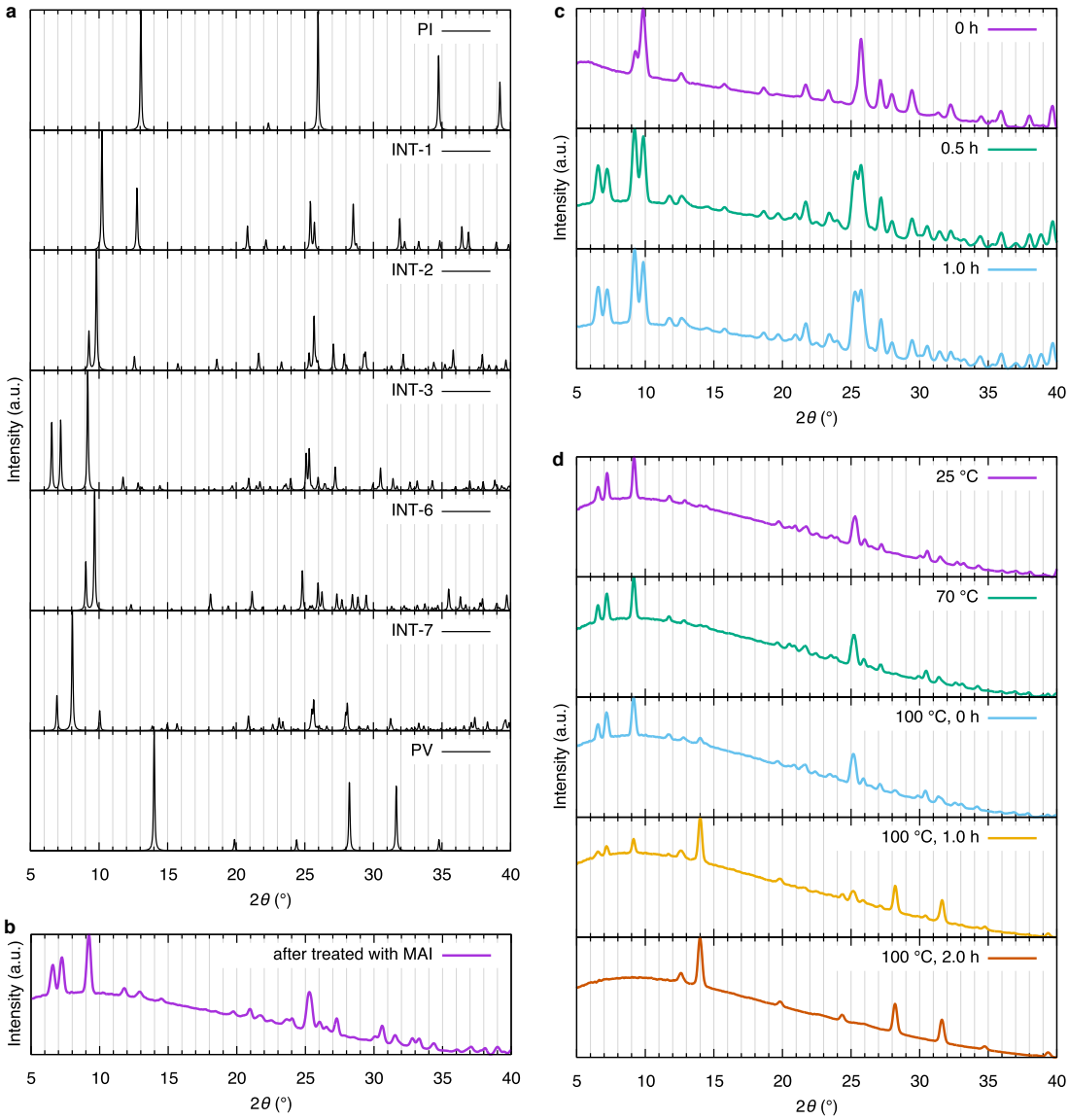

Figure 2.10. Fiber XRD patterns of conversion among **PI**, **INT-1**–**3**, **INT-6**, **-7**, and **PV** (1/3). **a**, Simulated XRD patterns of **PI**[57], **INT-1**–3, **INT-6**[62], 7[63], and **PV**[29]. **b**, XRD pattern of **INT-1** treated with MAI. **INT-1** crystals were put onto a glass slide from the mother liquor. One drop of MAI solution (60 mg/mL in isopropyl alcohol) was coated over the crystals. After 30 s, the rod-like crystals of **INT-1** exhibited polycrystalline surface texture. After these operations **INT-1** fully converted to **INT-3**. **c**, XRD patterns of a bundle of **INT-2** fibers coated with MAI and DMSO. **INT-2** converts to **INT-3** within 0.5 h. **d**, XRD patterns of an **INT-3** fiber, which was washed by dichloromethane before measurement to remove MAI from the fiber surface. After 2 h the fiber converted to **PI** and **PV**.

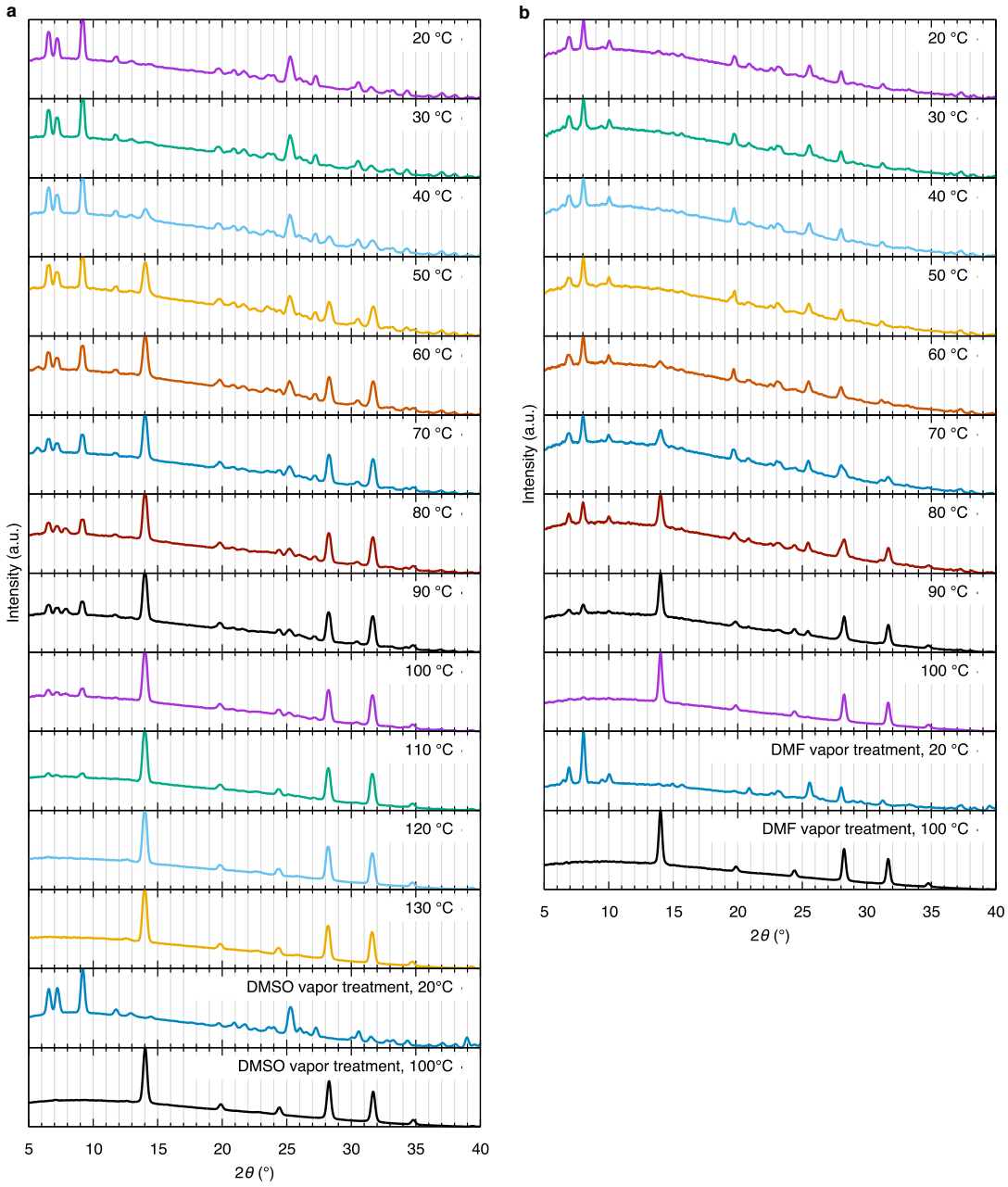

Figure 2.11. Fiber XRD patterns of conversion among **PI**, **INT-1**–**3**, **INT-6**, **-7**, and **PV** (2/3). **a**, XRD patterns of inter-conversion between **INT-3** and **PV**. A bundle of **INT-3** fibers was heated from 20 °C to 130 °C with a 10 °C step. Each measurement took 5 min. The resulting **PV** fiber was then treated with DMSO vapor for 0.5 h at 25 °C and measured at 20 °C. Finally the fibers were heated to 100 °C for 0.5 h and measured at 100 °C. **b**, XRD patterns of inter-conversion between **INT-7** and **PV**. A single **INT-7** fiber was heated from 20 °C to 100 °C with a 10 °C step. Each measurement took 5 min. The resulting **PV** fiber was then treated with DMF vapor for 0.5 h at 25 °C and measured at 20 °C. Finally the fiber was heated to 100 °C for 0.5 h and measured at 100 °C.

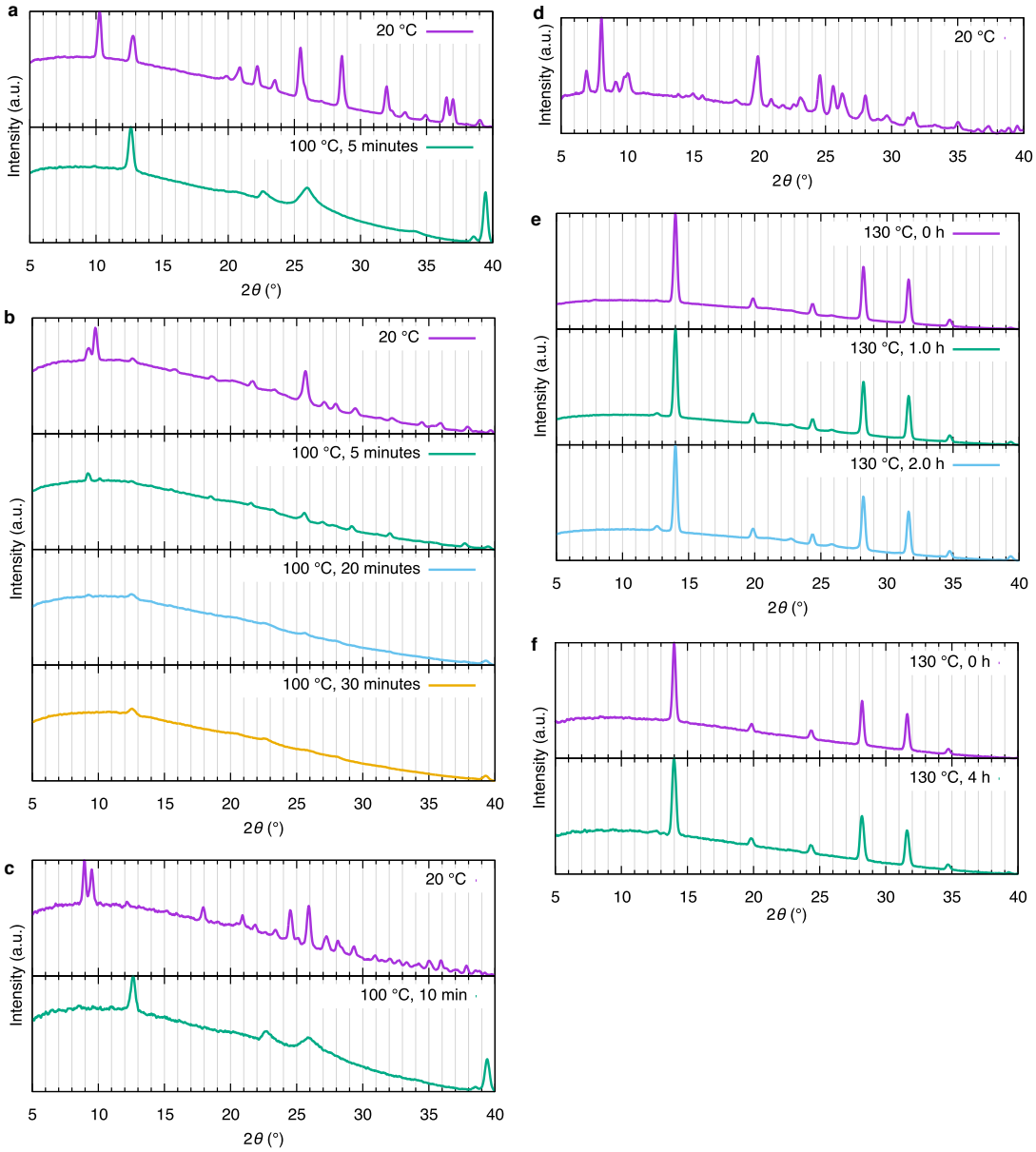

Figure 2.12. Fiber XRD patterns of conversion among **PI**, **INT-1**–**3**, **INT-6**, **-7**, and **PV** (3/3). **a**, XRD patterns of a rod crystal of **INT-1** at 20 °C and after heating at 100 °C for 5 min. Decomposition to **PI** occurred within 5 min. **b**, XRD patterns of a single **INT-2** fiber at 20 °C and then heated to 100 °C for 30 min. Decomposition to **PI** occurred within 30 min. **c**, XRD patterns of an **INT-6** fiber at 20 °C and after heating at 100 °C for 10 min measured at 100 °C. Decomposition to **PI** occurred within 10 min. **d**, XRD pattern of **INT-6** fibers dipped in a MAI solution in DMF for 0.5 h. **e**, XRD patterns of a **PV** fiber prepared from **INT-3** heated at 130 °C over two hours. A peak of **PI** started to appear at $2\theta = 12.6°$. **f**, XRD patterns of a **PV** fiber prepared from **INT-7** heated at 130 °C over two hours. A peak of **PI** started to appear at $2\theta = 12.6°$.

2.4.4 SEM analysis

SEM measurement was conducted on an FEI Magellan 400L instrument at a landing voltage of 1 kV under a reduced pressure of 5×10^{-5} Pa.

Chapter 3.

Chemical origin of the effects of water on lead perovskite crystal growth

3.1 Introduction

The effect of water on the formation process of lead perovskite ($CH_3NH_3^+PbI_3^-$; $MA^+PbI_3^-$; **PV**) is often discussed in two different contexts. One is concerned with decomposition of **PV** to lead iodide (PbI_2; **PI**) and methylammonium iodide ($CH_3NH_3^+I^-$; MAI),[73-77] the other is control of **PV** thin-film morphology to boost the performance of solar cell devices.[78-82] The former refers to an adverse effect of water, the latter to a beneficial effect. Yet still unanswered question is from where those two controversial effects originate.

In this chapter is presented a discussion of the effect of water to the crystallization process of **PV** from chemistry-oriented viewpoint. Specifically I isolated an intermediate species of **PV** in water,[63] and analyzed the conversion process to **PV** using X-ray diffraction (XRD) analysis as in Chapter 2. The specific concern in this analysis was the kinetics of **PV** formation process. This kinetics was investigated on the basis of acid–base and coordination chemistry. The results provided an evident connection between the two controversial effects of water.

Decomposition of **PV** by water vapor is one of the concerns of **PV**-based devices. In the beginning of **PV**-based solar cells research, a group of researchers reported vacuum co-deposition method to avoid this issue.[60] This method gave better reproducibility that can be associated to the water-free environment during the film deposition process. Some other methods include the use of 2-D perovskite materials that are better tolerant against degradation by water vapor.[77] In a similar manner, a method to use thiocyanite instead of iodide to form a different perovskite crystal structure was developed to alleviate the decomposition.[83,84]

Regarding the beneficial effects of water to **PV**, there are several reports that mention that water vapor can enhance film morphology of **PV**.[78-82] A group of researchers reported that by annealing thin-films in ambient conditions achieved high PCEs up to 19.3%[78] – among the top records of lead perovskite solar cells. The effect of water vapor on the performance of solar cells was rather comprehensively studied using UV-Vis spectroscopy and photoluminescence experiments.[82]

These reports well represent phenomenological observations of the effects of water, yet the chemical origins of these effects remain elusive. In this chapter I focus on chemical experiments using XRD analysis of reaction products. Here I demonstrate that, by studying the conversion of a fibrous **PV** intermediate to **PV** occurring in the system composed of water, **PI**, and MAI, formation of **PV** from plumbate intermediates is more facile in this system than in DMF or DMSO system. It was found that water rather accelerates reversible conversion from the intermediate to **PV**, than “deteriorates” **PV**. This fast conversion can be attributed to the weaker Lewis basicity of water compared to other frequently-used solvents

such as DMF and DMSO. Along with discussions in Chapter 2, it is also demonstrated that the morphology of **PV** crystals depends on the crystal lattice volume change between plumbate intermediates and **PV**, which is smallest in water system among three solvent systems. The idea to avoid significant volume change suggests formation of **PV** crystals without the formation of plumbate intermediates should serve as a way to form smoother and more dense **PV** thin-films in solution process. These findings provide clues to understand the effects of water during fabrication of **PV**-based devices.

In the following discussion **INT-3** ($(MA^+)_2[(PbI_3^-)_2PbI_2]\cdot DMSO_2$) and **INT-7** ($(MA^+)_2\cdot(PbI_3^-)_2\cdot DMF_2$) first described in Chapter 2 are renamed as **INT-S** and **INT-F**, respectively.

3.2 Results and discussion

3.2.1 Chemical reactions in water system

I first identified chemical species that exist in a system composed of water, MAI, and **PI** using X-ray diffraction (XRD) analysis (Figure 3.1). When **PI** was added to a solution of MAI in water (2 mol/L) it immediately produced di-nuclear polymeric plumbate ($(MA^+)_2\cdot(PbI_3^-)_2\cdot(H_2O)_2$; **INT-W**) as pale-yellow precipitates, which was isolated in different conditions previously.[63] When the suspension was heated to 90 °C it produced black precipitates of **PV** without dissolution of **INT-W**. This conversion occurred reversibly; when the suspension of **PV** was cooled to room temperature it reverted to a pale-yellow suspension of **INT-W**.

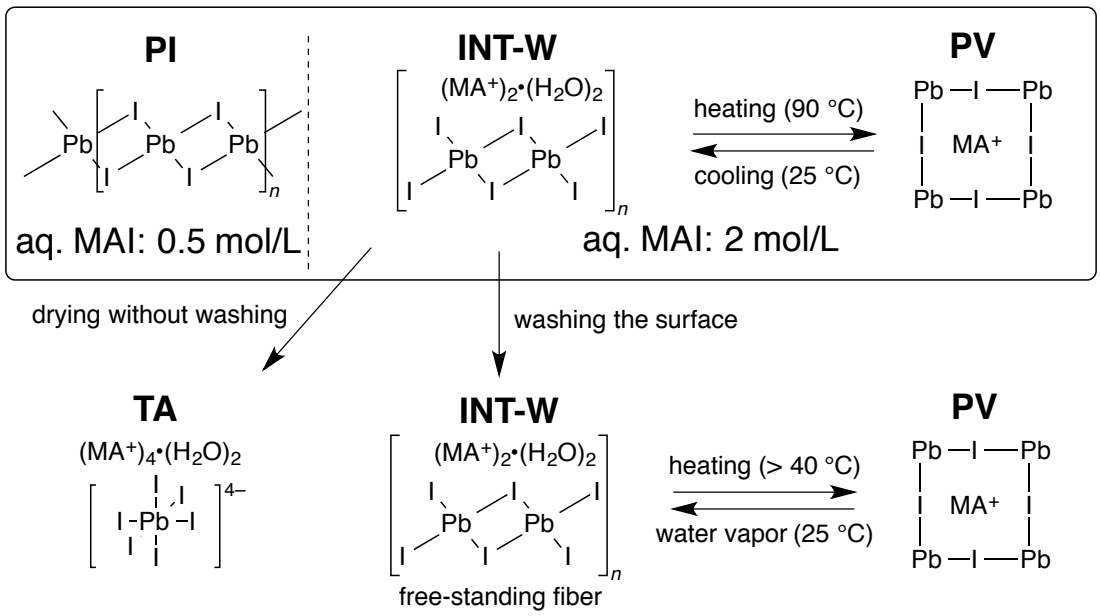

Figure 3.1. Chemical equilibrium of the system composed of water, **PI** and MAI.

Concentration of MAI plays an important role in reactions occurring in the water system. The reaction occurred in the form of precipitates since the solubility of **INT-W** in water is low, similar to that of **PI**. Thus, the reaction from **PI** to **INT-W** is driven by rapid equilibrium of the following chemical equation on the surface of **PI** solid upon addition of MAI:

$2\ PbI_2 + 2\ MA^+I^- + 2\ H_2O \rightleftarrows (MA^+)_2{\cdot}(PbI_3^-)_2{\cdot}(H_2O)_2$

As such, the equilibrium that involves water, MAI, and **PI** controls this reaction. Because the amount of water is constant at the surface of **PI**, the concentration of MAI controls this reaction. A high concentration (e.g. 2 mol/L) of MAI was used for preparing **INT-W**; lower concentrations (e.g. 0.5 mol/L) gave no reaction to **PI**. When **INT-W** precipitates were taken out from a 2 mol/L water solution of MAI it produced tetra anion ($(MA^+)_4{\cdot}(PbI_6^{4-}){\cdot}(H_2O)_2$; **TA**)[62] due to concentration of MAI at the surface of precipitates.

This concentration dependence demonstrates that the chemical species in this system are in equilibrium one another by reversible participation of water and MAI molecules. Since the only difference of the chemical formulae of **INT-W** and **PV** is presence of water molecules the inter-conversion of **INT-W** and **PV** is simply described as reversible participation of water molecules in the solid-state.

3.2.2 Structures of INT-W and related plumbate species

Figure 3.2 shows crystallographic structures of **INT-W** ($(MA^+)_2(PbI_3^-)_2{\cdot}(H_2O)_2$), **-F** ($(MA^+)_2(PbI_3^-)_2{\cdot}DMF_2$),[63] and **-S** ($(MA^+)_2[(PbI_3^-)_2PbI_2]{\cdot}DMSO_2$), focusing on one strip of plumbate(II) unit seen along the fiber axis for each intermediate. All structures are measured at the same temperature (−150 °C) to allow comparison of bond lengths and connection angles. The terminal iodine atom of the plumbate(II) strip of each intermediate is interacting with a positively charged MA^+ fragment, which is also interacting with an solvent molecule (H_2O, DMF, or DMSO). Preceding the following discussion I point out that the positions of hydrogen atoms in the crystallographic structures are not directory calculated from diffraction data of the X-ray measurement, but are calculated as idealized hydrogen positions from their designated bond connectivity.[71] As such, the positions of heavier atoms (C, N, O, S, I, and Pb) are used for discussing atom interactions.

The distances between the terminal iodine atom and positively charged nitrogen atom of the nearest MA^+ cation are 3.64, 3.59, and 3.62 Å for **INT-W**, **-F**, and **-S**, respectively. These values are within the sum of Van der Waals radii of iodine, hydrogen atom, and common cationic N–H bond length[85] (1.98 + 1.20 + 1.03 = 4.21 Å). In the same manner, the distances of the nitrogen atom of MA^+ and the oxygen atom the nearest solvent molecule are 2.85, 2.80, and 2.80 Å respectively, all within the sum of Van der Waals radii of nitrogen and oxygen atoms, and hydrogen (1.55 + 1.20 + 1.03 = 3.78 Å). The angles of I–N-O are 74, 82, and 82° respectively. These angles allow one of the hydrogen atoms on the nitrogen atom of MA^+

molecule to head to the terminal iodine atom of the plumbate strip and another to head to the oxygen atom of the solvent molecule. These close distances and wide angles, along with the fact that there are negative charges in the di- or tri-nuclear trips of plumbate and a positive charge in the MA^+ molecule concludes that the plumbate trips are sustained by hydrogen bond networks via MA^+ and solvent molecules. This interaction can be denoted as Pb···H–N–H···O where '···' indicates hydrogen bond.

The molecular interactions discussed above give an implication on the reaction kinetics of the conversion of these intermediates to **PV**. The conversion from intermediates to **PV** involves removal of solvent molecules in the crystal of these intermediates. Thus when the solvent molecule of an intermediate has stronger coordination ability its interaction with neighboring MA^+ cation becomes stronger and the detachment of it becomes slower. This suggests that the coordination ability of water, DMF, or DMSO controls the removal of these molecules during intermediate–**PV** conversion (*vide infra*).

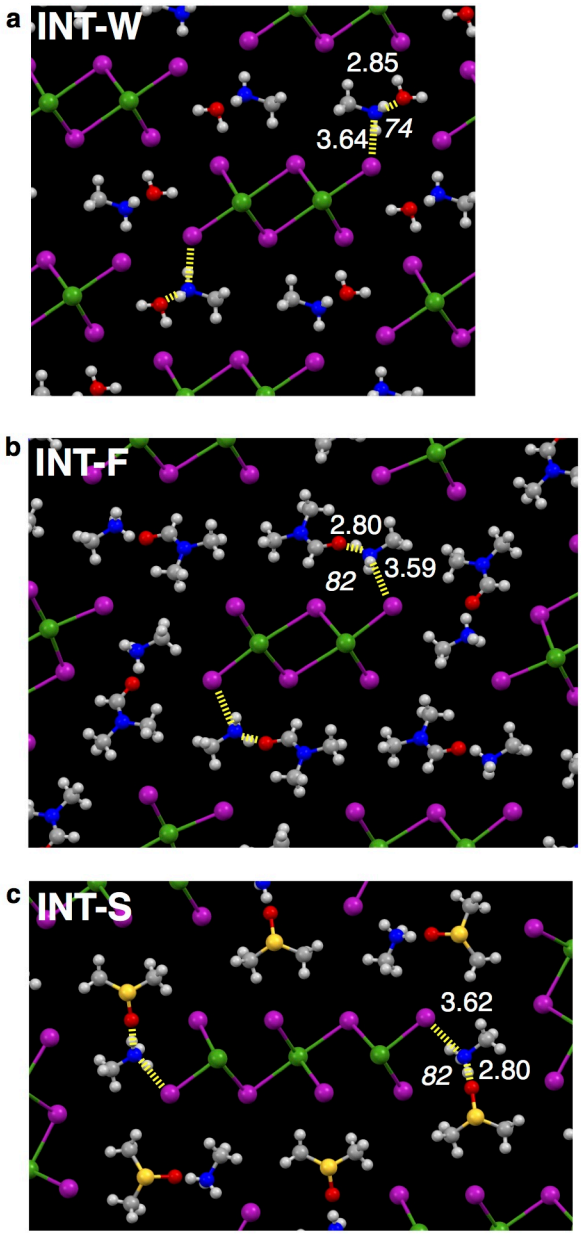

Figure 3.2. Interactions between di- or tri-nuclear strips of plumbate and surrounding molecules in the crystallographic structures of **INT-W**, **-F**, and **-S**, seen from the fiber axis. Numbers written in italic style are angles, others are distances. Inter-fragment interactions are highlighted by yellow dashed lines. The crystallographic date are obtained at −150 °C. **a**, **INT-W**. **b**, **INT-F**. **c**, **INT-S**.

3.2.3 Conversion kinetics study

I used XRD measurements to monitor the reactions between **INT-W** and **PV** (Figure 3.3) as I described in Chapter 2. Single crystalline fibers (ca. 15 micrometers in diameter) of **INT-W** were taken out from mother liquor and washed by dichloromethane to wipe off excess MAI solution sticking on the surface. I note here that when the liquid on the surface of the fiber was not cleaned the fiber converted to the octahedral PbI_6^{4-} cluster **TA** (Figure 3.1) due

to concentration of MAI on the surface. Then an **INT-W** fiber was mounted on a sample loop with its fiber axis perpendicular to the horizontal line under nitrogen atmosphere. The temperature was raised stepwise from 20 °C to 100 °C over 40 min with an interval of 10 °C/5 min for each measurement. At 20 °C the XRD pattern was in good agreement with simulated powder pattern of **INT-W**. The conversion to **PV** started already at *ca*. 30 °C, which is quicker than the same experiment performed for DMSO and DMF systems (Figure 3.4). At 50 °C the peaks of **INT-W** disappeared and the resulting XRD pattern become identical to **PV**. Thus I concluded that the reaction completed at this temperature. Hereafter I use the term T(PV) as the temperature at which intermediate diffraction peaks disappears and only **PV** diffraction are present in the XRD pattern. I note here that the intensity of **PV** increases after 50 °C because of gradual Ostwald ripening process by thermally activated ion migration as discussed in Chapter 2. This quick conversion is in stark contrast to DMF or DMSO system, wherein the conversion completed at 100 °C or 130 °C, respectively. The conversion in DMSO system is quicker in the beginning but complete disappearance of **INT-S** is slower than the other systems. The quicker conversion in the beginning is because in this system the conversion accompanies intake of MAI and formation of transient intermediates thus there is a different type of conversion pathway that involves stepwise bond formation via these transient intermediates. Similar to DMF and DMSO systems, the intermediate–**PV** conversion is reversible in water system, with a slower reversion time. When the **PV** fiber obtained from **INT-W** was kept in saturated water vapor it reverted to **INT-W** over 2 h. The same reaction in DMF or DMSO system completed within 0.5 h. Because the system composed of **PI**, MAI, and solvent is in equilibrium, the slower conversion in water system indicates lower affinity of water molecules to **PV**.

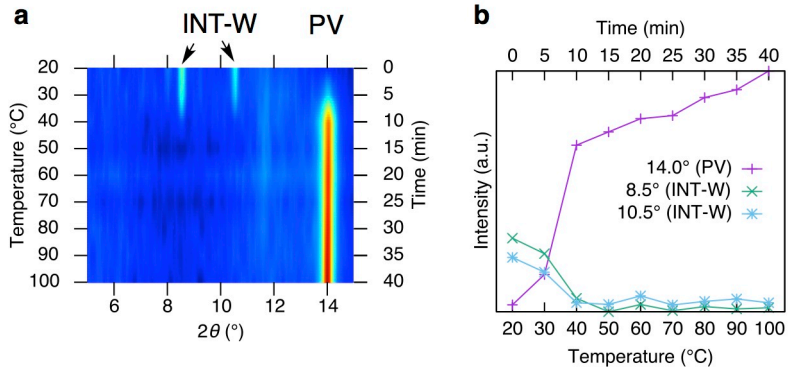

Figure 3.3. The time course of the conversion from **INT-W** to **PV** by stepwise heating. **a**, XRD signal intensity between 2θ = 5° to 15°. **b**, Intensity–time course plot of diffraction peaks from **PV** (14.0°) and **INT-W** (8.5° and 10.5°).

Based on the experimental fact on the reaction kinetics and discussions on the solvent molecule interactions in the crystal structures, I draw the following interpretation of solvent

roles on the reaction. When the system contains a sufficient amount of solvent is produces corresponding plumbate intermediate at room temperature. When the system is applied with heat, the solvent molecules in the intermediate crystal go out of the crystal due to thermal movement. Although the intermediate–**PV** conversion is reversible, the solvent molecule once goes out of crystal it diffuses infinitely away outside of the system, hence **PV** is produced. Because the solvent molecule is bound to MA^+ via hydrogen bond, the temperature at which thermal movements let the solvent molecules away depends on the coordination ability of the solvent molecule.

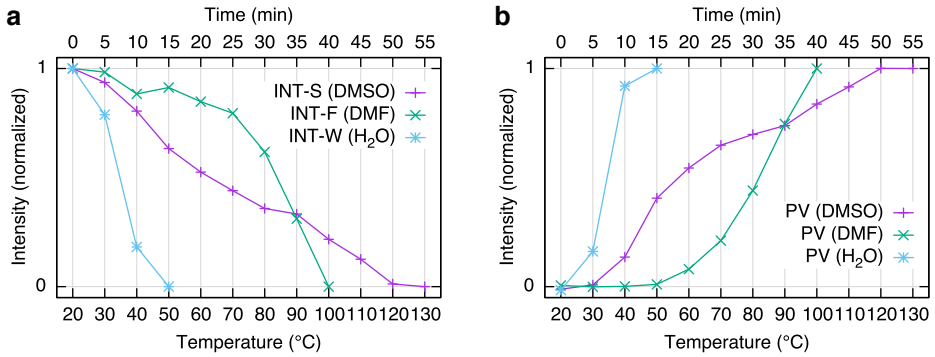

Figure 3.4. Comparison of the conversion kinetics of three different solvent systems (DMSO, DMF, H_2O) between intermediates and **PV**. The plots are XRD intensity against temperature and elapsed time. **a**, XRD intensity of intermediates in three systems. **b**, XRD intensity of **PV** in three systems.

As the measure of coordination ability, I discuss the donor number of these solvents. The donor number (DN) of water, DMF, and DMSO are 18.0, 26.6, and 29.8, respectively (Table 3.1). [69] As discussed above, the water molecule in the crystal of **INT-W** is interacting with the positively charged nitrogen atom of MA^+ through hydrogen bond. The same interaction also exists for DMF and DMSO intermediates. This situation is similar in their pure liquid form. All of these solvent molecules have inter-molecular hydrogen bond interactions. Thus the boiling points (bps) of these solvents are in good accordance with T(PV) and DN (Figure 3.5). Water has the lowest bp, DN, and T(PV) among the three solvents. Those numbers of DMF come in the middle, and those of DMSO come on the top. The weak interaction of water molecule with MA^+ can induce detachment of water at an earlier stage of the conversion. I note here that the conversion process is reversible, which becomes important in the later discussion.

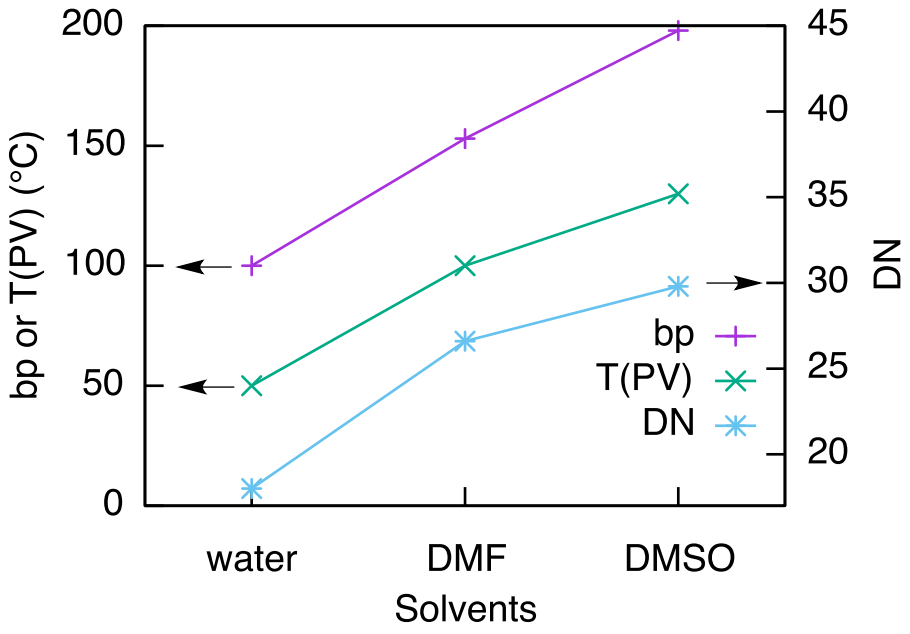

Figure 3.5. Comparison of solvent properties (boiling point (bp) and donor number (DN)) and intermediate–**PV** conversion temperatures (T(PV)) in water, DMF, and DMSO systems.

Table 3.1. Solvent parameters[69] and pK_a values of solvents related to plumbate intermediates and MA^+.[86]

Solvent	Dielectric constant	Dipole moment (D)	bp (°C)	DN	AN	pK_a
H_2O	80	1.85	100	18.0	54.8	15.7
DMF	38	3.82	153	26.6	16.0	
DMSO	46.7	3.96	189	29.8	19.3	
MA^+						10.66

3.2.4 Reaction mechanisms in water system

Two-dimensional (2-D) XRD images show crystal orientation during the conversion (Figure 3.6). As I discussed in Chapter 2, from changes of orientation during the conversion one can identify the atom-to-atom mapping before and after the conversion. Figure 3.6a shows the image before conversion. Diffraction peaks of (100) and $(10\bar{1})$ are aligned parallel to the horizontal line, which coincides with the fiber orientation. After conversion to **PV**, eight spots appeared along (100) diffraction circle. This indicates that the resulting **PV** has two orientations; one is parallel to the horizontal line, the other 90° inclined to that, similar to the observations on the DMF system thus indicating quicker inter-conversion between

intermediate and **PV** than in the DMSO system. The XRD pattern of the fiber reverted back to **INT-W** by exposure to water vapor showed (100) and $(10\bar{1})$ peaks of **INT-W**, which are aligned parallel to the horizontal line similar to the one before inter-conversion cycle with some azimuthal signal widening. This observation indicates that regeneration of **INT-W** from **PV** accompanies tendencies to regain the initial crystallographic orientation that, as discussed later in conjunction with volume change during the conversion, come from morphological smoothness of the resulting **PV** fiber. The XRD pattern of the fiber converted to **PV** again by heated to 100 °C showed no azimuthal signal intensity deviation, indicating the loss of any orientation of the crystal, which is the same for both DMF and DMSO systems.

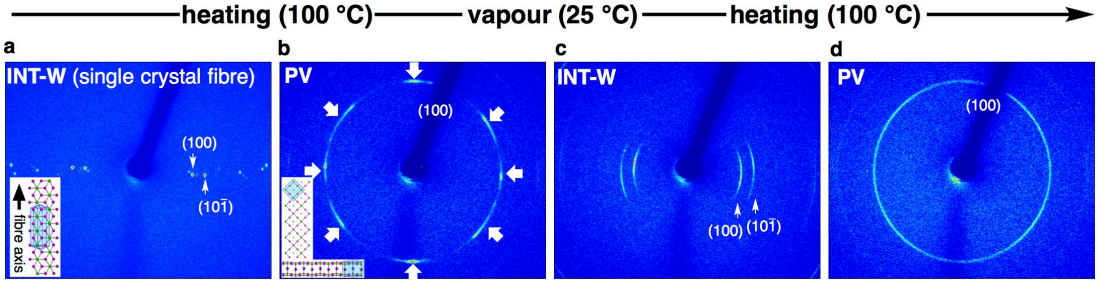

Figure 3.6. 2-D XRD patterns during inter-conversion of **INT-W** and **PV**. **a**, A single crystal fiber of **INT-W**. **b**, Fibrous **PV** prepared by heating **INT-W**. **c**, **INT-W** prepared by reversion of **PV** by moisture treatment. **d**, Fibrous **PV** prepared by heating again the reverted **INT-W**.

In accordance with the DMSO and DMF systems, above XRD data enable to elucidate the reaction mechanism in the crystal-to-crystal conversion as in Figure 3.7 and Figure 3.8. There can be two ways to map atoms of **INT-W** crystal structure onto cubic lattices of **PV** (vertical or horizontal).

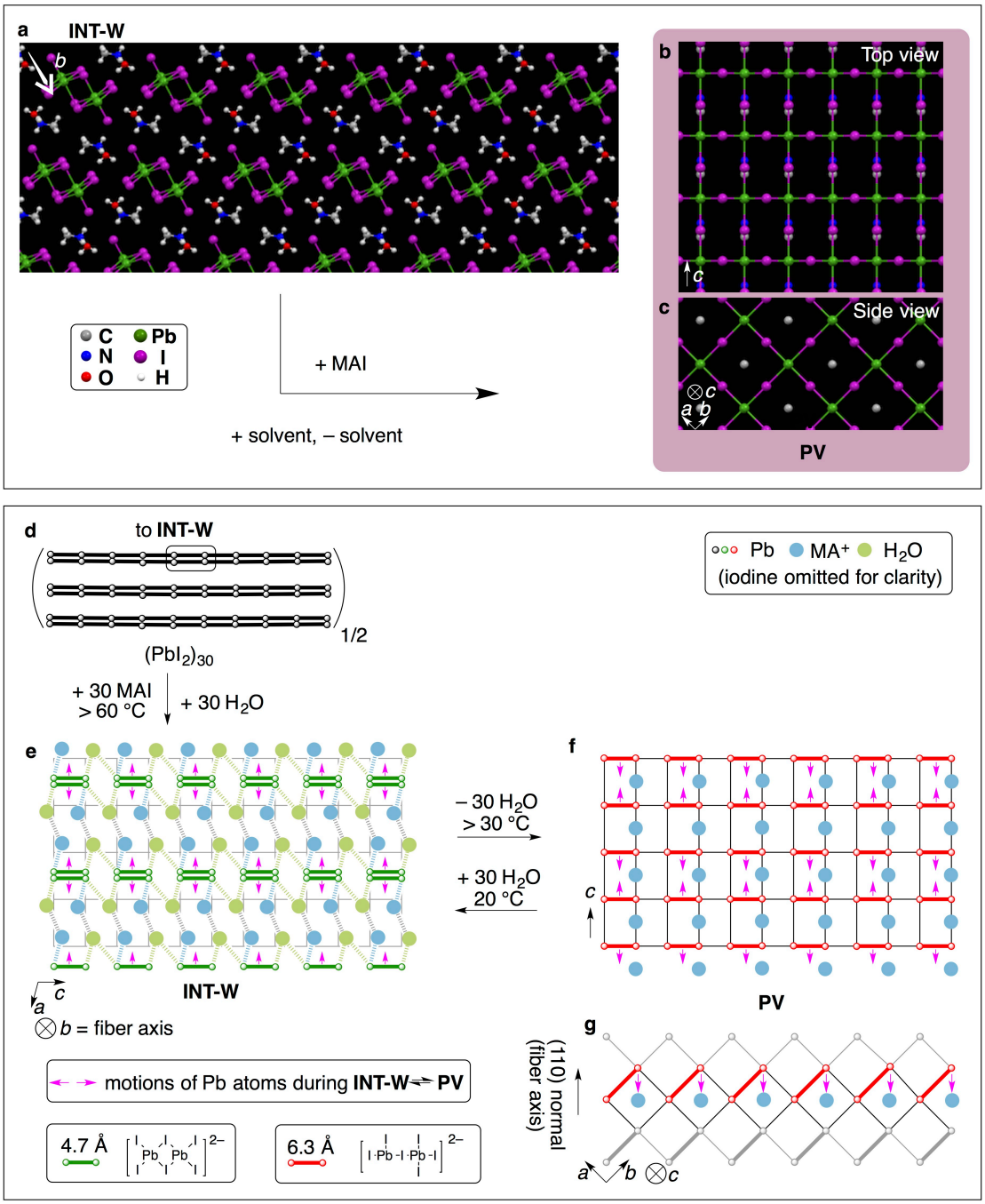

Figure 3.7. Structural correlation between **INT-W** and **PV** (1/2). Only two layers of plumbate is shown. (Top panel) Crystal structures of **INT-W** and **PV**. **a**, Crystal structure of **INT-W** seen along crystallographic *b*-axis, which runs along the fiber axis. **b**, Crystal structure of **PV** seen along the (110) normal. **c**, Seen along *c*-axis. (Bottom panel) Schematic images of **PI**, **INT-W**, and **PV** corresponding to the Top panel images. **d**, A selected area of **PI** layered crystal that converts to **INT-W** and **PV** shown in **Figure 3.7**e–g. **e**, **INT-W** mapped onto the cubic grid of **PV** in **Figure 3.7**f. **f**, The cubic lattice of **PV** that is inclined by 45° laterally. **g**, Side view of **Figure 3.7**f.

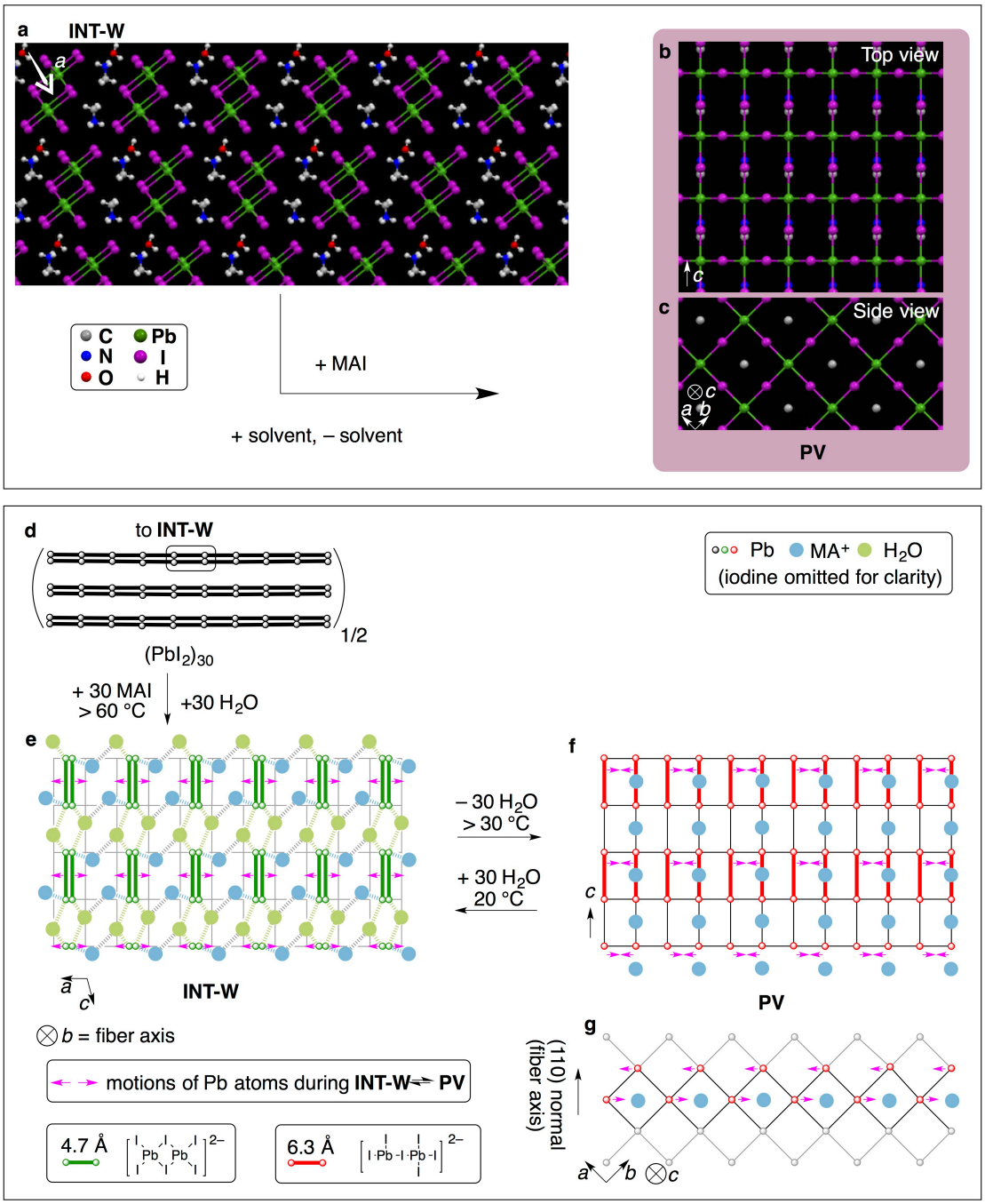

Figure 3.8. Structural correlation between **INT-W** and **PV** (2/2). Only two layers of plumbate is shown. (Top panel) Crystal structures of **INT-W** and **PV**. **a**, Crystal structure of **INT-W** seen along crystallographic *b*-axis, which runs along the fiber axis. **b**, Crystal structure of **PV** seen along the (110) normal. **c**, Seen along *c*-axis. (Bottom panel) Schematic images of **PI**, **INT-W**, and **PV** corresponding to the Top panel images. **d**, A selected area of **PI** layered crystal that converts to **INT-W** and **PV** shown in **Figure 3.8**e–g. **e**, **INT-W** mapped onto the cubic grid of **PV** in **Figure 3.8**f. **f**, The cubic lattice of **PV** that is inclined by 45° laterally. **g**, Side view of **Figure 3.8**f.

3.2.5 Effects of solvents on morphology

The SEM images of **PV** fibers obtained from water revealed their smooth surface (Figure 3.9b). This smoothness is similar to **PV** fibers obtained from **INT-S**, but stands in contrast to the rough and cracked surface of **PV** fibers obtained from **INT-F** (Figure 3.9a). I reason this observation by considering volume changes during the intermediate–**PV** conversion. Smaller volume changes allow smoother surface of resulting **PV** fibers due to lower degree of deformation required for the resulting shrinkage after the conversion.

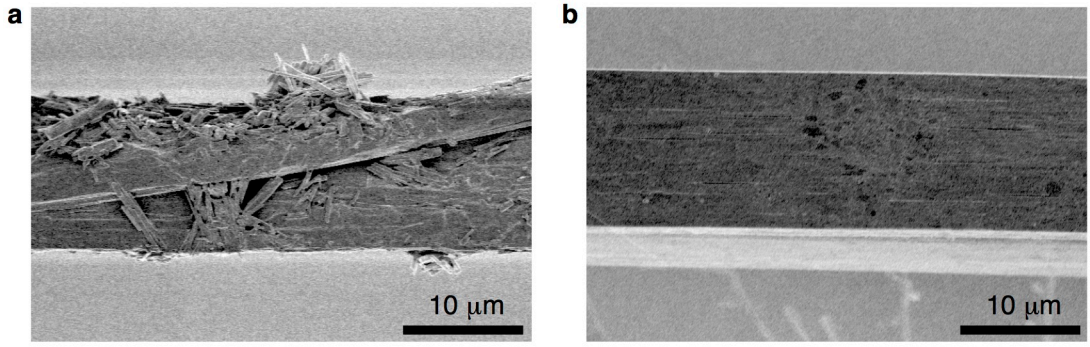

Figure 3.9. SEM images of fibrous **PV** prepared from different intermediates. **a**, **PV** fiber prepared from DMF-coordinated precursor **INT-F** ($(MA^+)_2 \cdot (PbI_3^-)_2 \cdot DMF_2$). **b**, **PV** fiber prepared from water-coordinated precursor **INT-W** ($(MA^+)_2 \cdot (PbI_3^-)_2 \cdot (H_2O)_2$).

Figure 3.10 shows the comparison of volumes of intermediates and **PV** per Pb atom in the three solvent systems. The volume change during the conversion of **INT-W** to **PV** is 10% (273 $Å^3$ to 247 $Å^3$), which is the smallest value among the three systems. The volume change in the DMSO system is the second smallest, 13% (285 $Å^3$ to 247 $Å^3$). The volume change in the DMF system is the largest, 30% (354 $Å^3$ to 247 $Å^3$). This difference comes from the size of solvent molecules and the number of Pb atoms in the plumbate intermediates. The size of water is smallest, followed by DMSO and DMF. The fact that **INT-S** has one more column of lead atoms in each plumbate strip (tri-nuclear plumbate) gives more dense Pb atom concentration, thus giving a significant lowering in the volume change. The volume change is only 10% in water system and only slightly higher in DMSO system (13%) thus giving smoother surfaces of the resulting fibers. That of DMF system is as much as 30% thus giving fractured surfaces.

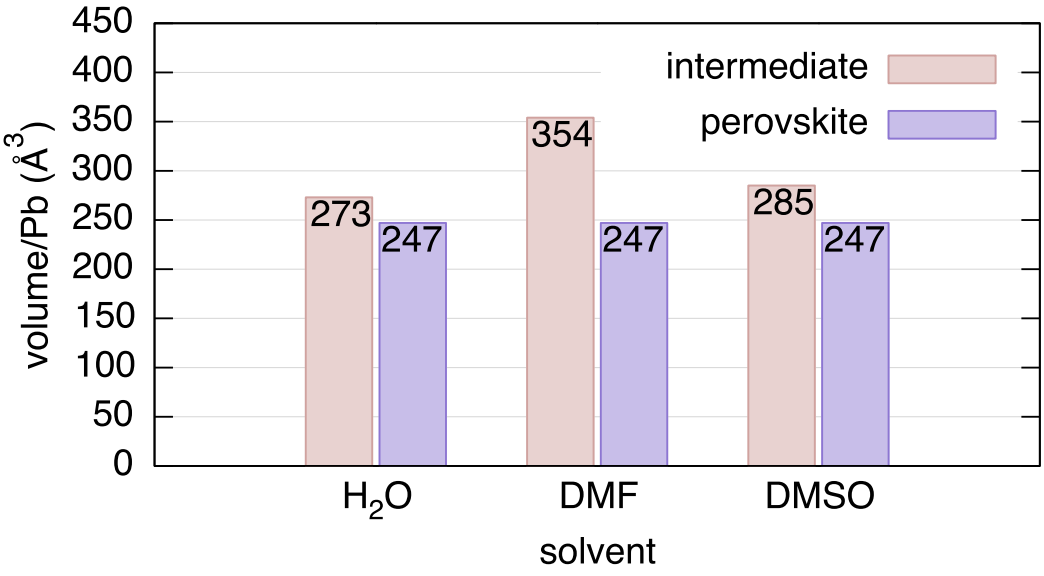

Figure 3.10. Volume comparison of conversions between intermediates (**INT-W**, **-F**, and **-S**) and **PV**. The volumes are calculated from lattice constants measured at 20 °C.

These facts give an explanation to the observed crystallographic orientations of intermediate fibers obtained by reversion of **PV** in the three solvent systems. The orientation in water and DMSO systems retain certain degree of initial orientations, while that in DMF system does not. The retention of orientation in water and DMSO systems is due to tight packing of crystallites in **PV** fibers that does not require significant mass migration to form intermediates.

In order to produce flaw-less crystallites of **PV** from plumbate intermediates, there should be smaller changes of volume during the conversion. In this regard, the conversion pathway in the water system is more desirable than that in the other two solvent systems discussed here, as the volume change is smallest due to the smaller size of water molecule than the other two solvents.

3.2.6 Water-assisted acceleration in the equilibrium of DMSO or DMF system

The equilibrium in DMF or DMSO system is experimentally known to be accelerated by supply of water vapor.[82] With discussions above in mind, this behavior can be explained in the following matter. When **PV** is being produced from **INT-F** or **INT-S** the system is in equilibrium controlled by removal of solvent molecules to the out side of the system. When water is present in addition to these solvents, water molecules can participate in the equilibrium thus giving **INT-W** either directory from **INT-F** or **INT-S**, or via **PV**. Once **INT-W** is present in the equilibrium, the conversion to **PV** occurs at lower temperatures than the conversion pathway from **INT-F** or **INT-S**. As such the conversion from **INT-F** or **INT-S** to **PV** is accelerated. The decomposition of **PV** to **PI** is also induced by the presence of water.

PV, when supplied with water, produces **INT-W**. When this is long left and MAI gradually diffuses to outside of the system[50,87-90] it produces **PI**. I note here that in the experiment synthesizing **INT-W** in aqueous MAI solution, lower concentrations of MAI gave **PI** while higher concentrations gave **INT-W**. This indicates that gradual loss of MAI can let the equilibrium to produce **PI**.

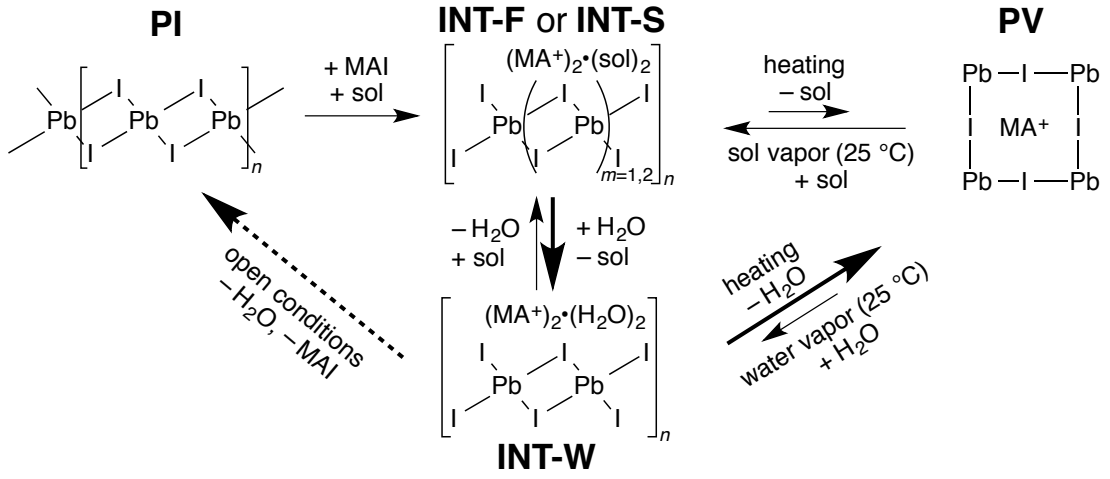

Figure 3.11. The pathways involved in the formation of **PV** from **INT-F** or **INT-S**, or decomposition of **PV** to **PI** in the presence of trace amount of water. Solid bold arrows are used for chemical reactions accelerate **PV** formation process. Dashed bold arrow indicates the path leads to decomposition to **PI**.

3.2.7 Conclusions

In summary, I presented the chemical understanding of the effect of water on the conversion pathway to **PV**. Coordination chemistry plays an important role in the kinetics of the conversion of multi-nuclear strips of plumbate(II) intermediates to **PV**. Because **PV** formation is in equilibrium with plumbate(II) intermediates, presence of water can accelerate the formation of **PV** by participation of the quicker **PV** formation pathway in the water system. Water system also helps formation of **PV** crystals with smoother surface due to small shrinkage of the volume during the conversion. These effects are due to (1) smaller size of water molecule, (2) lower coordination ability (donor number) of water, (3) lower boiling point of water (also related to (2) since it depends on the intermolecular interactions in the liquid state). These factors will serve as the criteria for the choice of solvent used in **PV** formation process. Ideally there should be no volume change to produce smooth solid surface, thus a way to construct three-dimensional **PV** structure without forming two-dimension fibrous structures would serve as a method to improve the quality of **PV** crystals. The facts that **INT-W** can exist only in the presence of high concentrations of MAI and that water vapor treatment of **PV** reverts it back to **INT-W**, indicate that when **PV** is left in the presence of water it can gradually produce **PI** by losing MAI over time. The detailed chemical picture

of the effect of water presented here will rationalize the phenomenological observations regarding the presence of water in **PV**-based solar cells reported up to now and further support development of **PV**-based solar cell fabrication processes.

3.3 Experimental section

3.3.1 Preparation of fibrous INT-W [$(MA^+)_2(PbI_3^-)_2{\cdot}(H_2O)_2$]

PbI_2 (184 mg, 0.4 mmol) and MAI (318 mg, 2.0 mmol) were mixed in water (1.0 mL), and immediately it produced precipitates of **INT-W**. The suspension was heated to 90 °C for 30 min to form black **PV** suspension. When cooled to room temperature it formed fibrous crystals of **INT-W** over 2 h.

3.3.2 Fiber XRD analysis

The diffraction images for fiber X-ray analyses were collected on a Rigaku Rapid II diffractometer equipped with an IP using Cu Kα (λ = 1.5419 Å) radiation. Diffraction images were taken under the following conditions: exposure time, 1 s/ °; $d\omega$, 180°. The fiber was placed with its fiber axis perpendicular to the horizontal line. The fiber was kept under nitrogen atmosphere during measurement. The measurement temperature was controlled by a heater attached to the nitrogen generator. Image acquisition took 5 min, 3 min for exposure, 2 min for IP reading.

3.3.2.1 Conversion from INT-W to PV

INT-W fibers were prepared directly from solution. A single **INT-W** fiber was heated from 20 to 100 °C with an interval of 5 min for each 10 °C. The conversion completed when the temperature reached 100 °C.

3.3.2.2 Vapor treatment experiment

The **PV** fiber sample was kept in a saturated water vapor atmosphere for 2 h. The fiber XRD measurement was performed at 20 °C. Conversion to **PV** finished at 100 °C.

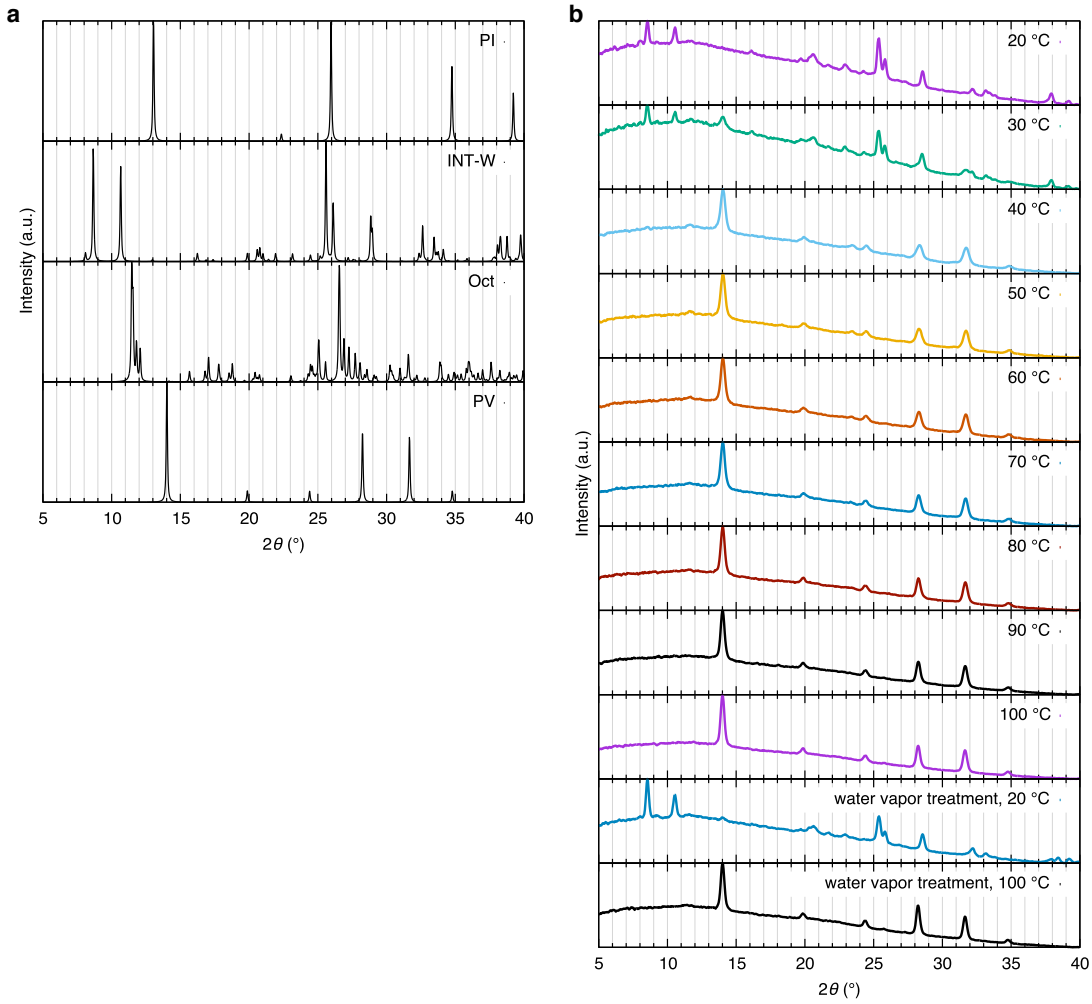

Figure 3.12. 1-D traces of XRD experiment. **a**, Reference calculated XRD patterns of **PI**,[57] **INT-W**,[63] **TA**,[62] and **PV**.[29] **b**, XRD patterns of fiber XRD measurement.

3.3.3 Crystallographic analysis

The diffraction images for X-ray crystallographic analysis were collected on a Rigaku Rapid II diffractometer equipped with an imaging plate (IP) using Cu Kα (λ = 1.5419 Å) radiation. For crystallographic analysis, the sample was removed from the mother liquor and put onto a glass slide. A crystal was chosen and then it was put on and taken off from a glass slide several times to remove liquid from its surface. The positional and thermal parameters were refined by the full-matrix least-squares method using SHELXL-2014/7 program.[71] The Yadokari-XG software was used for refinement of the structure.[72]

3.3.3.1 Crystallographic data of INT-W (−150 °C)

Formula	I_3Pb, CH_6N, O
Formula weight	635.96
Measurement temperature	123(2) K
Crystal system	monoclinic
Space group	$P2_1/m$
Lattice parameters	a = 10.4080(4) Å
	b = 4.6327(2) Å
	c = 11.2030(5) Å
	α = 90°
	β = 101.218(7)°
	γ = 90°
Volume	529.86(4) $Å^3$
Z value	2
Density (calculated)	3.986 g/cm^3
F(000)	536
Number of reflections measured	5879
Number of unique reflections	1105
R_{int}	0.1903
Number of observed reflections ($I > 2\sigma(I)$)	681
Goodness of fit indicator	0.973
Final R_1 indices [$I > 2\sigma(I)$] (R_{obs}, wR_{obs})	0.0713, 0.1148
R indices [all data] (R_{all}, wR_{all})	0.1087, 0.1300
Largest diff peak and hole	3.686/−2.770 $e \cdot Å^{-3}$

3.3.3.2 Crystallographic data of INT-F (−150 °C)

Formula	I_3Pb, C_3H_7NO, CH_6N
Formula weight	693.05
Measurement temperature	123(2) K
Crystal system	monoclinic
Space group	$P2_1/c$
Lattice parameters	a = 4.54280(10) Å
	b = 25.3099(6) Å
	c = 12.0733(3) Å
	α = 90°
	β = 96.574(7)°
	γ = 90°
Volume	1379.03(6) Å^3
Z value	4
Density (calculated)	3.338 g/cm^3
F(000)	1200
Number of reflections measured	15006
Number of unique reflections	2528
R_{int}	0.1962
Number of observed reflections ($I > 2\sigma(I)$)	1815
Goodness of fit indicator	1.020
Final R_1 indices [$I > 2\sigma(I)$] (R_{obs}, wR_{obs})	0.0736, 0.1627
R indices [all data] (R_{all}, wR_{all})	0.0958, 0.1788
Largest diff peak and hole	3.305/−4.364 e·Å^{-3}

3.3.4 SEM analysis

SEM measurement was conducted on an FEI Magellan 400L instrument at a landing voltage of 1 kV under a reduced pressure of 5×10^{-5} Pa.

Chapter 4.

Phase stabilization of lead perovskite crystals

4.1 Introduction

In previous chapters (Chapter 2 and Chapter 3) I have focused on freestanding fibers of lead perovskite materials. From this chapter on (Chapter 4 and Chapter 5) I will focus on thin-films of lead perovskite and, hence actual solar cell devices. The lead perovskite used in thin-film study has the formula $CH_3NH_3PbI_{(3-x)}Cl_x$ as discussed later and in the following chapters PV (which is not written in the bold style) denotes this formula. Thin-film state is clearly different from bulk state. The dimensions are limited, thicknesses only up to several hundred nanometers, lateral dimensions almost infinity compared to those thicknesses. Thus their chemical or physical properties can differ significantly from bulk materials.

Solar cells must be stable for practical application. High stability is one of the criteria for materials used for this energy harvesting technology. However, instability is the toughest problem of lead perovskite materials.[91-94] In this thesis I classify the instability of lead perovskite crystals into three types; (1) chemical stability, (2) thermal stability, and (3) stability based on other effects such as physical, electrochemical, or optical stimuli. Lead perovskite crystals are chemically unstable as they easily convert to fibrous polymeric intermediates when exposed to vapor of a polar solvent (Chapter 2, Chapter 3). They are also thermally unstable at >>100 °C, since they are susceptible to thermal decomposition to **PI** (Chapter 2). There can be other effects such as physical compression with sandwiching layers or electrochemical reaction that may take place under operating conditions. Those instability issues should be addressed for practical application of lead perovskite crystals to solar cells.

In this chapter I present stabilization of a crystallographic phase of PV crystals, which resulted in higher thermal stability of thin-films, hence longer lifetime of solar cell devices. PV crystals were found to be stable when impregnated with a polar polymer polyvinylpyrrolidone (PVP). Crystallites of PV obtained by PVP impregnation resulted in smaller crystallite size as well as higher thermal stability. They also had different phase transition (PT) characteristics compared to those without PVP impregnation.

The realization of small crystallite-size PV that is also stable against heat enabled fabrication of semi-transparent solar cell devices, which is a key architecture for zero-energy buildings. These solar cells overcome the problem of having very thin (50–100 nm) active layer as well as high average transmittance (AVT).

In this chapter I will mainly focus on the analysis of the crystallite properties and the solar cell studies have been performed by my co-workers Dr. Yunlong Guo and Dr. Wataru Sato.

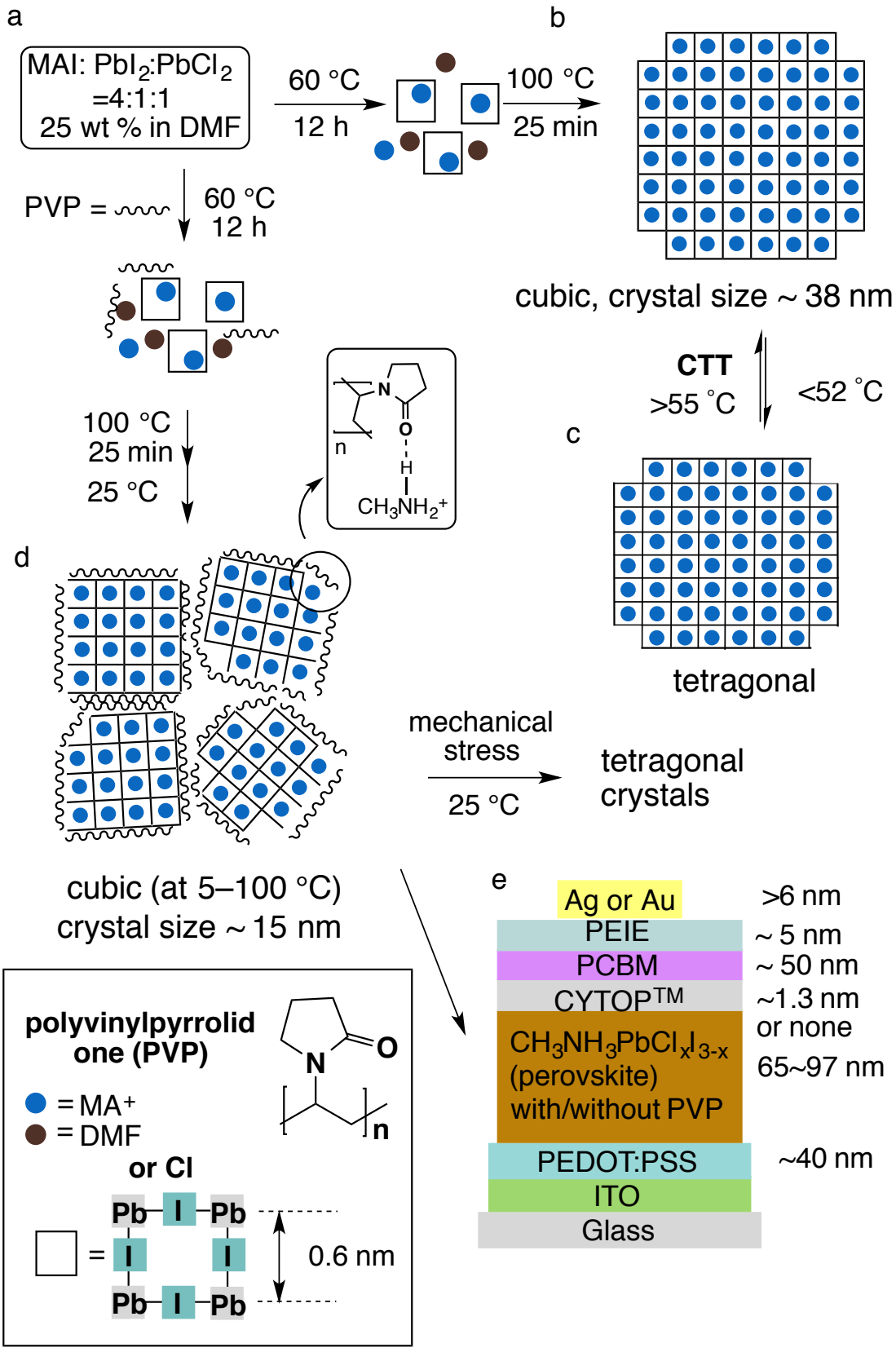

Figure 4.1. Schematic image of the formation process of nanometer-size PVP-PV crystallites and device structure. **a**, PV precursor solution. **b**, PV in the cubic phase as the result of annealing process. **c**, PV in the tetragonal phase as the result of cooling process. **d**, PV

impregnated with PVP thus in the cubic phase. **e**, Device structure of the solar cells used in this study.

4.1.1 Phase transition of lead perovskite

Lead perovskite ($CH_3NH_3PbI_3$) crystals are known to have three phases under atmospheric pressure.[37] Those are orthorhombic, tetragonal, and cubic. The restrictions of orthorhombic lattice parameters are $\alpha = \beta = \gamma = 90°$, $a \neq b \neq c$, tetragonal $\alpha = \beta = \gamma = 90°$, $a = b \neq c$, and cubic $\alpha = \beta = \gamma = 90°$, $a = b = c$. Thus, as the temperature becomes high, the crystallographic symmetry of lead perovskite crystals becomes higher. In lead perovskite crystals, the orthorhombic to tetragonal phase transition (PT) occurs at 162.2 K (−109.9 °C), and tetragonal to cubic (T-C) PT occurs at 327.4 K (54.3 °C) according to thermal analysis. This T-C PT occurs in a temperature range where solar cells can experience during operation. When this occurs in the thin film it accompanies changes in the dimensions of each crystallite (expansion/shrinkage to one dimension and shrinkage/expansion to the other two dimensions), which could give physical compression or loosening to surrounding crystallites. Since morphology of any thin-film solar cells is sensitive to morphological changes, unnecessary changes to the morphology of the thin-films during solar cell operation should be minimized.

I studied the correlation of this PT behavior with thin-film PV solar cells. As an important tool for this study I used XRD, which can track both PT behavior and various thin-film properties. Deviation from standard bulk behavior occurs when the crystallite size of materials becomes small. PVP impregnation did cause a decrease of PV crystallite size in the form of thin-films. The resulted mass of PV was studied either in the thin-film state or in the form of stacked thin-films that were scraped carefully from the substrate by a surgical blade.

4.1.2 Mixed halide perovskite

The lead perovskites used in thin-film studies are based on chloride doped one, $CH_3NH_3PbI_{(3-x)}Cl_x$. This formula is commonly used for lead perovskite solar cells studies, since chloride doping contributes to controlling the morphology[95] or increasing the diffusion length of charges.[96] The value of x in $CH_3NH_3PbI_{(3-x)}Cl_x$ is found to be on the order of 1%.[97,98] In this chapter PV denotes this $CH_3NH_3PbI_{(3-x)}Cl_x$ formula. Note that this is different from pure $CH_3NH_3PbI_3$ (**PV**) in Chapter 2 and Chapter 3, which described the bulk state of lead perovskite.

4.1.3 XRD intensity dependency on thermal factor

In the discussion of crystallite properties of PV, some elaborate knowledge of X-ray diffraction theory was used. The following description is to prove the proposition ‘X-ray

diffraction peaks at higher angles with respect to lower angle peaks of the same crystallographic planes (e.g. (400) vs (100)) reflect thermally less active region of the crystallites.'

Bragg diffraction occurs in samples where a number of planes that have the same structure are stacking with the same inter-planar distance, often denoted as Bragg condition, $n\lambda = 2d \sin\theta$. The particular concern here is diffraction intensity dependence with respect to thermal factors. Thermal factors here denote vibration of atoms in each crystallographic plane of interest. It is often visualized in the form of thermal ellipsoid in crystallographic data. The larger the vibration of the atom is, the smaller the diffraction intensity that comes from the plane containing the atom becomes. Thus when dealing with crystallites that have significant deviation in the degree of atom vibration in their interior and exterior the XRD pattern differs from calculated pattern. In such case, the diffraction peaks at higher angles do not reflect highly vibrating regions of the crystallite, thus only less vibrating regions contribute to the signal (see Section 1.4.2).

Since each crystallite has dangling regions in its exterior, and rigid regions are in its interior, the diffraction peaks in the lower angles reflect almost the whole system while those in the higher angles reflect only rigid interior regions of the crystallite. Thus by following the intensity difference of the diffractions that come from the same crystallographic plane (e.g. (100), (200), (300), and so on) one can obtain the 'depth profile' of the crystallites.

4.2 Results and discussion

4.2.1 Preparation of PVP-PV thin-films

PV thin-films doped with PVP (*x* wt% PVP-PV) was formed either on glass/ITO or glass/ITO/PEDOT:PSS surface. A precursor solution was prepared by mixing 25 wt% of MAI, PbI_2, and $PbCl_2$ (4:1:1 molar ratio) in DMF with *x* wt% of PVP and heating at 60 °C for 12 h. The solution was spin-coated on the substrate. The thin-film was annealed at 100 °C for 25 min, followed by rapid cooling to room temperature.[99]

4.2.2 DSC analysis

The PT behavior of *x* wt% PVP-PV thin-films was first measured by differential scanning calorimetry (DSC). DSC is a standard method for bulk materials to trace their PT temperatures, enthalpies, and entropies. For the purpose of investigating the intrinsic properties of lead perovskite itself, the films were deposited directory on glass/ITO surface, not on a PEDOT:PSS surface. The samples were carefully scraped off from the surface by a surgical blade in order not to induce any property change.

The sample without PVP impregnation (0 wt% PVP-PV) showed an endothermic peak at 55 °C for the heating process and exothermic peak at 52 °C for the cooling process during the

heating/cooling cycles between −50 °C and 100 °C (Figure 4.2a). This behavior is similar to that of pure $CH_3NH_3PbI_3$ without chloride doping. The slightly lower PT temperature (57 ° vs 55 °C) is due to mixing with chloride which contributed to the decrease of entropy thus to the higher stability of higher temperature phase as in the case of freezing-point depression phenomenon. By contrast in the same traces of 3 wt% PVP-PV there was no peak in the cooling process and a broad peak around 42 °C in the heating process. This implies that at lower temperatures the sample is not in equilibrium and changes its phase when the sample is kept at lower temperatures.

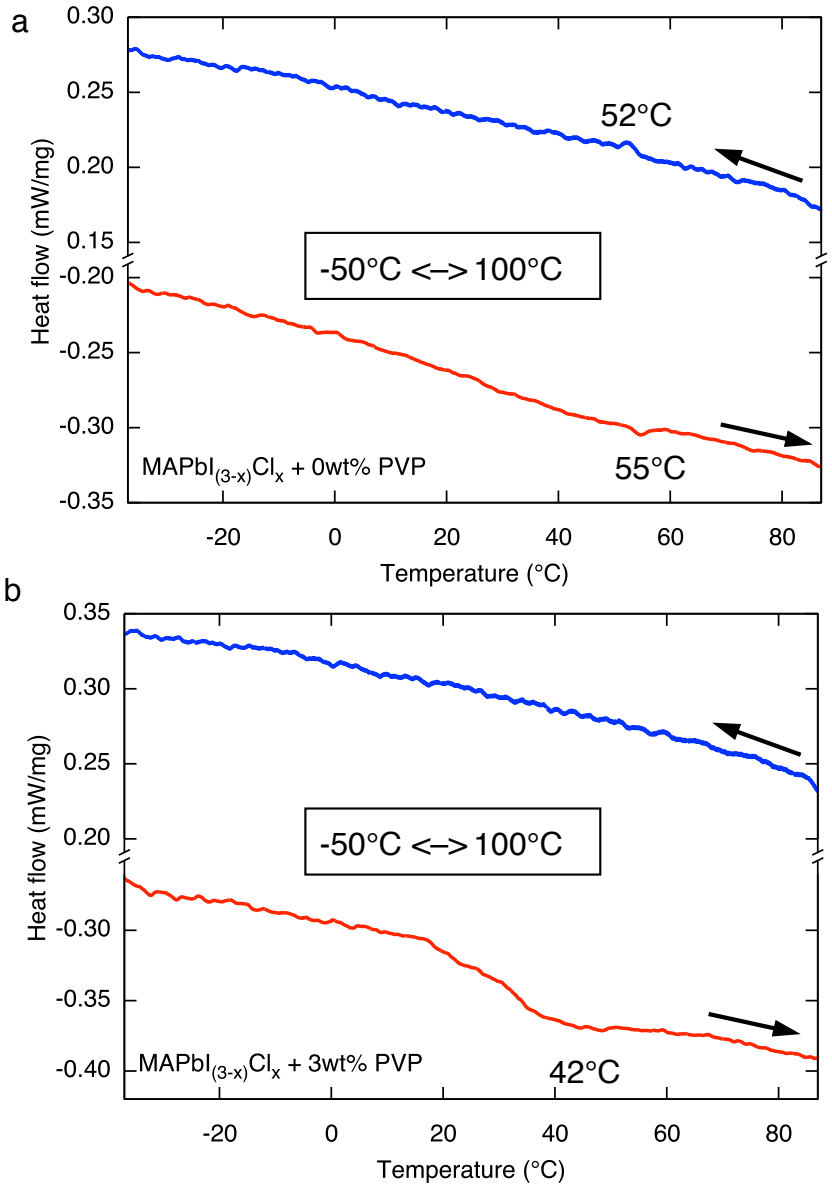

Figure 4.2. DSC traces of *x* wt% PVP-PV scraped off from the glass/ITO substrate. **a**, 0 wt% PVP-PV. **b**, 3 wt% PVP-PV.

In order to elucidate at which temperature range this behavior occurs, measurements at a different temperature range were performed. Surprisingly, in the temperature range between 5

°C to 100 °C the broad peak of 3 wt% PVP-PV was not observed (Figure 4.3b). Thus in this temperature range 3 wt% PVP-PV does not have any thermally detectable changes. The same measurement of 0 wt% PVP-PV had the same behavior as the one between −50 °C and 100 °C.

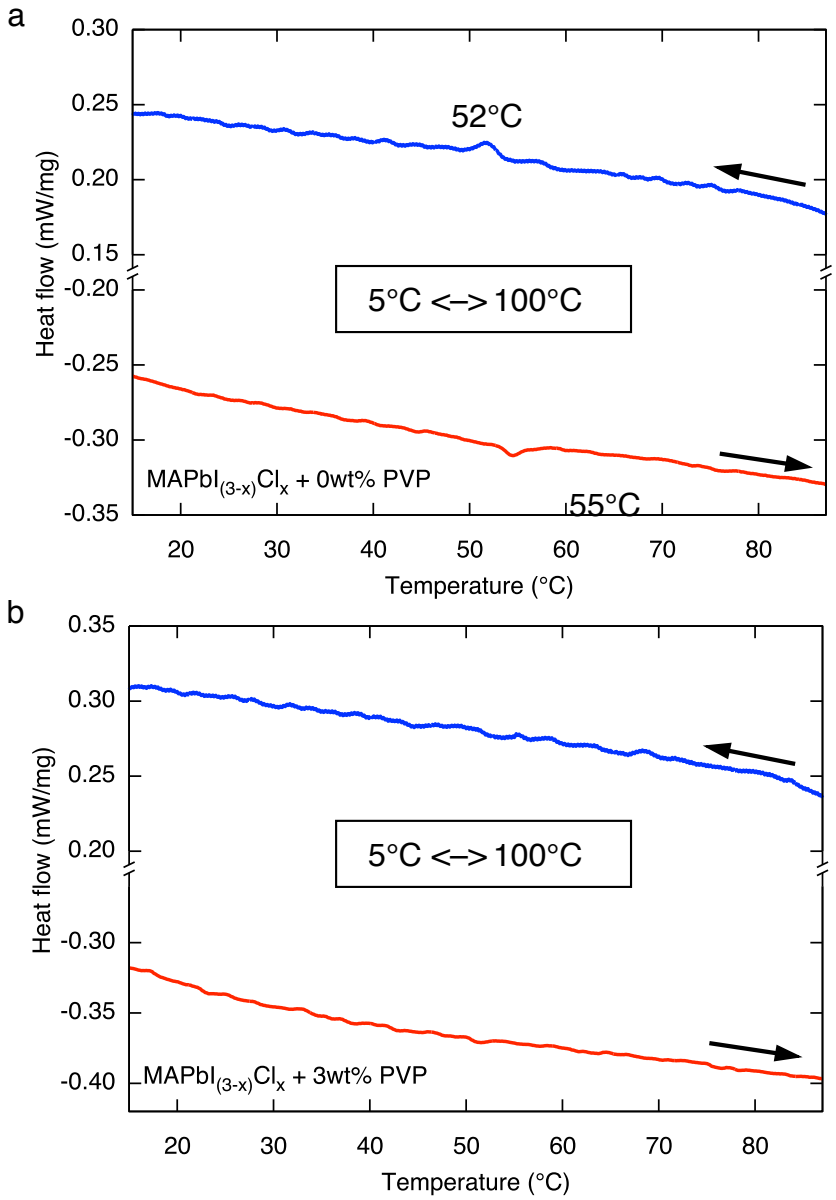

Figure 4.3. DSC traces of *x* wt% PVP-PV (x = 0 or 3) scraped off from the glass/ITO substrate in the range of 5 °C and 100 °C. **a**, 0 wt% PVP-PV. **b**, 3 wt% PVP-PV.

4.2.3 Morphology analysis of PVP-PV thin-films

The surface morphology of *x* wt% PVP-PV samples was analyzed by atomic-force microscopy (AFM) and SEM measurements. The AFM images in Figure 4.4a–c show the roughness of each sample. The thin-film of 0 wt% PVP-PV had larger roughness (R_q, root mean square) than 3 or 6 wt% PVP-PV (14.6 nm vs 3.1 nm or 2.9 nm). This in in good agreement with the SEM images in Figure 4.4d–f taken for corresponding samples.

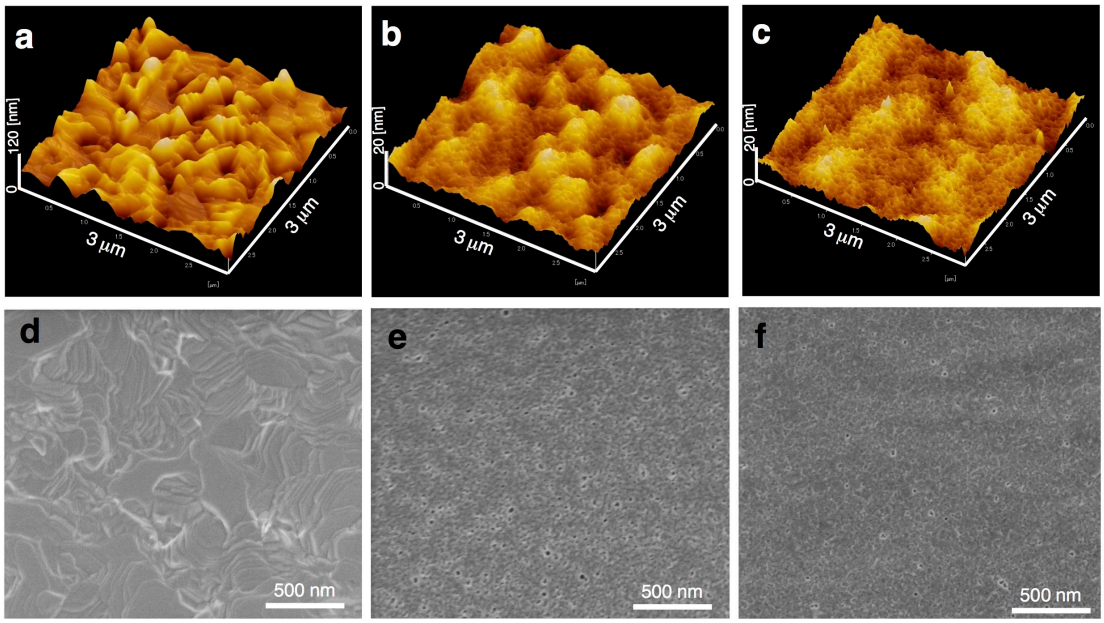

Figure 4.4. Morphology analysis of *x* wt% PVP-PV thin-films on glass/ITO/PEDOT:PSS surface. **a**, AFM image of 0 wt% PVP-PV. **b**, 3 wt% PVP-PV. **c**, 6 wt% PVP-PV. **d**, SEM image of 0 wt% PVP-PV. **e**, 3 wt% PVP-PV. **f**, 6 wt% PVP-PV.

4.2.4 Thin-film XRD analysis of PVP-PV

Thin-film XRD analysis of samples prepared on glass/ITO/PEDOT:PSS indicated distinctive properties of PVP-PV samples. First low-angle diffractions will be discussed and then high angle diffractions using stacks of thin-films will be discussed. Since PV has two crystallographic phases in the operating conditions of solar cells, here I start from naming each diffraction peak. The left most peak in Figure 4.5a is denoted P1, which is the average of (110) and (002) of the tetragonal phase and/or (100) of the cubic lattice. In the same manner P2 is the average of (220) and (004) of the tetragonal phase and/or (200) of the cubic lattice, P3 the average of (330) and (006) of the tetragonal phase and/or (300) of the cubic lattice, P4 the average of (440) and (008) of the tetragonal phase and/or (400) of the cubic lattice.

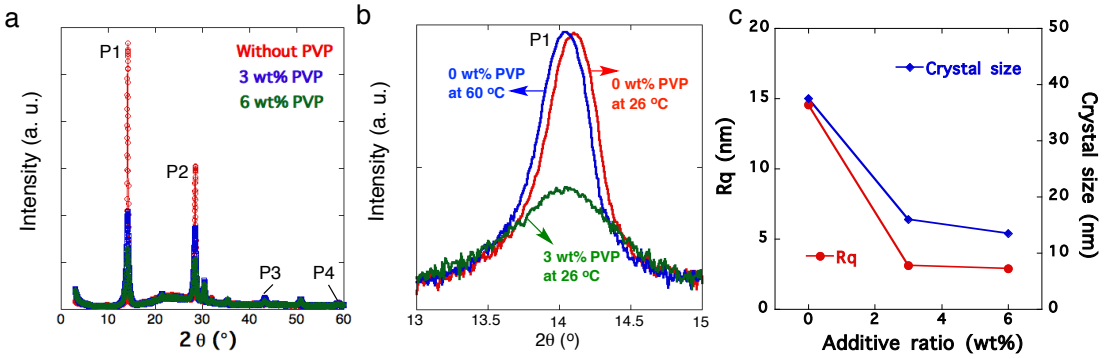

Figure 4.5. XRD patterns of thin-film samples. **a**, wide-range diffraction pattern of *x* wt% PVP-PV. **b**, P1 peak of the samples. **c**, Crystallite size and R_q in **Figure 4.4**.

The addition of PVP caused the resulting thin-films to have lower peak intensity in the XRD pattern, as in Figure 4.5b. This behavior accompanied increase in half-width-at-half-maximum (HWHM) values of diffraction peaks. From this information crystallite sizes were calculated using Scherrer equation. Scherrer equation gives minimum crystallite size of the sample. For this calculation spherical shape of the crystallites was used in accordance with the BFDH morphology analysis in Figure 2.6. The calculation revealed the crystallite size of 35–40 nm for 0 wt% PVP-PV, 15 –17 nm for 3 wt% PVP-PV, and 12–15 nm for 6 wt% PVP-PV. The crystallite size obtained for 3 or 6 wt% PVP-PV sample corresponds to dimensions of approximately 25 × 25 × 25 units of cubic lead perovskite unit cells. The crystallite size analysis has the same trend as AFM analysis (Figure 4.5).

The comparison of *d*-spacing obtained from P1–P4 gave detailed view of the structure of crystallites. The *d*-spacing values obtained from P1–P4 of 0 wt% PVP-PV had ranged in 6.270–6.280. By contrast those obtained for 1–10 wt% PVP-PV had larger deviations. The difference was most prominent for *d*-spacing values obtained from P1. The *d*-spacing of the P1 peak of 1 wt% PVP-PV was 6.293 Å, that of 3 wt% PVP-PV was 6.308 Å longest among samples of 0–10 wt% PVP-PV. The *d*-spacing from P4 had only a small deviation from 0 wt% PVP-PV, less than 6.28 Å in any case. Those of P2 or P3 ranged in between P1 and P4. Given that *d*-spacing obtained from higher diffraction angles reflects thermally less vibrating regions of the crystallite, one can conclude that the crystallite of 3 wt% PVP-PV has the largest crystallite deformation among those samples. This behavior was also the same in the measurements at 60 °C, where the crystallites are in the cubic phase in any case.

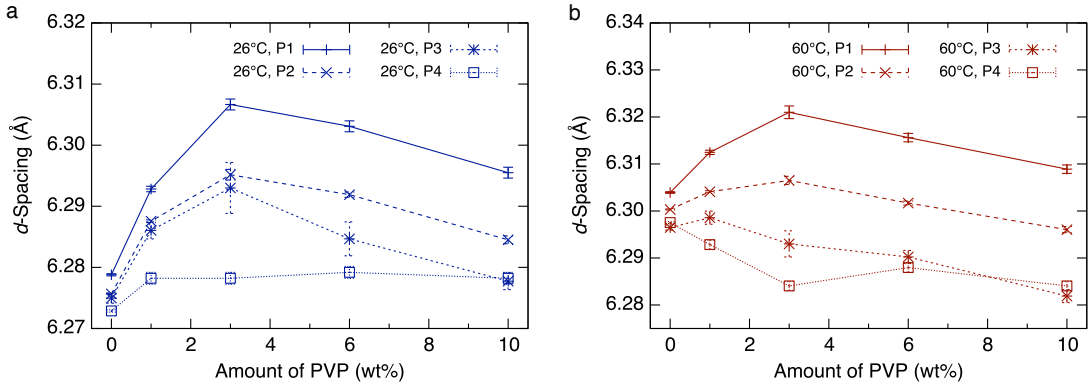

Figure 4.6. *d*-Spacing of *x* wt% PVP-PV thin-films calculated from thin-film XRD measurement. **a**, At 26 °C. **b**, At 60 °C.

The fact that 3 wt% PVP-PV has the largest crystallite deformation indicates that in this sample each crystallite hardly retains the bulk behavior of PV, the properties can significantly deviate from the standard behavior. Since the tetragonal phase of lead perovskite is partly maintained by the frozen motion of methylammonium cations in the crystal,[37,100,101] with such

deformation such 'frozenness' cannot necessarily be maintained thus can cause stabilization of the higher temperature cubic phase.

In order to view this behavior more clearly, XRD measurements of stacks of samples were performed with respect to the high angle diffraction peak P4 (Figure 4.7). The measurement data of 0 wt% PVP-PV showed standard behavior of lead perovskite as in DSC analysis. The diffraction data in the range of 57 ° to 60 ° had two peaks that come from the tetragonal phase at 26 °C as well as −50 °C, while only one peak at 60 °C. On the contrary in the measurement data of 3 wt% PVP-PV was only one peak at 26 °C as well as 60 °C, only just-discernable two peaks of the tetragonal lattice at −50 °C. Interestingly, kneaded sample of 3 wt% PVP-PV exhibited standard tetragonal characteristics at 26 °C, more clearly at 50 °C. This indicates due to coalescence of the crystallite by mechanical forces they merged together to make larger crystallites thus exhibited closer properties as 0 wt% PVP-PV, which has a larger crystallite size.

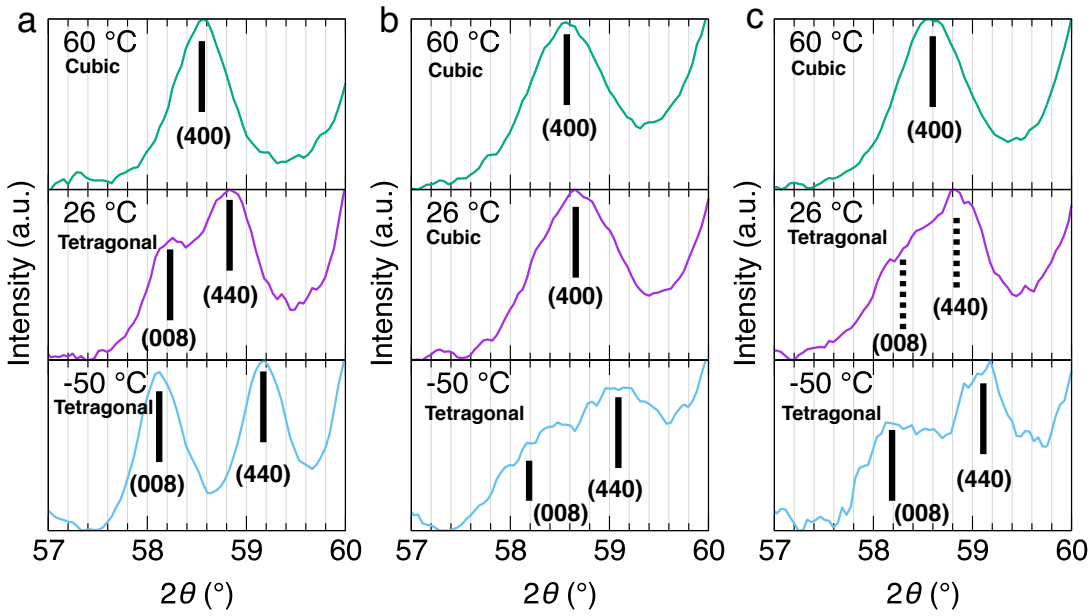

Figure 4.7. High angle XRD patterns using stacks of thin-film samples. **a**, 0 wt% PVP-PV. **b**, 3 wt% PVP-PV. **c**, Kneaded 3 wt% PVP-PV.

According to XRD analysis, impregnation with PVP resulted in smaller crystallite size of lead perovskite. XRD measurements indicated larger deformation for 3 wt% PVP-PV in comparison with 0 wt% PVP-PV or 6–10 wt% PVP-PV samples. Such larger deformation resulted in the stabilization of the higher temperature phase of PV.

4.2.5 IR analysis

Infrared spectroscopy (IR) analysis was performed to elucidate the interactions of PVP with PV. The measurement was performed for the samples prepared directory on glass/ITO

surface in order to prevent interaction with PEDOT:PSS. The evolution of C=O stretching signal appeared at 1640 cm^{-1} as the amount of PVP additive increases. This signal position is loosened compared to pure PVP sample, which gave a C=O stretching peak at 1660 cm^{-1}. This indicates that the C=O groups of PVP interacted with basic MA^+ cations on the surface of PV crystallites. Surprisingly, there is a good correspondence between the number of MA^+ cations on the surface of crystallites and the number of C=O groups of PVP in the system. The number of MA^+ cations is equal to the number of PV unit cells on the surface of crystallites. The crystallite size is calculated from Scherrer equation to be 15 nm. From this number one can calculate that approximately 13% of PV unit cells are on the surface of crystallites. This number is in the same order to the mole percent of the C=O groups of PVP against PV, which is calculated to be 14 mol%. Thus each C=O group can interact with the surface MA^+ ions in 3 wt% PVP-PV sample. There was only one peak assigned to symmetric vibration of NH_3 in the samples of 0–10 wt% PVP-PV, indicating that in all samples the MA^+ cations are rapidly moving in the time scale of IR measurement (ps scale). This signal is loosened for samples with PVP-additive (1460 cm^{-1}) compared to 0 wt% PVP-PV (1464 cm^{-1}).

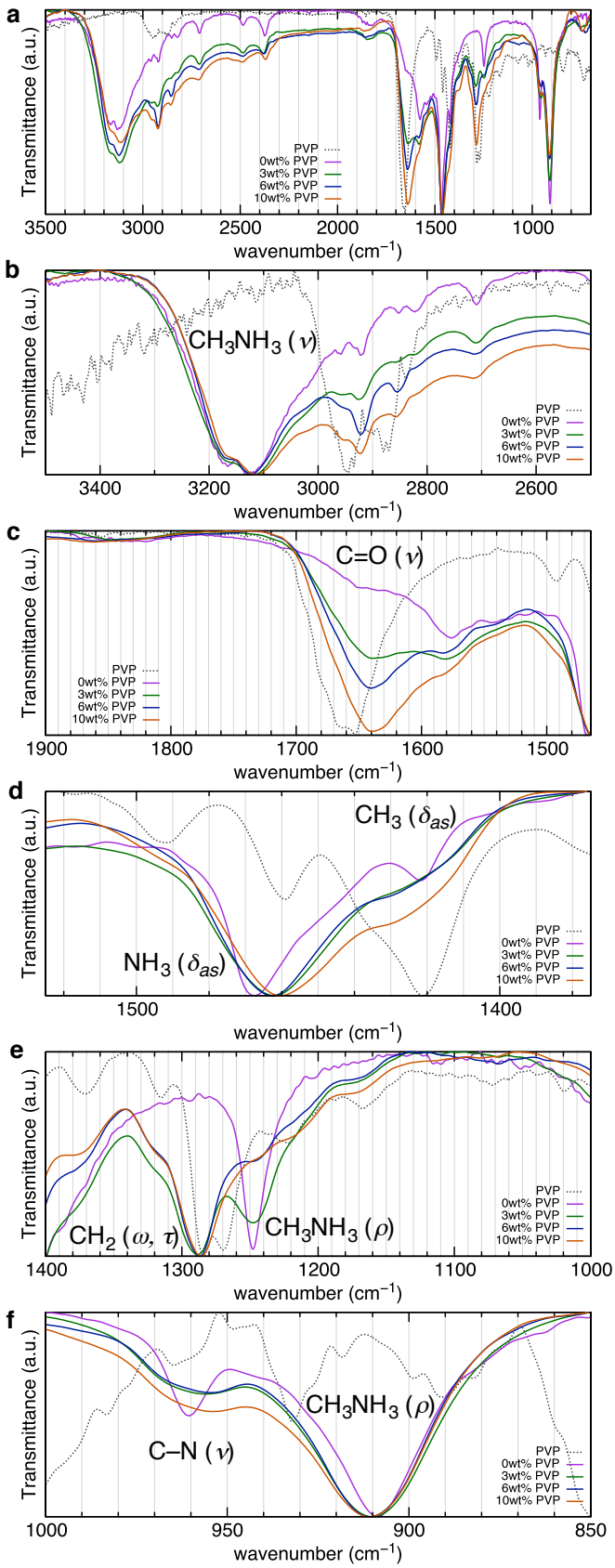

Figure 4.8. IR spectra of *x* wt% PVP-PVs with various PVP doping ratio. **a**, 3500–700 cm^{-1}. **b**, 3500–2700 cm^{-1}. **c**, 1900–1500 cm^{-1}. **d**, 1500–1400 cm^{-1}. **e**, 1400–1000 cm^{-1}. **f**, 1000–850 cm^{-1}.

4.2.6 Thin-film stability

Thermal stability was tested by XRD measurements at 60 °C. It revealed higher thermal stability of samples with PVP additive. The samples were prepared on glass/ITO/PEDOT:PSS substrate. 0 wt% PVP-PV sample gave **PI** signal at 12.6° after heating at 60 °C for 6 h in ambient conditions (28% humidity) (Figure 4.). This accompanied decrease of UV-Vis absorption coefficients. However, the samples with PVP additive (3 wt% or 6 wt%) showed only negligible peak of **PI** in the same conditions, which is also supported by UV-Vis spectra.

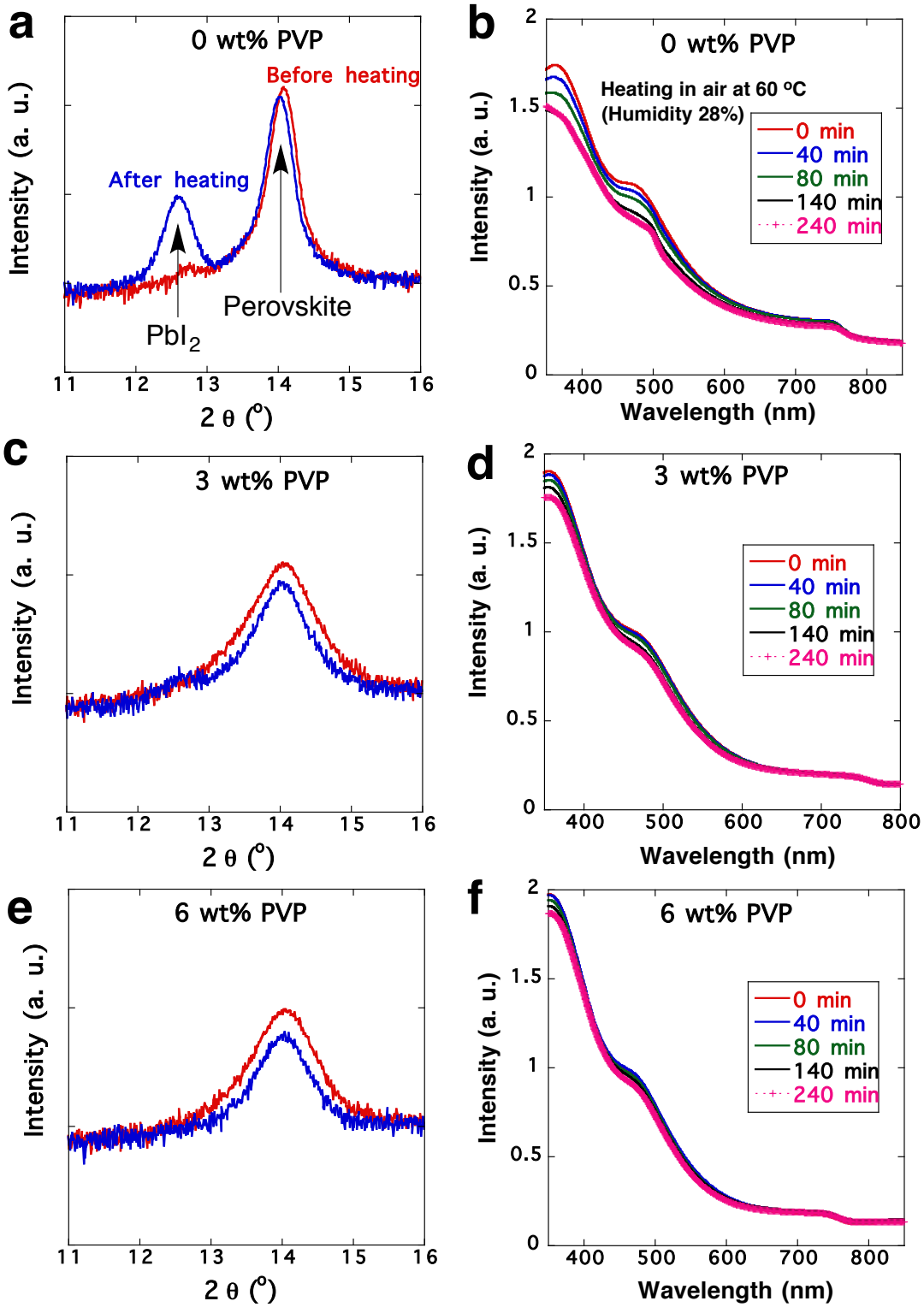

Figure 4.9. VT XRD patterns of P1 and UV-Vis spectra of *x* wt% PVP-PV samples measured in ambient conditions. **a**, VT XRD patterns of 0 wt% PVP-PV. **b**, UV-Vis spectra of 0 wt% PVP-PV. **c**, VT XRD patterns of 3 wt% PVP-PV. **d**, UV-Vis spectra of 3 wt% PVP-PV. **e**, VT XRD patterns of 6 wt% PVP-PV. **f**, UV-Vis spectra of 6 wt% PVP-PV.

4.2.7 Solar cells

Solar cells were finally fabricated by spin-coating an electron transport layer that consists of PCBM, electrode modification layer using polyethyleneimine ethoxylated (PEIE), and gold or silver electrode. Between *x* wt% PVP-PV and PCBM was a thin CYTOP layer for stability enhancement.[102] The final device structure is glass/ITO/PEDOT:PSS/*x* wt% PVP-PV/ CYTOP/PCBM/PEIE/Ag or Au. Figure 4.10 shows cross section SEM images of such devices. The CYTOP layer has a thickness of only 1.3 nm so that it is not seen in the cross section images. The thickness of *x* wt% PVP-PV increased as more PVP was added. Thus, 0 wt% PVP-PVP had thicknesses of 65–84 nm, the thinnest among three samples, 3 wt% PVP-PV 82–86 nm, 6 wt% PVP-PV 92–97 nm.

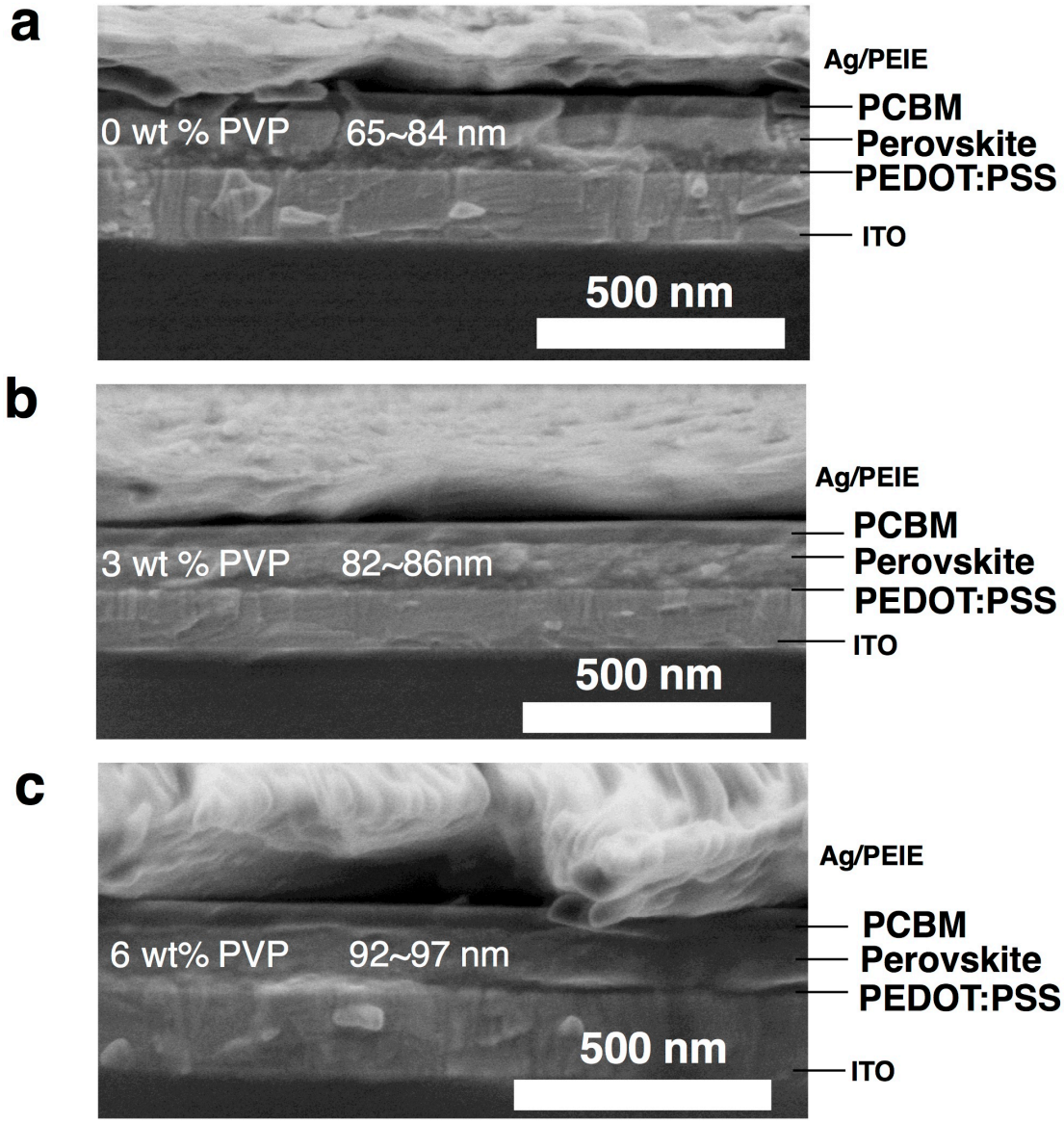

Figure 4.10. Cross section SEM images of glass/ITO/PEDOT:PSS/*x* wt% PVP-PV/PCBM/PEIE/Ag. **a**, 0 wt% PVP-PV. **b**, 3 wt% PVP-PV. **c**, 6 wt% PVP-PV.

Figure 4.11 summarizes solar cell performances as well as transparency. Under AM-1.5 light of 100 mW cm^{-2} the devices based on 3 wt% PVP-PV showed an average PCE of 7.10 ±

0.24%, which is significantly higher than the control device using 0 wt% PVP-PV (5.92 ± 0.32%). This enhancement accompanied increases in AVT, shunt resistance (R_{sh}), and FF. The increase of AVT is ascribed to the smoother surface morphology as in the AFM image (Figure 4.4b) that can reduce scattering of light on the surface. This smooth morphology also contributed to higher shunt resistance, and hence FF. Increasing the amount of PVP additive resulted in higher series resistance thus lowering FF and PCE (3.73 ± 0.25%), while AVT was maintained. This suggests excess amounts PVP act as insulator that significantly deteriorates solar cell performance.

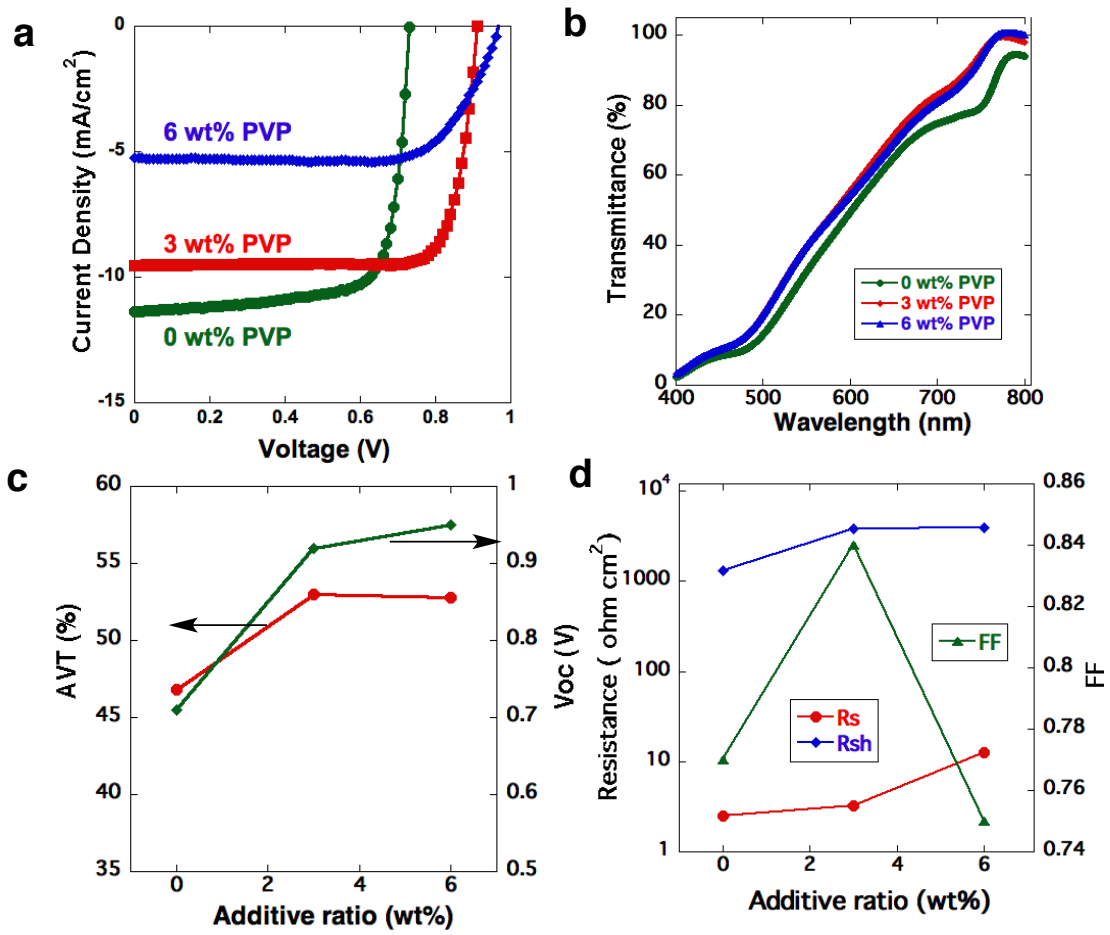

Figure 4.11. Solar cell performances of *x* wt% PVP-PV. **a**, *J*–*V* curves. **b**, Transmittance spectra. **c**, AVT values. **d**, Shunt and series resistance.

Finally solar cell stability was tested in ambient conditions (Figure 4.12). The device employing 0 wt% PVP-PV did not tolerate to operate over 200 h storage. The device with 3 wt% PVP-PV tolerated more than double, up to 400 h. This stability increased further by adding a thin CYTOP layer between 3 wt% PVP-PV and PCBM, thus yielding a life time of 840 h.

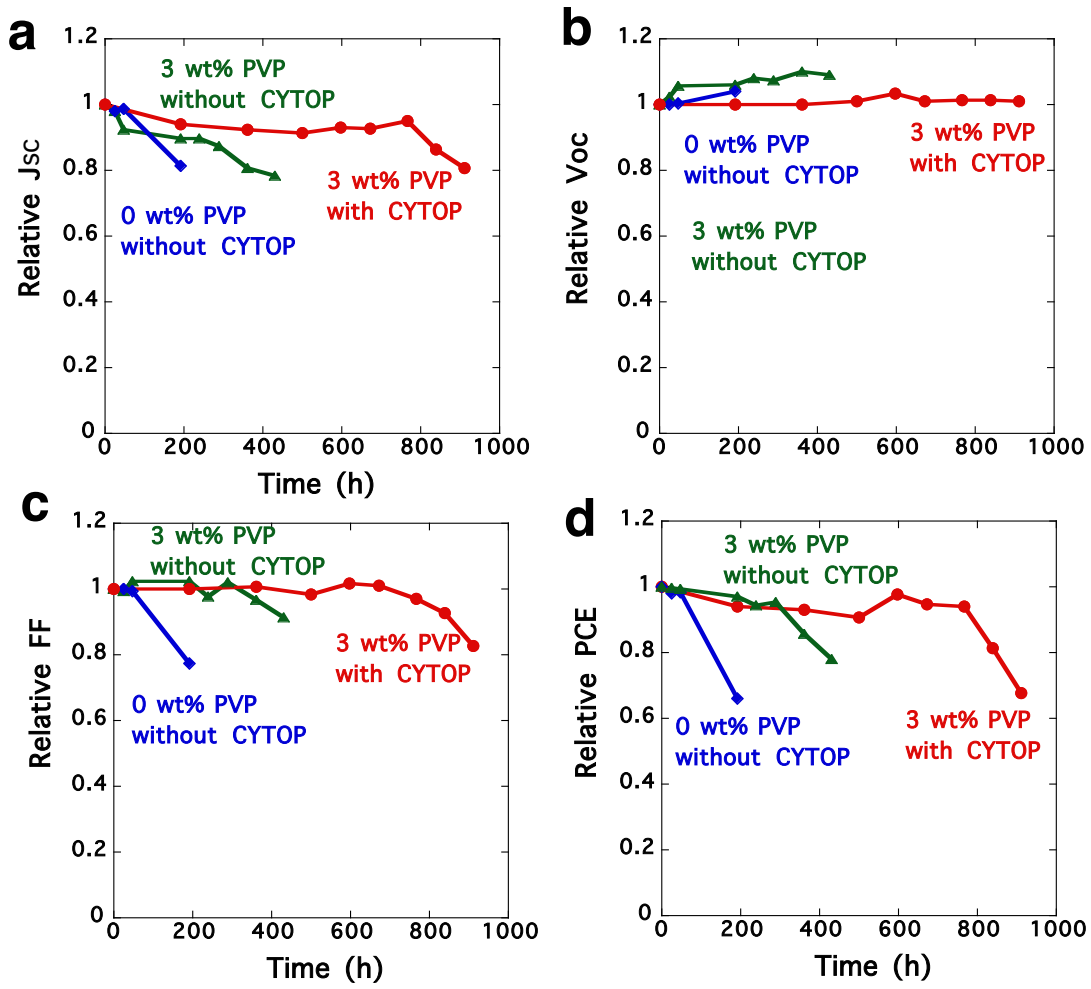

Figure 4.12. Stability test of solar cells using *x* wt% PVP-PV. **a**, Relative J_{sc}, **b**, V_{oc}. **c**, FF. **d**, PCE.

4.3 Conclusions

PVP doping of PV thin-films resulted in a decrease of crystallite size. This effect at the same time brought significant distortion of the crystallites, specifically expansion of the cell lattice, thus enabling the crystallites to maintain the cubic phase even at room temperature. This prevented the crystallites from suffering unnecessary PT behavior during operational conditions that can cause strain around each crystallite due to expansion/shrinkage of the cell lattice, resulted in higher thermal stability of the PV in its thin-film state as well as longer device lifetime. Expansion of cell lattice was also observed in PV thin-films formed on mesoporous TiO_x electron transport layer that enhanced the device performance.[103-105] Present study gives several new pieces of information on chemical understanding of PV crystal properties that are beneficial for those studying lead perovskite solar cell devices.

4.4 Experimental section

4.4.1 DSC analysis

DSC analysis was performed on a NETZSCH DSC 204 F1 Phoenix analyzer. Samples (~2 mg) were placed in an aluminum pan. Measurements were performed with a heating rate of 10 K/min under nitrogen atmosphere.

4.4.2 SEM analysis

SEM measurement was conducted on an FEI Magellan 400L instrument at a landing voltage of 1 kV under a reduced pressure of 5×10^{-5} Pa.

4.4.3 AFM analysis

AFM observations of *x* wt% PVP-PV thin-films were performed on a Bruker Multimode 8 instrument in air.

4.4.4 Thin-film XRD analysis

Thin-film XRD experiments were performed on a Rigaku SmartLab X-ray diffractometer equipped with a scintillation counter. The measurement employed Cu Kα (λ = 1.5419 Å) radiation at 9 kW (45 kV, 200 mA) power. The intensity was collected as a 0.02° step $2\theta/\omega$ scan of 3.0–40.0° with a scanning speed of 3° min^{-1}. For thin-film stability evaluation, a TCU 150 temperature control unit (Anton Paar) was used in air. The XRD measurements of a peeled sample were performed on a RIGAKU R-AXIS RAPID II diffractometer equipped with an imaging plate detector, using Cu Kα (graphite monochromated, λ = 1.5419 Å) radiation.

4.4.5 UV-Vis absorption spectra measurement

The UV-Vis spectra of the PV thin-films on glass/ITO were recorded on a JASCO V-670 spectrophotometer.

4.4.6 ATR IR measurements

The ATR–IR spectra were recorded on a JASCO FT-IR-6100 spectrometer. Measurements were performed under a nitrogen atmosphere at room temperature.

4.4.7 Device fabrication

In a nitrogen-filled glove box, dry MAI, PbI_2 (Aldrich, 99.999%, purified by vacuum oven twice), and $PbCl_2$ (Aldrich, 99.999%) were dissolved in *N*,*N*-dimethylformamide (Tokyo Chemical Industry Co., 99.5%) with a mole ratio of 4:1:1 and stirred for 12 h at 60 °C with 0–6 wt % of PVP (40K, Aldrich) to obtain a precursor solution. The concentration of PV precursor solution was kept constant at 25 wt % (except for PVP mass).

The devices were fabricated according to the following typical procedure. An ITO layer on the glass substrate was 145 nm thick with a sheet resistance of 8 Ω/square. The surface

roughness, R_q, was 0.7 nm and the R_{max} was 8.1 nm. Prior to the formation of the buffer layer, the patterned ITO glass was ultrasonically cleaned using a surfactant, rinsed with water, and then given UV–ozone treatment. A PEDOT:PSS solution (AI4083) was spin-coated on the ITO surface at 500 rpm for 3 s and then 3000 rpm for 30 s in air, and was annealed at 130 °C for 25 min under air and 20 min under nitrogen. A solution of 0–6 wt% PVP-PV precursor was spin-coated on the PEDOT:PSS surface at 6000 rpm for 30 s under nitrogen atmosphere. The thickness of PV layers can be controlled by spinning speed (6000 rpm, 5000 rpm, 4000 rpm, 3000 rpm, 2000 rpm and 1000 rpm). The film was annealed at 100 °C for 25 min. An electron-transporting layer (PCBM, 20 mg/mL in chlorobenzene) was deposited by spin-coating (2000 rpm for 30 s). PEIE (0.02 wt %, in methanol), an interface-modifying layer, was spin-coated at 6000 rpm for 30 s. The top electrode (Ag, 150 nm) was deposited via a metal shadow mask, which created a 2 mm stripe pattern perpendicular to the ITO stripe.

4.4.8 Evaluation of PV devices

Current–voltage sweeps were taken on a Keithley 2400 source measurement unit controlled by a computer. The light source used to determine the PCE was an AM1.5G solar simulator system (Sumitomo Heavy Industries Advanced Machinery) with intensity of 100 mW/cm^2. The SCs were masked with a metal aperture to define the active area of 4 mm^2.

Chapter 5.

Formation mechanism of lead perovskite crystallites on thin-films

5.1 Introduction

In this chapter I describe the process in which PV crystallites form on flat substrates by solution process. One of the main focuses of lead perovskites (PVs) is application to thin-film solar cell devices. I have already described in Chapter 2 and Chapter 3 the process in which nm- to μm-size fibrous lead perovskite crystals form. However the sizes of crystals used in thin-film solar cells are widths of nm–mm and thicknesses of several hundred nm because the crystals should be confined in thin-films.[106,107] As such there should be a huge discrepancy between the PV formation process in the form of a freestanding fibrous solid and the one in the form of multiple nm–mm crystallites. For the understanding of the conversion process occurring on thin-films one needs to analyze the process on actual thin-film substrates.

One of the key observations in the bulk state study was the acid–base reaction occurring in the chemical pathways leading to PV crystal formation. It has been seen that ligands that have higher donor numbers tend to cause the conversion of the intermediate to lead perovskite at higher temperatures. Thus among the three solvents studied (DMSO, DMF, H_2O), temperature at which the conversion completes is the highest in DMSO system (donor number 29.8), followed by DMF (donor number 26.6), and the lowest in water system (donor number 18.0) (see Table 3.1).[69]

This observation poses the possibility that an appropriate acid can catalyze the conversion pathway thus controlling the PV formation kinetics. As I have explained in Chapter 2 and Chapter 3, the conversion from intermediate species to lead perovskite results in inclination of two of the crystallographic axes of lead perovskite by 45° against initial intermediate fiber axis. This, if occurs in the thin-film deposition process, this can cause the same inclination against the normal axis of the substrate surface. There are some reports that observed this inclination. Seok *et al*. have reported that a preferred orientation of (111) was observed during their two-step PV preparation method.[108] In a simple one-step deposition this can cause randomness of the crystallographic orientation of the resulting PV crystallites, thus a method to avoid the formation of intermediate crystallites on the surface during the deposition process would serve an improvement of the overall performance as well as higher reproducibility of lead perovskite solar cells.

For the purpose of accelerating PV formation process and avoiding randomness of the crystallites deposited on flat substrates, in this chapter, a method to accelerate the formation pathway by addition of an organic acid in the precursor solution of PV will be discussed. This method indeed gave an improved crystallographic orientation and better solar cell performance. In this study, a collective set of evidence for the higher orientation of this rapid-crystallization protocol and resulting better performance of solar cells will be provided.

The discussion focuses on the morphology of PV thin-films that were obtained by just after spin-coating PV precursor solution and thin-films that were further annealed to complete the formation of PV crystallites.

In this chapter I will mainly focus on the analysis of the crystallization pathways and the solar cell studies have been performed by my co-workers Dr. Yunlong Guo and Dr. Wataru Sato.

5.2 Results and discussion

5.2.1 Sample preparation

Preparation of the precursor solution is described first. A 25 wt% solution of PbI_2, $PbCl_2$, and MAI (with a molar ratio of 1:1:4) in DMF was prepared. Then an organic acid was added. The amount of the acid was calculated as weight percent against the amount of PbI_2, $PbCl_2$, MAI (half of the amount was considered as excess, thus not counted). Organic acids used here are citric acid (CA), tartaric acid (TA), glycine hydrochloride (GLY). The solution was then stirred at 60 °C for 6 h and cooled to room temperature.

The precursor solution was spin-coated on ITO/PEDOT:PSS substrates at 4000 rpm. Some of following measurements were conducted on samples at this state. The substrate was annealed at 100 °C for 25 min. The thickness of PV layer was measured to be 140 nm by a surface profile analyzer. For fabrication of solar cells the substrate was further spin-coated PCBM, PEIE, and deposited a silver electrode. And finally coated with CYTOP for device evaluation.

5.2.2 1-D XRD analysis of thin-films

The quicker conversion of citric acid-doped thin-films than non-doped ones was distinguished by 1-D XRD measurements. Figure 5.1a, b shows XRD patterns of 0 wt% citric acid-doped PV (0 wt% CA-PV) before and after annealing. In the XRD pattern before annealing PV diffraction peaks appeared already at 2θ = 14.0° and 28.2°. Indicating that the intermediate to PV conversion already started. At the same time the diffraction peaks of methylammonium lead trichloride (2θ = 15.6°, 31.6°) were observed. This chloride perovskite serves as nuclei to initiate the crystallization of PV.[98] These peaks disappeared after annealing. From this observation one can deduce that the annealing process facilitates inter-conversion of PV and intermediates via trace solvent molecules remaining on the substrate to form well-mixed distribution of chloride ions and iodide ions. The final chloride incorporation ratio is around 3% as discussed in Chapter 4. Figure 5.1c, d shows XRD patterns of 15 wt% CA-PV before and after annealing. There is no trace of chloride perovskite even before annealing in this case. Thus in this case already at the end of spin-coating process the above reaction brings mixing of chloride ions and iodide ions. After the

annealing process the trace intermediacy peaks (2θ = 11.0°, 12.0°) disappeared, which indicates the annealing process is also required for 15 wt% CA-PV.

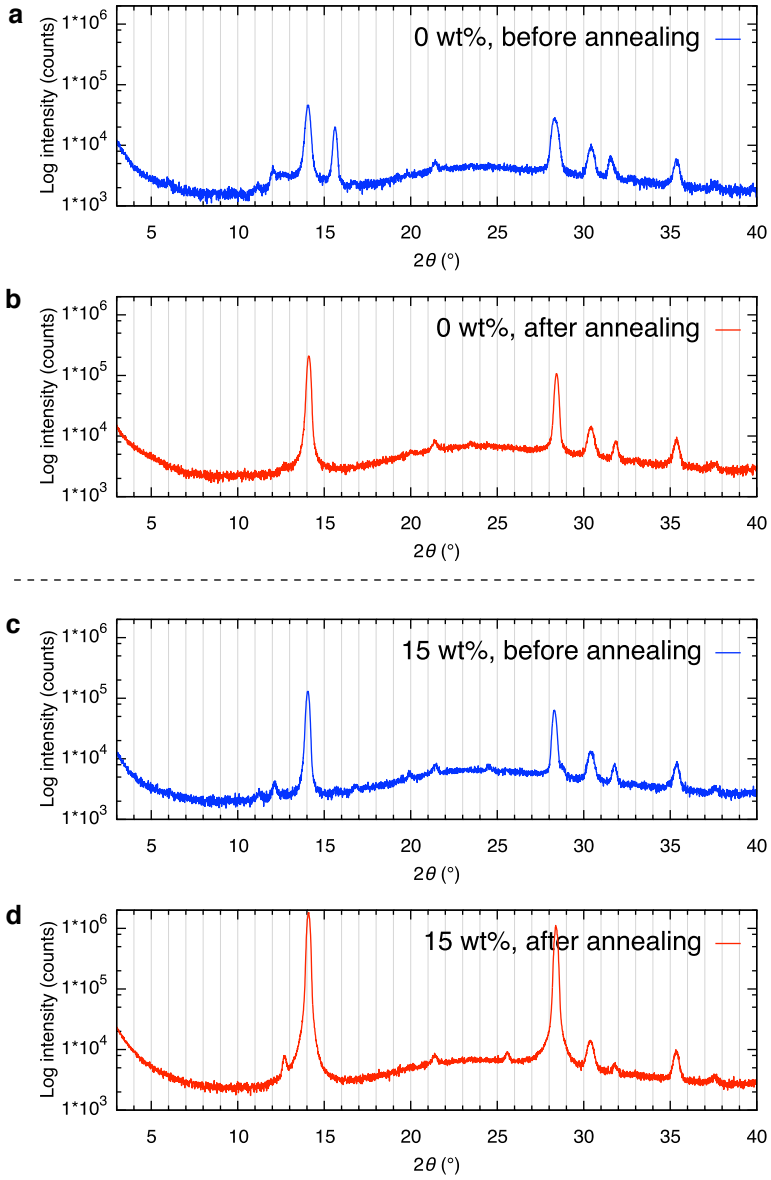

Figure 5.1. 1-D thin-film XRD patterns of 0 wt% CA-PV and 15 wt% CA-PV. **a**, 0 wt% CA-PV before annealing. **b**, 0 wt% CA-PV after annealing. **c**, 15 wt% CA-PV before annealing. **d**, 15 wt% CA-PV after annealing.

5.2.3 2-D XRD analysis of thin-films

The quantitative analysis of the enhancement of crystallographic orientation was performed by 2-D XRD analysis of the thin-film. In order to conduct this analysis, reciprocal space maps (RSMs, see Section 1.4.3) of different samples were measured. In the RSM of 15 wt% CA-PV (Figure 5.2c) there was clear orientation preference compared to non-doped one (Figure 5.2a). For this discussion each of the peaks is named in accordance with the corresponding cubic lattice indices of the actual tetragonal indices as summarized in Table

5.1. Thus the diffraction of (110) and (002) of tetragonal perovskite was named as C100 since they correspond to (100) of the higher temperature cubic phase of PV. Peaks named as C*hkl* follow this rule. One of the peaks listed in Table 5.1 is named P113, because this peak does not appear in the cubic phase due to extinction law, thus is treated as a pseudo-cubic peak that comes from (0.5 0.5 1.5) plane of the cubic lattice.

Figure 5.2a–f shows RSMs of 0 wt% CA-PV (after annealing and before annealing), 15 wt% CA-PV (after annealing and before annealing), 6 wt% TA-PV (after annealing), and 6% GLY-PV (after annealing). The diffraction spots are assigned as illustrated in Figure 5.2a–f. RMS data, when integrated along the wave vector q, have similar 1-D profile (Figure 5.3). The q value and 2θ value are connected by the following equation.[109]

$$q = \left(\frac{4\pi}{\lambda}\right) \sin\theta$$

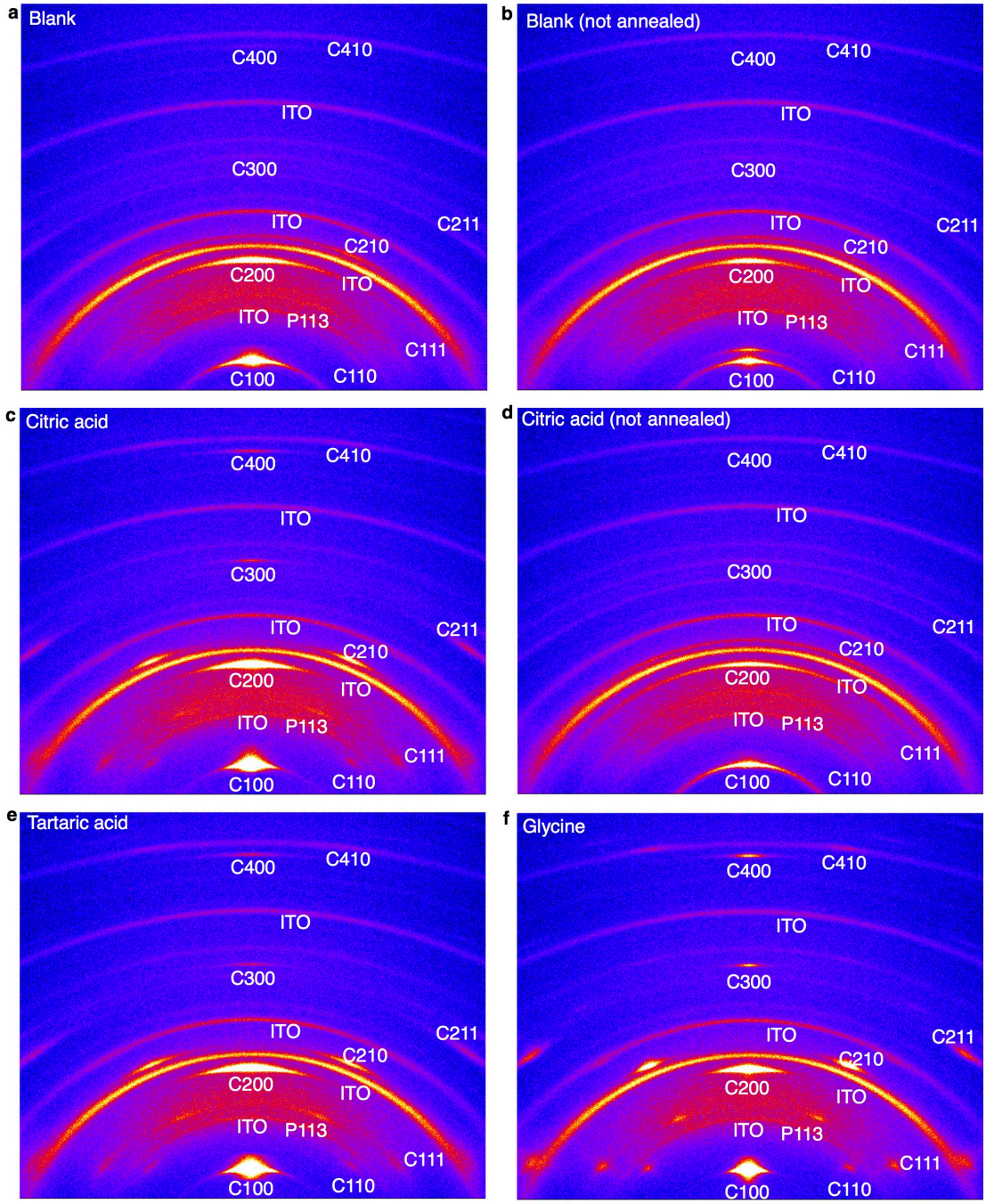

Figure 5.2. RSMs of various acid-doped samples and control blank samples. **a**, 0 wt% CA-PV after annealing. **b**, 0 wt% CA-PV before annealing. **c**, 15 wt% CA-PV after annealing. **d**, 15 wt% CA-PV before annealing. **e**, 6 wt% TA-PV after annealing. **f**, 6 wt% GLY-PV after annealing.

Table 5.1. Diffraction peaks and their angles of the data shown in **Figure 5.2**.

ID [a]	(*hkl*) (cubic)[b]	(*hkl*) (tetragonal) [c]	2θ (°)[d]	q (Å^{-1}) [e]
C100	(100)	(110), (002)	14.0	0.99
C110	(110)	(112), (200)	19.8	1.40
P113	(0.5 0.5 1.5)	(103), (211)	23.4	1.65
C111	(111)	(202), (022)	24.4	1.72
C200	(200)	(220), (004)	28.3	1.99
C210	(210)	(114), (222), (310)	31.7	2.23
C211	(211)	(204), (312)	40.5	2.82
C300	(300)	(330), (006)	43.1	2.99
C400	(400)	(440), (008)	58.7	3.99
C410	(410)	(442), (530), (118)	60.6	4.11

[a] IDs assigned to diffractions peaks. These IDs are named after corresponding (*hkl*) indices of the cubic lattice.

[b] The crystallographic planes of the cubic lattice that correspond to the peaks.

[c] The crystallographic planes of the tetragonal lattice that correspond to the peaks.

[d] 2θ angles of the peaks.

[e] q values of the peaks.

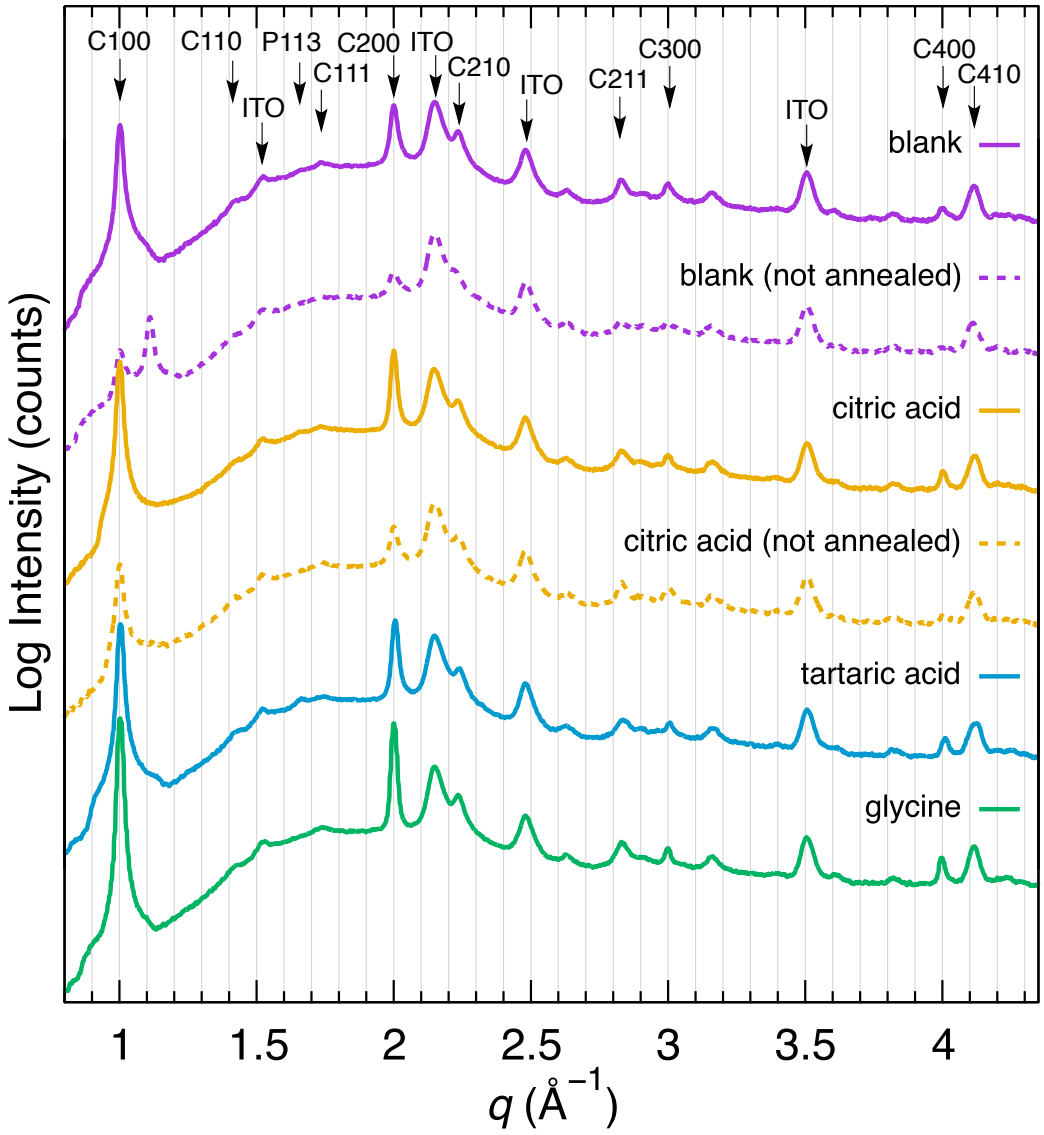

Figure 5.3. 1-D XRD patterns obtained from RSM images of acid-doped samples. The samples are from the top 0 wt% CA-PV after annealing (solid purple), 0 wt% CA-PV before annealing (dashed purple), 15 wt% CA-PV after annealing (solid orange), 15 wt% CA-PV before annealing (dashed orange), 6 wt% TA-PV after annealing (solid blue), and 6 wt% GLY-PV after annealing (solid green).

Notable differences appear when integrated along ϕ (Figure 5.4). The diffraction of C200 appears at ϕ = 90° for all samples after annealing (Figure 5.4a), indicating the crystallites prefer to orient with their (110) or (002) surface parallel to the substrate. While this tendency is the same for all samples, there is a significant difference in the full-width-at-half-maximum (FWHM) values of these signals (Table 5.2). The ϕ–I plot of the C200 diffraction of 15 wt% CA-PV after annealing (Figure 5.4c) has narrower FWHM than that of 0 wt% CA-PV after annealing (Figure 5.4a). This tendency is the same for other diffraction peaks, such as C210,

C400, and C410 (Figure 5.4b–c). When peaks in ϕ–I plots have narrower FWHM, it indicates that the orientation fluctuation of the crystallites is smaller. Thus one can conclude that the crystallites on 15 wt% CA-PV are better oriented along the substrate surface than those of 0 wt% CA-PV after annealing process. Samples before annealing either 15 wt% CA-PV or 0 wt% CA-PV (Figure 5.2b, d) have lower intensity and wider FWHM (not calculated due to lower intensity). The orientation is poorer for samples without annealing for both cases. This indicated the crystallites reorganize during the annealing process due to Ostwald ripening process discussed in Chapter 2. This fact is clearly supported by the following SEM analysis.

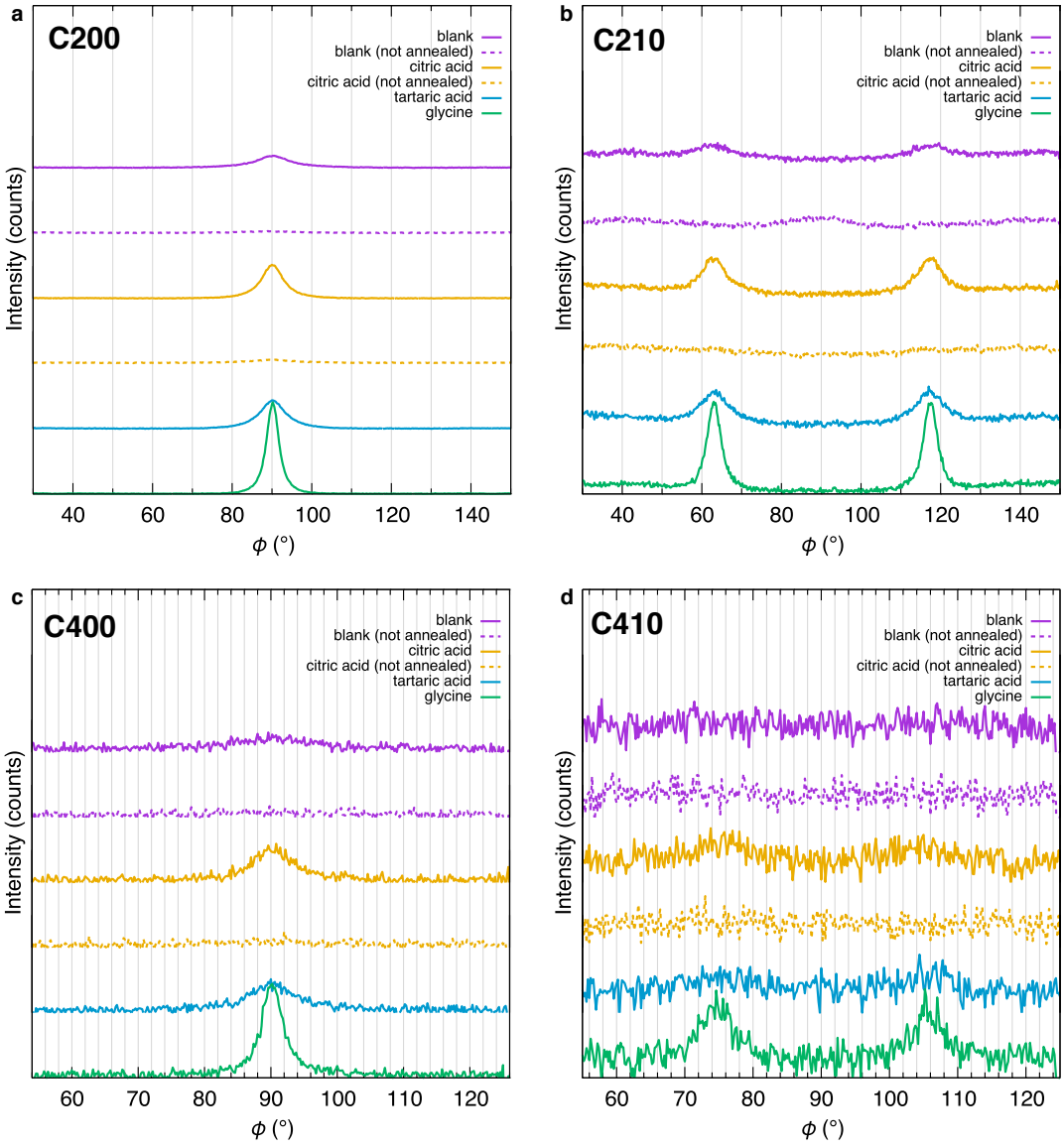

Figure 5.4. ϕ-Plot of RSMs of various samples. **a**, C200. **b**, C210. **c**, C400. **d**, C410.

Table 5.2. FWHM values of the peaks of ϕ–I plots in **Figure 5.4**. Only samples after annealing were considered. The FWHM value of C410 of additive-free PV was not determined due to low S/N ratio.

FWHM (°)	C200	C210	C400	C410
PV	10	9.7	17	nd
CA-PV	6.5	7.2	7.1	9.0
TA-PV	7.6	8.3	8.3	11
GLY-PV	3.8	4.3	3.8	5.3

5.2.4 SEM analysis

The comparison of the SEM images of x wt% CA-PV where x is 0, 6, or 15 clearly demonstrates the better orientation alignment of crystallites formed by the use of 15 wt% CA-PV (Figure 5.5). The SEM image of 0 wt% CA-PV before annealing has uniform surface morphology without clear grain boundaries (Figure 5.5a). That of the sample after annealing showed featureless morphology as well (Figure 5.5d). There were clear differences in the same set of images in 6 wt% CA-PV. The SEM image of 6 wt% CA-PV before annealing showed distinguishable grain boundaries (Figure 5.5b), which became clearer in the sample after annealing (Figure 5.5e). The thin-film of 15 wt% CA-PV before annealing has obvious grain boundaries even the sample before annealing (Figure 5.5c). The one after annealing as well has grains with sharper edges than the sample before annealing (Figure 5.5f). Because the shape of these grains is consistent with the BFDH morphology of PV (which is cubic), one can assume that these grains are composed of a single PV crystallite. This observation indicates that when forming a thin-film of 15 wt% CA-PV the crystal nuclei quickly grow larger during/after spin-coating so that the number of nuclei form on the surface is suppressed to minimum, and each nucleus can grow larger as possible.

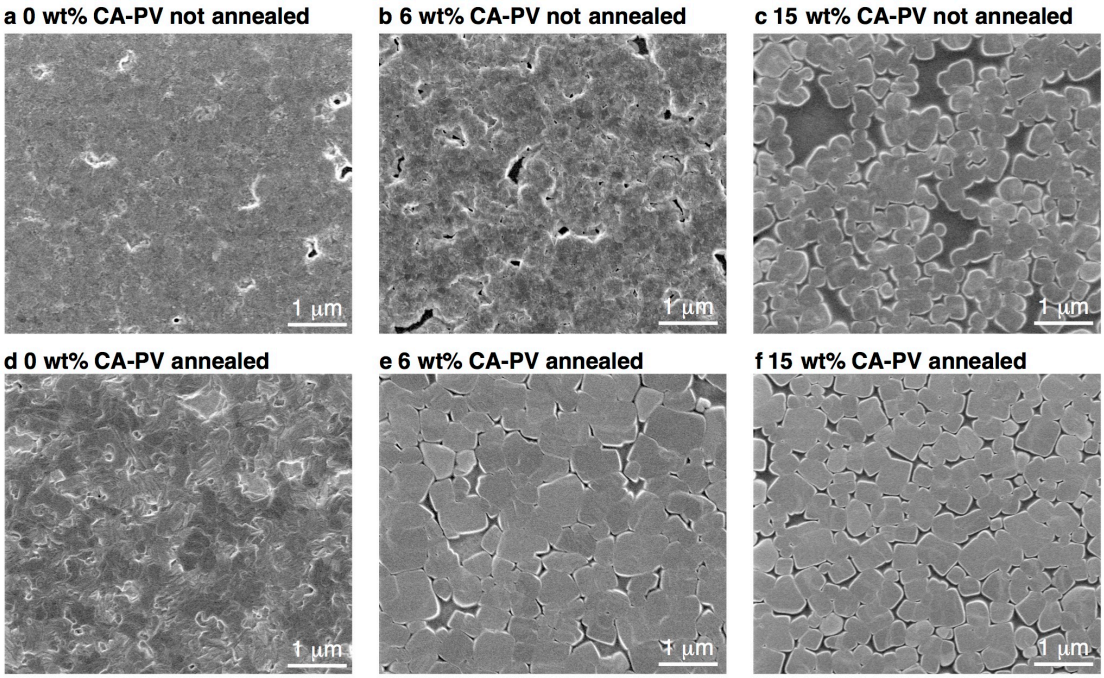

Figure 5.5. SEM images of lead perovskite thin-films with or without an organic acid additive. **a**, 0 wt% CA-PV before annealing. **b**, 6 wt% CA-PV before annealing. **c**, 15 wt% CA-PV before annealing. **d**, 0 wt% CA-PV after annealing. **e**, 6 wt% CA-PV after annealing. **f**, 15 wt% CA-PV after annealing.

Energy-dispersive X-ray spectroscopy (EDX) mapping analysis of 15 wt% CA-PV indicated that there was no PV formed between each crystallite that were seen in SEM image (Figure 5.6). Secondary electron (SE) image in Figure 5.7 clearly distinguishes grain boundaries. Signals of Pb and I in the EDX measurement are observed only from regions where crystallites occupy in the SE image. The In signals, that come form the substrate ITO, were observed in the region where SE signals were not observed. Thus one can conclude that there are no materials occupying the areas surrounded by PV grains.

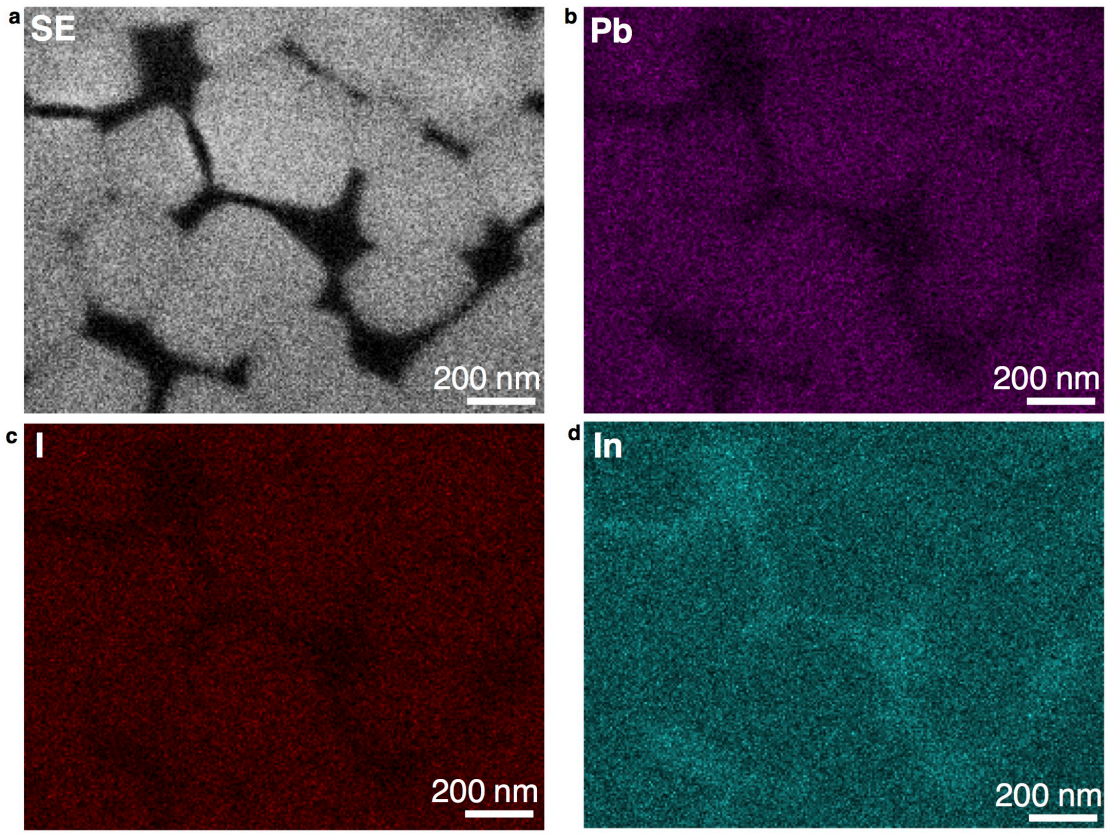

Figure 5.6. EDX mapping images of 15 wt% CA-PV thin-film measured at 10 keV. **a**, Secondary electron. **b**, Lead. **c**. Iodine. **d**, Indium.

5.2.5 AFM analysis

AFM analysis revealed the whereabouts of as-much-as 15 wt% citric acid molecules. Figure 5.7 shows an AFM image of 15 wt% CA-PV thin-film. The R_q is 8.7 nm significantly lower than the thin-film without additive (see Section 4.2.3). There were several chunks of a size of 100 to 200 nm that are not seen in SEM images. Because SEM image is not sensitive to light elements than heavy elements nor to height changes, and AFM is significantly sensitive in the height analysis, one can conclude that these chunks are made of citric acid molecules; citric acid only possesses light elements than PV. Thus the citric acid molecules, after serving as a catalysis to accelerate the formation of perovskite crystallites, excluded out to the surface of PV crystallites.

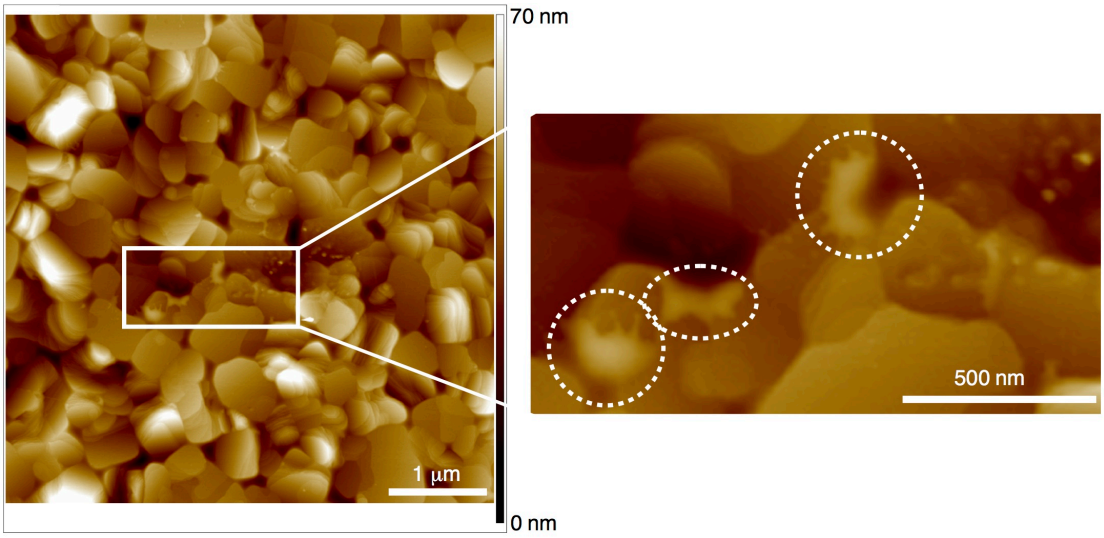

Figure 5.7. AFM analysis of 15 wt% CA-PV thin-film. The center area was expanded in the right side to show gum-like deposits of material that is assigned to be CA.

5.2.6 IR analysis

IR analysis is as a well-established method to characterize and analyze the state of organic molecules. This analysis further supported the presence of citric acid on the thin-films. For this purpose the 15 wt% CA-PV was scraped off from the substrate by a surgical blade and mounted on an attenuated total reflectance (ATR) FT-IR spectroscope. Figure 5.8 shows IR spectra of various additive amounts of PV thin-films (additive ratio varies from 0 to 20 wt%). The most distinguishable peak is C=O bond stretch which appeared at 1715 cm^{-1} (Figure 5.8c). This peak gradually increases as the amount of citric acid increases. Also CH_2 wagging signal of citric acid appeared at 1200 cm^{-1} (Figure 5.8e). CH_3 scissoring and NH_3 scissoring signals moved to lower energy region by approximately 5–10 cm^{-1} indicating the loosening of methylammonium ions in the PV crystallites by interactions with sorrowing materials (Figure 5.8d). The same was observed, with lower degree of change (approximately 5 cm^{-1}), for C–N stretch and MA rocking (Figure 5.8f). In comparison to Figure 4.8, the methylene wagging or twisting signal of citric acid has lower energy region by ca. 80 cm^{-1}, due to looser free methylene groups of citric acid compared to those of rigid five-membered rings in PVP.

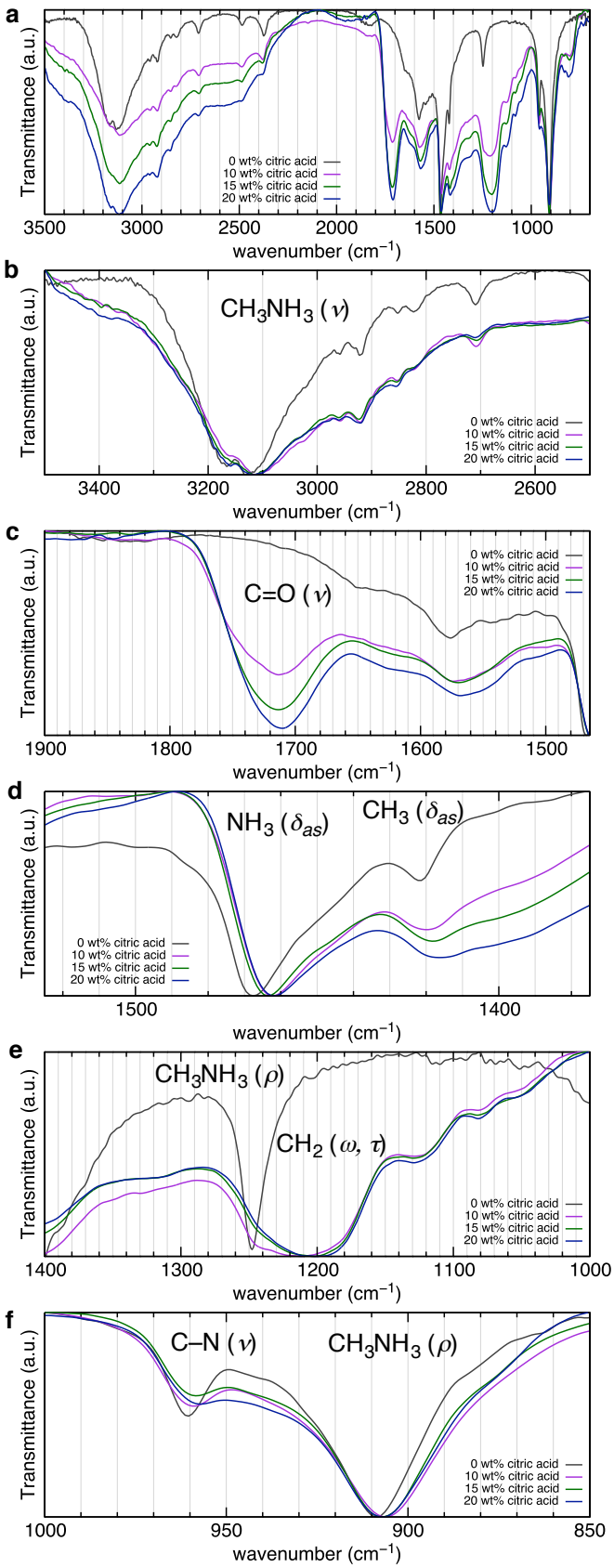

Figure 5.8. IR spectra of citric acid-doped lead perovskite. **a**, the whole region. **b**, CH_3 region. **c**, C=O region. **d**, scissor vibration region. **e**, MA^+ rocking and citric acid CH_2 vibration.

5.2.7 Solar cells

Solar cells employing better aligned crystallites obtained by addition of organic acids have better performance than those without additives. Figure 5.9 and Table 5.3 show the *J-V* curves and device parameters of solar cells using 0 wt% CA-PV and 15 wt% CA-PV. Both short-circuit current density (J_{sc}) and open-circuit voltage (V_{oc}) improved significantly, and also there was a slight increase of fill factor (FF). The higher J_{sc} indicates a higher charge generation rate as well as higher charge separation efficiency of the device using 15 wt% CA-PV than 0 wt% CA-PV. The fewer number of grain boundaries in the thin-film consists of 15 wt% CA-PV can lead to higher charge generation rates because charges cannot be generated around the grain boundaries. The smoother surface of the thin-film can contribute to higher charge separation efficiencies by facilitating charges going through the interface of 15 wt% CA-PV and neighboring layers. Fewer numbers of grain boundaries lead to fewer recombination rates,[93,110] which is beneficial for higher V_{oc} and FF. Because grains in the 15 wt% CA-PV thin-film are composed of single PV crystallites as discussed in the SEM/AFM observations, there are fewer recombination sites compared to 0 wt% CA-PV thin-films. Overall the power conversion efficiency (PCE) increased from 8.7% to 15.9%, significantly large value given that the film thickness of PV layer is only 140 nm, close to the world records that were measured for a thicker lead perovskite layer (> 500 nm).

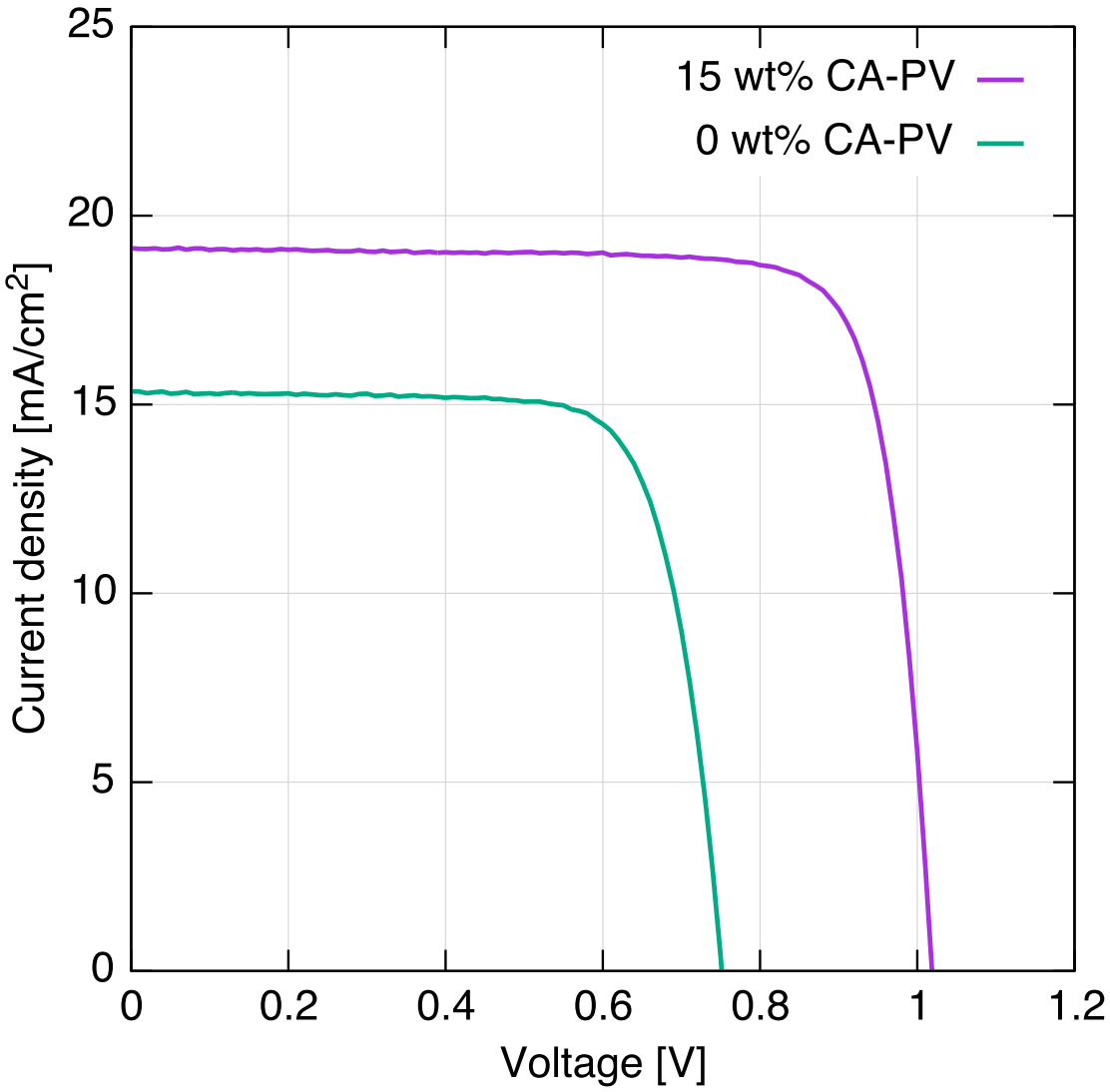

Figure 5.9. *J–V* curves of solar cell devices using 0 wt% CA-PV and 15 wt% CA-PV.

Table 5.3. Summary of the device performance parameters of **Figure 5.9**.

Lead perovskite	J_{sc} (mA/cm^2)	V_{oc} (V)	FF	PCE (%)
0 wt% CA-PV	15.35	0.75	0.76	8.7
15 wt% CA-PV	19.14	1.02	0.81	15.9

5.3 Conclusions

Doping PV precursor solutions with organic acids was proved to accelerate the formation of PV crystallites on flat substrates. The crystallites obtained in this method have better orientation alignment and thus better performance of solar cells. Citric acid-doped samples were extensively studied for the effect of organic acids. Further analysis of acid catalysis will provide better-scooped picture of the process in which PV crystallites form on flat substrates.

5.4 Experimental

5.4.1 General

Unless otherwise noted all manipulations regarding device fabrication were conducted in a nitrogen-filled glove box. Reagents were purchased from commercial sources such as TCI, Wako, or Aldrich.

5.4.2 Thin-film XRD analysis

Thin-film XRD experiments were performed on a Rigaku SmartLab X-ray diffractometer equipped with a scintillation counter. The measurement employed Cu Kα (λ = 1.5419 Å) radiation at 9 kW (45 kV, 200 mA) power. In RSM measurement, X-ray beam was collimated with CBO-*f* point line optics (ϕ < 1 mm) and detected by a HyPix-3000 two-dimensional semiconductor detector.

5.4.3 SEM analysis

SEM measurement was conducted on an FEI Magellan 400L equipped with AMETEK/EDAX Genesis APEX4 at a landing voltage of 1 kV under a reduced pressure of 5 × 10^{-5} Pa. EDX measurement was performed at 10 keV.

5.4.4 AFM analysis

AFM experiment was performed under ambient conditions using a Bruker MultiMode 8 instrument with a silicon nitride probe (SCANASIST-AIR-HR, spring constant 0.4 N m^{-1}, resonant frequency 130 kHz) in the tapping mode.

5.4.5 Synthesis of methylammonium iodide

A 33 wt% solution of methylammonium in ethanol (25 mL, 200 mmol) and a 57 wt% hydroiodic acid (26.4 mL, 200 mmol) were mixed at 0 °C in a flask. The mixture was stirred for 2 h then the solvent was removed under reduced pressure. The resulting crystalline powder was then recrystallized with ethanol, and dried under vacuum for 12 h at 60 °C to yield a white crystalline solid of methylammonium iodide (24.0 g, 75 % yield).

5.4.6 Device fabrication

PV precursor solutions were prepared in the following manner. For thinner thin-films (ca. 100 nm), first a 25 wt% solution of a mixture of PbI_2, $PbCl_2$, and MAI with a mole ratio of 1:1:4 in DMF was prepared. Acid additives were added at the same time. The amount of acid additives was calculated as weight percent unit with respect to the amount of PbI_2, $PbCl_2$. The solution was stirred at 60 °C for an appropriate time for each acid additive. Sulfamic acid-doped samples required only 0.5 h stirring. Other acids (citric acid, tartaric acid, glycine hydrogen chloride) required 6 h stirring.

Glass substrates covered with a 145 nm thick indium tin oxide (ITO) layer (resistance: 8 Ω/square; surface roughness R_q = 0.7 nm, R_{max} = 8.1 nm) were cleaned ultrasonically using a surfactant, rinsed with water. They were dried and treated with UV/ozone. A PEDOT:PSS (AI4083) layer was coated on the substrate at 500 rpm for 3 sec then 3000 rpm for 30 sec in air. The substrate was then annealed in air at 130 °C for 25 min, subsequently in a nitrogen-filled glove box at 110 °C for 20 min. For PV film deposition using 25 wt% precursor solutions, it was spin-coated at 500 rpm for 3 sec, then 4000 rpm for 30 sec, then the lid was removed at the same time the spinning was kept at 0 rpm for 10 sec, finally at 6000 rpm for 20 sec. The substrate was kept in the glove box for 10 min before a 25 min annealing at 100 °C was performed. For that using 40 wt% precursor solutions, it was spin-coated at 500 for 3 sec, 3000 rpm for 100 sec. In this case the lid was removed at 30 sec time lapse. Annealing was performed in the same manner as in the case of 25 wt% precursor solution. An electron-transporting layer (PCBM, 20 mg/mL in chlorobenzene) was deposited by spin-coating (2000 rpm for 30 s). PEIE (0.02 wt %, in methanol), an interface-modifying layer, was spin-coated at 6000 rpm for 30 s. The top electrode (Ag, 150 nm) was deposited via a metal shadow mask, which created a 2 mm stripe pattern perpendicular to the ITO stripe.

5.4.7 Solar cell evaluation

Current–voltage sweeps were taken on a Keithley 2400 source measurement unit controlled by a computer. The light source used to determine the PCE was an AM1.5G solar simulator system (Sumitomo Heavy Industries Advanced Machinery) with intensity of 100 mW/cm^2. The SCs were masked with a metal aperture to define the active area of 4 mm^2.

Chapter 6.

Perspectives

In this thesis I described studies on the formation of lead perovskite ($CH_3NH_3^+PbI_3^-$; $MA^+PbI_3^-$; **PV**) crystals and their crystallographic properties, from a chemistry-oriented viewpoint. In Chapter 2 the chemical reactions to form **PV** from lead iodide (PbI_2, **PI**), methylammonium iodide (MAI), and a polar solvent (DMF or DMSO) were described. Morphology control and reproducibility problem, two of the major concerns of the lead perovskite solar cell community, are proved to originate from delicate lead perovskite formation process that is a crystal-to-crystal conversion reaction involving reversible participation of solvent molecules. The fact that the whole process is reversible proposes also a solution to the toxicity problem: recycling of solar cells by recollecting toxic lead compounds using a polar solvent. Chapter 3 describes the detailed chemical information on how water affects the film quality and how this lead to decomposition of lead perovskite. In Chapter 4, crystallographic stability is described, which gave some implications in terms of crystallographic properties. In Chapter 5 is presented chemical information that connects crystallization pathways in the bulk solid state (described in Chapter 2) and those in the thin-film state, which has been so far chemically enigmatic.

The morphology control can be achieved by choice of solvent as well as processing conditions in which lead perovskite materials are exposed. When plumbate intermediates have significantly large volume per Pb atom the conversion gives solids rich in cracks, while when the change is smaller gives solids with smoother surface. In this regard **INT-W** is the best among three intermediates (**INT-W**, **-F**, and **-S**) since the volume change is the smallest among them. Thus, one can expect better morphology control by wisely using this water effect. Water also hasten the reversible inter-conversion between the intermediates and **PV**, which can also cause degradation of **PV** to **PI**, thus we should rationally design the use of water by controlling the intake and release timing.

One necessary task for practical application of lead perovskite solar cells is how to cope with the toxicity of lead. The reversible inter-conversion discussed in Chapter 2 poses the possibility that the cells can be recycled by reverting **PV** to **PI** and MAI by a polar solvent. Solar cells once fabricated degrade over time and when they become incapable of generating energy the active layer composed of lead perovskite can be converted back to a solution of **PI** and MAI, thus can be used for fabrication of new solar cells again.

Crystallographic phase change of lead perovskite should be considered when designing practical solar cells since it takes place during operating conditions. As a concept to suppress this behavior, miniaturization of crystallites by impregnation of polymer was proposed. This indeed brought stabilization of the higher temperature phase (cubic phase) at room temperature. This topic poses an obscured viewpoint that we should consider crystallographic phase transitions of these materials. There should be more investigation on the correlation between crystallite properties including sizes, dimensions, and chemical stability.

The most obscured process of lead perovskite solar cell fabrication is how the active layer is constructed under solution-process. The bulk study in fibrous intermediates posed acid-catalysis as a method to disperse oriented crystalline lead perovskite crystallite islands. 2-D XRD measurements were a useful method to analyze the construction process. There still remains room for tuning the proper catalyst in this process.

This study is not restricted to lead perovskites, rather also related to similar systems such as tin perovskites,[111,112] germanium perovskites,[113] and tin chalcogenides.[114] Tin perovskites have exactly the same behavior as lead perovskite where a 2-D fibrous structure inter-converts with cubic or lower symmetry crystallographic phases. There are several germanium perovskites that are useful for application to opt-electronic devices. Those perovskites are still not well studied in terms of reaction pathways, however, poses worthiness for future investigation. Tin chalcogenides are well studied for their attractive properties for semiconductor materials.[115,116] These materials can be synthesized from a hydrazinium precursor that has similar structure to plumbate intermediates of **PV**.[114] These materials also need processing to form a nicely ordered form for practical application thus should be studied in terms of formation mechanism.

One mechanically notable difference between lead perovskites and tin perovskites is the necessity of solvent molecules in their fibrous crystals. The lead perovskite studied in this thesis need solvent molecules in its plumbate intermediates. On the other hand the tin counterpart does not require those. In this sense it is better described as another phase of the same material. This fact highlights that the distinctive kinetics seen in the conversion between intermediates (**INT-W**, **-F**, **-S**) and **PV** is due to intake and outtake of solvent molecules during the conversions. In the absence of intake and outtake the change is better described as phase transition. Thus I surmise that one of the reasons lead perovskite is so widely used is because the kinetics is slower than simple phase transition thus enabling the reaction controllable by modification of the procedure.

X-ray diffraction was proven to be a useful method for studies on crystal-to-crystal conversions. The methodology used in this study could be further applied to other crystal-to-crystal conversion systems especially solution-processable materials in which isolation of intermediates can be expected.

Overall, throughout the study on the chemistry of lead perovskite crystals I propose several future tasks. In the proximity of lead perovskite solar cells, there needs more effort to rationally control the formation process of lead perovskite crystals on flat substrates by solution process. The formation kinetics is controllable by chemical tuning of the removal of solvent molecules from the system. Mass production of solar cells requires more delicate control than laboratory scale production thus needs further effort. The ways to mitigate toxicity of lead should be addressed by considering the reversibility of **PV** formation process.

In the fields related to pure science, this study is a rare example of crystal-to-crystal conversion reactions. Since perovskite crystal structure is one of the commonest crystal structures of minerals, this study represents a good example of studies on mineral formation processes. Expansion of our understanding to the formation mechanism of other types of crystal structures will be a next step advocated by this study. Also, the concepts and techniques used here can be applied to crystal formation mechanism or order control of molecular functional materials.[117-128]

References

(1) Reinhoudt, D. N.; Crego-Calama, M. Synthesis Beyond the Molecule. *Science* **2002**, *295* (5564), 2403–2407.

(2) Takeuchi, T.; Amano, H.; Hiramatsu, K.; Sawaki, N.; Akasaki, I. Growth of Single Crystalline GaN Film on Si Substrate Using 3C-SiC as an Intermediate Layer. *Journal of Crystal Growth* **1991**, *115* (1-4), 634–638.

(3) Zhang, W.; Jin, W.; Fukushima, T.; Saeki, A.; Seki, S.; Aida, T. Supramolecular Linear Heterojunction Composed of Graphite-Like Semiconducting Nanotubular Segments. *Science* **2011**, *334* (6054), 340–343.

(4) Würthner, F. Supramolecular Polymerization: Living It Up. *Nature Chemistry* **2014**, *6* (3), 171–173.

(5) Zarzar, L. D.; Sresht, V.; Sletten, E. M.; Kalow, J. A.; Blankschtein, D.; Swager, T. M. Dynamically Reconfigurable Complex Emulsions via Tunable Interfacial Tensions. *Nature* **2015**, *518* (7540), 520–524.

(6) Negishi, E.-I.; Anastasia, L. Palladium-Catalyzed Alkynylation. *Chem. Rev.* **2003**, *103* (5), 1979–2018.

(7) Miyaura, N.; Suzuki, A. Palladium-Catalyzed Cross-Coupling Reactions of Organoboron Compounds. *Chem. Rev.* **1995**, *95* (7), 2457–2483.

(8) Chinchilla, R.; Nájera, C. The Sonogashira Reaction: a Booming Methodology in Synthetic Organic Chemistry †. *Chem. Rev.* **2007**, *107* (3), 874–922.

(9) King, A. O.; Okukado, N.; Negishi, E.-I. Highly General Stereo-, Regio-, and Chemo-Selective Synthesis of Terminal and Internal Conjugated Enynes by the Pd-Catalysed Reaction of Alkynylzinc Reagents with Alkenyl Halides. *J. Chem. Soc., Chem. Commun.* **1977**, No. 19, 683–684.

(10) Miyaura, N.; Yamada, K.; Suzuki, A. A New Stereospecific Cross-Coupling by the Palladium-Catalyzed Reaction of 1-Alkenylboranes with 1-Alkenyl or 1-Alkynyl Halides. *Tetrahedron Letters* **1979**, *20* (36), 3437–3440.

(11) Sonogashira, K.; Tohda, Y.; Hagihara, N. A Convenient Synthesis of Acetylenes: Catalytic Substitutions of Acetylenic Hydrogen with Bromoalkenes, Iodoarenes and Bromopyridines. *Tetrahedron Letters* **1975**, *16* (50), 4467–4470.

(12) Kittel. *Introduction to Solid State Physics*; John Wiley & Sons, 2007.

(13) Dang, M. T.; Hirsch, L.; Wantz, G.; Wuest, J. D. Controlling the Morphology and Performance of Bulk Heterojunctions in Solar Cells. Lessons Learned From the Benchmark Poly(3-Hexylthiophene):[6,6]-Phenyl-C61-Butyric Acid Methyl Ester System. *Chem. Rev.* **2013**, *113* (5), 3734–3765.

(14) Suryanarayana, C. *Mechanical Alloying and Milling*; CRC Press, 2004.

(15) Krishnan, B. P.; Sureshan, K. M. A Spontaneous Single-Crystal-to-Single-Crystal Polymorphic Transition Involving Major Packing Changes. *J. Am. Chem. Soc.* **2015**, *137* (4), 1692–1696.

(16) Hoshino, M.; Uchida, E.; Norikane, Y.; Azumi, R.; Nozawa, S.; Tomita, A.; Sato, T.; Adachi, S.-I.; Koshihara, S.-Y. Crystal Melting by Light: X-Ray Crystal Structure Analysis of an Azo Crystal Showing Photoinduced Crystal-Melt Transition. *J. Am. Chem. Soc.* **2014**, *136* (25), 9158–9164.

(17) Shang, R.; Wang, Z. M.; Gao, S. A 36-Fold Multiple Unit Cell and Switchable Anisotropic Dielectric Responses in an Ammonium Magnesium Formate Framework. *Angew. Chem. Int. Ed.* **2015**, *54* (8), 2534–2537.

(18) Dou, L.; Zheng, Y.; Shen, X.; Wu, G.; Fields, K.; Hsu, W. C.; Zhou, H.; Yang, Y.; Wudl, F. Single-Crystal Linear Polymers Through Visible Light-Triggered Topochemical Quantitative Polymerization. *Science* **2014**, *343* (6168), 272–277.

(19) McCammon, C. Perovskite as a Possible Sink for Ferric Iron in the Lower Mantle. *Nature* **1997**, *387* (6634), 694–696.

(20) Tschauner, O.; Ma, C.; Beckett, J. R.; Prescher, C.; Prakapenka, V. B.; Rossman, G. R. Mineralogy. Discovery of Bridgmanite, the Most Abundant Mineral in Earth, in a Shocked Meteorite. *Science* **2014**, *346* (6213), 1100–1102.

(21) Britvin, S. N.; Kashtanov, S. A.; Krzhizhanovskaya, M. G.; Gurinov, A. A.; Glumov, O. V.; Strekopytov, S.; Kretser, Y. L.; Zaitsev, A. N.; Chukanov, N. V.; Krivovichev, S. V. Perovskites with the Framework-Forming Xenon. *Angew. Chem. Int. Ed.* **2015**, *54* (48), 14340–14344.
(22) Zhu, Y.; Withers, R. L.; Bourgeois, L.; Dwyer, C.; Etheridge, J. Direct Mapping of Li-Enabled Octahedral Tilt Ordering and Associated Strain in Nanostructured Perovskites. *Nat Mater* **2015**, *14* (11), 1142–1149.
(23) Maeno, Y.; Hashimoto, H.; Yoshida, K.; Nishizaki, S.; Fujita, T.; Bednorz, J. G.; Lichtenberg, F. Superconductivity in a Layered Perovskite Without Copper. *Nature* **1994**, *372* (6506), 532–534.
(24) Ahn, K. H.; Lookman, T.; Bishop, A. R. Strain-Induced Metal–Insulator Phase Coexistence in Perovskite Manganites. *Nature* **2004**, *428* (6981), 401–404.
(25) Bousquet, E.; Dawber, M.; Stucki, N.; Lichtensteiger, C.; Hermet, P.; Gariglio, S.; Triscone, J.-M.; Ghosez, P. Improper Ferroelectricity in Perovskite Oxide Artificial Superlattices. *Nature* **2008**, *452* (7188), 732–736.
(26) Grinberg, I.; West, D. V.; Torres, M.; Gou, G.; Stein, D. M.; Wu, L.; Chen, G.; Gallo, E. M.; Akbashev, A. R.; Davies, P. K.; Spanier, J. E.; Rappe, A. M. Perovskite Oxides for Visible-Light-Absorbing Ferroelectric and Photovoltaic Materials. *Nature* **2013**, *503* (7477), 509–512.
(27) Chung, I.; Lee, B.; He, J.; Chang, R. P. H.; Kanatzidis, M. G. All-Solid-State Dye-Sensitized Solar Cells with High Efficiency. *Nature* **2012**, *485* (7399), 486–489.
(28) Wolfram, T.; Ellialtioglu, S. *Electronic and Optical Properties of D-Band Perovskites*; Cambridge University Press, 2006.
(29) Stoumpos, C. C.; Malliakas, C. D.; Kanatzidis, M. G. Semiconducting Tin and Lead Iodide Perovskites with Organic Cations: Phase Transitions, High Mobilities, and Near-Infrared Photoluminescent Properties. *Inorg. Chem.* **2013**, *52* (15), 9019–9038.
(30) Kojima, A.; Teshima, K.; Shirai, Y.; Miyasaka, T. Organometal Halide Perovskites as Visible-Light Sensitizers for Photovoltaic Cells. *J. Am. Chem. Soc.* **2009**, *131* (17), 6050–6051.
(31) Im, J.-H.; Lee, C.-R.; Lee, J.-W.; Park, S.-W.; Park, N.-G. 6.5% Efficient Perovskite Quantum-Dot-Sensitized Solar Cell. *Nanoscale* **2011**, *3* (10), 4088–4093.
(32) Kim, H.-S.; Lee, C.-R.; Im, J.-H.; Lee, K.-B.; Moehl, T.; Marchioro, A.; Moon, S.-J.; Humphry-Baker, R.; Yum, J.-H.; Moser, J.-E.; Grätzel, M.; Park, N.-G. Lead Iodide Perovskite Sensitized All-Solid-State Submicron Thin Film Mesoscopic Solar Cell with Efficiency Exceeding 9%. *Sci. Rep.* **2012**, *2*, 591.
(33) Etgar, L.; Gao, P.; Xue, Z.; Peng, Q.; Chandiran, A. K.; Liu, B.; Nazeeruddin, M. K.; Grätzel, M. Mesoscopic CH 3NH 3PbI 3/TiO 2Heterojunction Solar Cells. *J. Am. Chem. Soc.* **2012**, *134* (42), 17396–17399.
(34) Lee, M. M.; Teuscher, J.; Miyasaka, T.; Murakami, T. N.; Snaith, H. J. Efficient Hybrid Solar Cells Based on Meso-Superstructured Organometal Halide Perovskites. *Science* **2012**, *338* (6107), 643–647.
(35) Møller, C. K. A Phase Transition in Cæsium Plumbochloride. *Nature* **1957**, *180* (4593), 981–982.
(36) Ishihara, T.; Takahashi, J.; Goto, T. Optical Properties Due to Electronic Transitions in Two-Dimensional Semiconductors (CnH2n+1NH3)2PbI4. *Phys. Rev., B Condens. Matter* **1990**, *42* (17), 11099–11107.
(37) Onoda-Yamamuro, N.; Matsuo, T.; Suga, H. Calorimetric and IR Spectroscopic Studies of Phase Transitions in Methylammonium Trihalogenoplumbates (II)†. *Journal of Physics and Chemistry of Solids* **1990**, *51* (12), 1383–1395.
(38) Xu, Q.; Eguchi, T.; Nakayama, H.; Nakamura, N.; Kishita, M. Molecular Motions and Phase Transitions in Solid CH3NH3PbX3 (X = C1, Br, I) as Studied by NMR and NQR. *Zeitschrift für Naturforschung A* **1991**, *46* (3), 240–246.
(39) Xu, Q.; Eguchi, T.; Nakayama, H. Molecular Motions in Solid CD3NH3PbBr3 as

Studied by 1H NMR. *Bull. Chem. Soc. Jpn.* **1992**, *65* (8), 2264–2266.
(40) Onoda-Yamamuro, N.; Yamamuro, O.; Matsuo, T.; Suga, H. P-T Phase Relations of CH3NH3PbX3 (X = Cl, Br, I) Crystals. *Journal of Physics and Chemistry of Solids* **1992**, *53* (2), 277–281.
(41) Onoda-Yamamuro, N.; Matsuo, T.; Suga, H. Dielectric Study of CH3NH3PbX3 (X = Cl, Br, I). *Journal of Physics and Chemistry of Solids* **1992**, *53* (7), 935–939.
(42) Mitzi, D. B.; Feild, C. A.; Harrison, W. T. A.; Guloy, A. M. Conducting Tin Halides with a Layered Organic-Based Perovskite Structure. *Nature* **1994**, *369* (6480), 467–469.
(43) Lee, Y.; Mitzi, D. B.; Barnes, P. W.; Vogt, T. Pressure-Induced Phase Transitions and Templating Effect in Three-Dimensional Organic-Inorganic Hybrid Perovskites. *Phys. Rev., B Condens. Matter* **2003**, *68* (2), 020103.
(44) McPherson, A. *Introduction to Macromolecular Crystallography*; John Wiley & Sons, Inc.: Hoboken, NJ, USA, 2009.
(45) Als-Nielsen, J.; McMorrow, D. *Elements of Modern X-Ray Physics*; John Wiley & Sons, Inc.: Hoboken, NJ, USA, 2011.
(46) Run Liu; Alexey A Vertegel; Eric W Bohannan; Thomas A Sorenson, A.; Switzer, J. A. Epitaxial Electrodeposition of Zinc Oxide Nanopillars on Single-Crystal Gold. *Chem. Mater.* **2001**, *13* (2), 508–512.
(47) Ueda, K.; Hase, T.; Yanagi, H.; Kawazoe, H.; Hosono, H.; Ohta, H.; Orita, M.; Hirano, M. Epitaxial Growth of Transparent P-Type Conducting CuGaO2 Thin Films on Sapphire (001) Substrates by Pulsed Laser Deposition. *J. Appl. Phys.* **2001**, *89* (3), 1790–1793.
(48) Roe, R. J.; Krigbaum, W. R. Description of Crystallite Orientation in Polycrystalline Materials Having Fiber Texture. *J. Chem. Phys.* **1964**, *40* (9), 2608.
(49) Li, W.; Hendriks, K. H.; Wienk, M. M.; Janssen, R. A. J. Diketopyrrolopyrrole Polymers for Organic Solar Cells. *Acc. Chem. Res.* **2016**, *49* (1), 78–85.
(50) Unger, E. L.; Bowring, A. R.; Tassone, C. J.; Pool, V. L.; Gold-Parker, A.; Cheacharoen, R.; Stone, K. H.; Hoke, E. T.; Toney, M. F.; McGehee, M. D. Chloride in Lead Chloride-Derived Organo-Metal Halides for Perovskite-Absorber Solar Cells. *Chem. Mater.* **2014**, *26* (24), 7158–7165.
(51) Yang, Y. M.; Chen, W.; Dou, L.; Chang, W.-H.; Duan, H. S.; Bob, B.; Li, G.; Yang, Y. High-Performance Multiple-Donor Bulk Heterojunction Solar Cells. *Nature Photon* **2015**.
(52) Guo, X.; Zhou, N.; Lou, S. J.; Smith, J.; Tice, D. B.; Hennek, J. W.; Ortiz, R. P.; Navarrete, J. T. L.; Li, S.; Strzalka, J.; Chen, L. X.; Chang, R. P. H.; Facchetti, A.; Marks, T. J. Polymer Solar Cells with Enhanced Fill Factors. *Nature Photon* **2013**, –.
(53) Lu, L.; Xu, T.; Chen, W.; Landry, E. S.; Yu, L. Ternary Blend Polymer Solar Cells with Enhanced Power Conversion Efficiency. *Nature Photon* **2014**, *8* (9), 716–722.
(54) Cruickshank, A. C.; Dotzler, C. J.; Din, S.; Heutz, S.; Toney, M. F.; Ryan, M. P. The Crystalline Structure of Copper Phthalocyanine Films on ZnO($1\bar{1}00$). *J. Am. Chem. Soc.* **2012**, *134* (35), 14302–14305.
(55) Fewster, P. F. Reciprocal Space Mapping. *Critical Reviews in Solid State and Materials Sciences* **1997**, *22* (2), 69–110.
(56) Salzmann, I.; Nabok, D.; Oehzelt, M.; Duhm, S.; Moser, A.; Heimel, G.; Puschnig, P.; Ambrosch-Draxl, C.; Rabe, J. P.; Koch, N. Structure Solution of the 6,13-Pentacenequinone Surface-Induced Polymorph by Combining X-Ray Diffraction Reciprocal-Space Mapping and Theoretical Structure Modeling. *Crystal Growth & Design* **2011**, *11* (2), 600–606.
(57) Terpstra, P.; Westenbrink, H. G. On the Crystal-Structure of Lead-Iodide. *Proceedings of the Koninklijke Nederlandse Academie van Wetenschappen* **1926**, *29*, 431–442.
(58) Heo, J. H.; Im, S. H.; Noh, J. H.; Mandal, T. N.; Lim, C.-S.; Chang, J. A.; Lee, Y.

H.; Kim, H.-J.; Sarkar, A.; Nazeeruddin, M. K.; Grätzel, M.; Seok, Il, S. Efficient Inorganic-Organic Hybrid Heterojunction Solar Cells Containing Perovskite Compound and Polymeric Hole Conductors. *Nature Photon* **2013**, *7* (6), 486–491.

(59) Burschka, J.; Pellet, N.; Moon, S.-J.; Humphry-Baker, R.; Gao, P.; Nazeeruddin, M. K.; Grätzel, M. Sequential Deposition as a Route to High-Performance Perovskite-Sensitized Solar Cells. *Nature* **2013**, *499* (7458), 316–319.

(60) Liu, M.; Johnston, M. B.; Snaith, H. J. Efficient Planar Heterojunction Perovskite Solar Cells by Vapour Deposition. *Nature* **2013**, *501* (7467), 395–398.

(61) Miyamae, H.; Numahata, Y.; Nagata, M. The Crystal Structure of Lead(II) Iodide-Dimethylsulphoxide(1/2), PbI2(Dmso)2. *Chem. Lett.* **1980**, *9* (6), 663–664.

(62) Wakamiya, A.; Endo, M.; Sasamori, T.; Tokitoh, N.; Ogomi, Y.; Hayase, S.; Murata, Y. Reproducible Fabrication of Efficient Perovskite-Based Solar Cells: X-Ray Crystallographic Studies on the Formation of CH3NH3PbI3 Layers. *Chem. Lett.* **2014**, *43* (5), 711–713.

(63) Hao, F.; Stoumpos, C. C.; Liu, Z.; Chang, R. P. H.; Kanatzidis, M. G. Controllable Perovskite Crystallization at a Gas-Solid Interface for Hole Conductor-Free Solar Cells with Steady Power Conversion Efficiency Over 10%. *J. Am. Chem. Soc.* **2014**, *136* (46), 16411–16419.

(64) Jeon, N. J.; Noh, J. H.; Kim, Y. C.; Yang, W. S.; Ryu, S.; Seok, S. I. Solvent Engineering for High-Performance Inorganic-Organic Hybrid Perovskite Solar Cells. *Nat Mater* **2014**, *13* (9), 897–903.

(65) Christians, J. A.; Fung, R. C. M.; Kamat, P. V. An Inorganic Hole Conductor for Organo-Lead Halide Perovskite Solar Cells. Improved Hole Conductivity with Copper Iodide. *J. Am. Chem. Soc.* **2014**, *136* (2), 758–764.

(66) Jeon, N. J.; Lee, J.; Noh, J. H.; Nazeeruddin, M. K.; Grätzel, M.; Seok, S. I. Efficient Inorganic-Organic Hybrid Perovskite Solar Cells Based on Pyrene Arylamine Derivatives as Hole-Transporting Materials. *J. Am. Chem. Soc.* **2013**, *135* (51), 19087–19090.

(67) Zhu, Z.; Ma, J.; Wang, Z.; Mu, C.; Fan, Z.; Du, L.; Bai, Y.; Fan, L.; Yan, H.; Phillips, D. L.; Yang, S. Efficiency Enhancement of Perovskite Solar Cells Through Fast Electron Extraction: the Role of Graphene Quantum Dots. *J. Am. Chem. Soc.* **2014**, *136* (10), 3760–3763.

(68) Mei, A.; Li, X.; Liu, L.; Ku, Z.; Liu, T.; Rong, Y.; Xu, M.; Hu, M.; Chen, J.; Yang, Y.; Gratzel, M.; Han, H. A Hole-Conductor-Free, Fully Printable Mesoscopic Perovskite Solar Cell with High Stability. *Science* **2014**, *345* (6194), 295–298.

(69) Gutmann, V. *The Donor-Acceptor Approach to Molecular Interactions*; Plenum Publishing Corporation, 1978.

(70) Watson, J. D.; CRICK, F. H. C. Molecular Structure of Nucleic Acids: a Structure for Deoxyribose Nucleic Acid. *Nature* **1953**, *171* (4356), 737–738.

(71) Sheldrick, G. M. Crystal Structure Refinement with SHELXL. *Acta Crystallogr C Struct Chem* **2015**, *71* (Pt 1), 3–8.

(72) Kabuto, C.; AKINE, S.; NEMOTO, T.; Kwon, E. Release of Software (Yadokari-XG 2009) for Crystal Structure Analyses. *Nihon Kessho Gakkaishi* **2009**, *51* (3), 218–224.

(73) Noh, J. H.; Im, S. H.; Heo, J. H.; Mandal, T. N.; Seok, S. I. Chemical Management for Colorful, Efficient, and Stable Inorganic–Organic Hybrid Nanostructured Solar Cells. *Nano Lett.* **2013**, *13* (4), 1764–1769.

(74) Eperon, G. E.; Burlakov, V. M.; Docampo, P.; Goriely, A.; Snaith, H. J. Morphological Control for High Performance, Solution-Processed Planar Heterojunction Perovskite Solar Cells. *Adv. Funct. Mater.* **2013**, *24* (1), 151–157.

(75) Leijtens, T.; Eperon, G. E.; Pathak, S.; Abate, A.; Lee, M. M.; Snaith, H. J. Overcoming Ultraviolet Light Instability of Sensitized TiO2 with Meso-Superstructured Organometal Tri-Halide Perovskite Solar Cells. *Nat Comms* **2013**, *4*, –.

(76) Zhao, Y.; Zhu, K. Optical Bleaching of Perovskite (CH3NH3)PbI3 Through

Room-Temperature Phase Transformation Induced by Ammonia. *Chem. Commun.* **2014**, *50* (13), 1605–1607.
(77) Smith, I. C.; Hoke, E. T.; Solis-Ibarra, D.; McGehee, M. D.; Karunadasa, H. I. A Layered Hybrid Perovskite Solar-Cell Absorber with Enhanced Moisture Stability. *Angew. Chem. Int. Ed.* **2014**, *53* (42), 11232–11235.
(78) Zhou, H.; Chen, Q.; Li, G.; Luo, S.; Song, T. B.; Duan, H. S.; Hong, Z.; You, J.; Liu, Y.; Yang, Y. Interface Engineering of Highly Efficient Perovskite Solar Cells. *Science* **2014**, *345* (6196), 542–546.
(79) Hanusch, F. C.; Wiesenmayer, E.; Mankel, E.; Binek, A.; Angloher, P.; Fraunhofer, C.; Giesbrecht, N.; Feckl, J. M.; Jaegermann, W.; Johrendt, D.; Bein, T.; Docampo, P. Efficient Planar Heterojunction Perovskite Solar Cells Based on Formamidinium Lead Bromide. *J. Phys. Chem. Lett.* **2014**, *5* (16), 2791–2795.
(80) Gong, X.; Li, M.; Shi, X.-B.; Ma, H.; Wang, Z.-K.; Liao, L.-S. Controllable Perovskite Crystallization by Water Additive for High-Performance Solar Cells. *Adv. Funct. Mater.* **2015**, *25* (42), 6671–6678.
(81) Leguy, A. M. A.; Hu, Y.; Campoy-Quiles, M.; Alonso, M. I.; Weber, O. J.; Azarhoosh, P.; van Schilfgaarde, M.; Weller, M. T.; Bein, T.; Nelson, J.; Docampo, P.; Barnes, P. R. F. Reversible Hydration of CH3NH3PbI3 in Films, Single Crystals, and Solar Cells. *Chem. Mater.* **2015**, *27* (9), 3397–3407.
(82) Eperon, G. E.; Habisreutinger, S. N.; Leijtens, T.; Bruijnaers, B. J.; van Franeker, J. J.; deQuilettes, D. W.; Pathak, S.; Sutton, R. J.; Grancini, G.; Ginger, D. S.; Janssen, R. A. J.; Petrozza, A.; Snaith, H. J. The Importance of Moisture in Hybrid Lead Halide Perovskite Thin Film Fabrication. *ACS Nano* **2015**, *9* (9), 9380–9393.
(83) Jiang, Q.; Rebollar, D.; Gong, J.; Piacentino, E. L.; Zheng, C.; Xu, T. Pseudohalide-Induced Moisture Tolerance in Perovskite CH3 NH3 Pb(SCN)2 I Thin Films. *Angew. Chem. Int. Ed.* **2015**, *54* (26), 7617–7620.
(84) Daub, M.; Hillebrecht, H. Synthesis, Single-Crystal Structure and Characterization of (CH3 NH3)2 Pb(SCN)2 I2. *Angew. Chem. Int. Ed.* **2015**, *54* (38), 11016–11017.
(85) Allen, F. H.; Kennard, O.; Watson, D. G.; Brammer, L.; Orpen, A. G.; Taylor, R. Tables of Bond Lengths Determined by X-Ray and Neutron Diffraction. Part 1. Bond Lengths in Organic Compounds. *J. Chem. Soc., Perkin Trans. 2* **1987**, No. 12, S1–S19.
(86) Uddin, N.; Choi, T. H.; Choi, C. H. Direct Absolute P KaPredictions and Proton Transfer Mechanisms of Small Molecules in Aqueous Solution by QM/MM-MD. *J. Phys. Chem. B* **2013**, *117* (20), 6269–6275.
(87) Chen, Y.; Zhao, Y.; Liang, Z. Non-Thermal Annealing Fabrication of Efficient Planar Perovskite Solar Cells with Inclusion of NH 4Cl. *Chem. Mater.* **2015**, *27* (5), 1448–1451.
(88) Mohammad K, N.; Gao, P.; Grätzel, M. Organohalide Lead Perovskites for Photovoltaic Applications. *Energy Environ. Sci.* **2014**, *7* (8), 2448–2463.
(89) Zhao, Y.; Zhu, K. Efficient Planar Perovskite Solar Cells Based on 1.8 eV Band Gap CH3NH3PbI2Br Nanosheets via Thermal Decomposition. *J. Am. Chem. Soc.* **2014**, *136* (35), 12241–12244.
(90) Zhang, W.; Saliba, M.; Moore, D. T.; Pathak, S. K.; Hörantner, M. T.; Stergiopoulos, T.; Stranks, S. D.; Eperon, G. E.; Alexander-Webber, J. A.; Abate, A.; Sadhanala, A.; Yao, S.; Chen, Y.; Friend, R. H.; Estroff, L. A.; Wiesner, U.; Snaith, H. J. Ultrasmooth Organic–Inorganic Perovskite Thin-Film Formation and Crystallization for Efficient Planar Heterojunction Solar Cells. *Nat Comms* **2015**, *6*, 6142.
(91) Chen, W.; Wu, Y.; Yue, Y.; Liu, J.; Zhang, W.; Yang, X.; Chen, H.; Bi, E.; Ashraful, I.; Grätzel, M.; Han, L. Efficient and Stable Large-Area Perovskite Solar Cells with Inorganic Charge Extraction Layers. *Science* **2015**, aad1015.
(92) Li, X.; Ibrahim Dar, M.; Yi, C.; Luo, J.; Tschumi, M.; Zakeeruddin, S. M.; Nazeeruddin, M. K.; Han, H.; Grätzel, M. Improved Performance and Stability of

Perovskite Solar Cells by Crystal Crosslinking with Alkylphosphonic Acid Ω-Ammonium Chlorides. *Nature Chemistry* **2015**, *7* (9), 703–711.
(93) You, J.; Meng, L.; Song, T. B.; Guo, T.-F.; Yang, Y. M.; Chang, W.-H.; Hong, Z.; Chen, H.; Zhou, H.; Chen, Q.; Liu, Y.; De Marco, N.; Yang, Y. Improved Air Stability of Perovskite Solar Cells via Solution-Processed Metal Oxide Transport Layers. *Nature Nanotech* **2016**, *11* (1), 75–81.
(94) Leijtens, T.; Eperon, G. E.; Noel, N. K.; Habisreutinger, S. N.; Petrozza, A.; Snaith, H. J. Stability of Metal Halide Perovskite Solar Cells. *Adv. Energy Mater.* **2015**, *5* (20), n/a–n/a.
(95) Stranks, S. D.; Nayak, P. K.; Zhang, W.; Stergiopoulos, T.; Snaith, H. J. Formation of Thin Films of Organic-Inorganic Perovskites for High-Efficiency Solar Cells. *Angew. Chem. Int. Ed. Engl.* **2015**, *54* (11), 3240–3248.
(96) Stranks, S. D.; Eperon, G. E.; Grancini, G.; Menelaou, C.; Alcocer, M. J. P.; Leijtens, T.; Herz, L. M.; Petrozza, A.; Snaith, H. J. Electron-Hole Diffusion Lengths Exceeding 1 Micrometer in an Organometal Trihalide Perovskite Absorber. *Science* **2013**, *342* (6156), 341–344.
(97) You, J.; Hong, Z.; Yang, Y. M.; Chen, Q.; Cai, M.; Song, T. B.; Chen, C.-C.; Lu, S.; Liu, Y.; Zhou, H.; Yang, Y. Low-Temperature Solution-Processed Perovskite Solar Cells with High Efficiency and Flexibility. *ACS Nano* **2014**, *8* (2), 1674–1680.
(98) Tidhar, Y.; Edri, E.; Weissman, H.; Zohar, D.; Hodes, G.; Cahen, D.; Rybtchinski, B.; Kirmayer, S. Crystallization of Methyl Ammonium Lead Halide Perovskites: Implications for Photovoltaic Applications. *J. Am. Chem. Soc.* **2014**, *136* (38), 13249–13256.
(99) Guo, Y.; Liu, C.; Inoue, K.; Harano, K.; Tanaka, H.; Nakamura, E. Enhancement in the Efficiency of an Organic–Inorganic Hybrid Solar Cell with a Doped P3HT Hole-Transporting Layer on a Void-Free Perovskite Active Layer. *J. Mater. Chem. A* **2014**, *2* (34), 13827–13830.
(100) Weller, M. T.; Weber, O. J.; Henry, P. F.; Di Pumpo, A. M.; Hansen, T. C. Complete Structure and Cation Orientation in the Perovskite Photovoltaic Methylammonium Lead Iodide Between 100 and 352 K. *Chem. Commun.* **2015**, *51* (20), 4180–4183.
(101) Leguy, A. M. A.; Frost, J. M.; McMahon, A. P.; Sakai, V. G.; Kochelmann, W.; Law, C.; Li, X.; Foglia, F.; Walsh, A.; O'Regan, B. C.; Nelson, J.; Cabral, J. T.; Barnes, P. R. F. The Dynamics of Methylammonium Ions in Hybrid Organic-Inorganic Perovskite Solar Cells. *Nat Comms* **2015**, *6*, 7124.
(102) Guo, Y.; Liu, C.; Tanaka, H.; Nakamura, E. Air-Stable and Solution-Processable Perovskite Photodetectors for Solar-Blind UV and Visible Light. *J. Phys. Chem. Lett.* **2015**, *6* (3), 535–539.
(103) Quarti, C.; Mosconi, E.; Ball, J. M.; D'Innocenzo, V.; Tao, C.; Pathak, S.; Snaith, H. J.; Petrozza, A.; De Angelis, F. Structural and Optical Properties of Methylammonium Lead Iodide Across the Tetragonal to Cubic Phase Transition: Implications for Perovskite Solar Cells. *Energy Environ. Sci.* **2016**, *9* (1), 155–163.
(104) Grancini, G.; Marras, S.; Prato, M.; Giannini, C.; Quarti, C.; De Angelis, F.; De Bastiani, M.; Eperon, G. E.; Snaith, H. J.; Manna, L.; Petrozza, A. The Impact of the Crystallization Processes on the Structural and Optical Properties of Hybrid Perovskite Films for Photovoltaics. *J. Phys. Chem. Lett.* **2014**, *5* (21), 3836–3842.
(105) Zhou, Y.; Vasiliev, A. L.; Wu, W.; Yang, M.; Pang, S.; Zhu, K.; Padture, N. P. Crystal Morphologies of Organolead Trihalide in Mesoscopic/Planar Perovskite Solar Cells. *J. Phys. Chem. Lett.* **2015**, *6* (12), 2292–2297.
(106) Nie, W.; Tsai, H.; Asadpour, R.; Blancon, J.-C.; Neukirch, A. J.; Gupta, G.; Crochet, J. J.; Chhowalla, M.; Tretiak, S.; Alam, M. A.; Wang, H.-L.; Mohite, A. D. High-Efficiency Solution-Processed Perovskite Solar Cells with Millimeter-Scale Grains. *Science* **2015**, *347* (6221), 522–525.
(107) Dong, Q.; Fang, Y.; Shao, Y.; Mulligan, P.; Qiu, J.; Cao, L.; Huang, J. Electron-

Hole Diffusion Lengths > 175 Mm in Solution-Grown CH3NH3PbI3 Single Crystals. *Science* **2015**, *347* (6225), 967–970.
(108) Yang, W. S.; Noh, J. H.; Jeon, N. J.; Kim, Y. C.; Ryu, S.; Seo, J.; Seok, S. I. High-Performance Photovoltaic Perovskite Layers Fabricated Through Intramolecular Exchange. *Science* **2015**.
(109) Rivnay, J.; Mannsfeld, S. C. B.; Miller, C. E.; Salleo, A.; Toney, M. F. Quantitative Determination of Organic Semiconductor Microstructure From the Molecular to Device Scale. *Chem. Rev.* **2012**, *112* (10), 5488–5519.
(110) Yang, B.; Dyck, O.; Poplawsky, J.; Keum, J.; Puretzky, A.; Das, S.; Ivanov, I.; Rouleau, C.; Duscher, G.; Geohegan, D.; Xiao, K. Perovskite Solar Cells with Near 100% Internal Quantum Efficiency Based on Large Single Crystalline Grains and Vertical Bulk Heterojunctions. *J. Am. Chem. Soc.* **2015**, *137* (29), 9210–9213.
(111) Chung, I.; Song, J.-H.; Im, J.; Androulakis, J.; Malliakas, C. D.; Li, H.; Freeman, A. J.; Kenney, J. T.; Kanatzidis, M. G. CsSnI 3: Semiconductor or Metal? High Electrical Conductivity and Strong Near-Infrared Photoluminescence From a Single Material. High Hole Mobility and Phase-Transitions. *J. Am. Chem. Soc.* **2012**, *134* (20), 8579–8587.
(112) Hao, F.; Stoumpos, C. C.; Cao, D. H.; Chang, R. P. H.; Kanatzidis, M. G. Lead-Free Solid-State Organic–Inorganic Halide Perovskite Solar Cells. *Nature Photon* **2014**, *8* (6), 489–494.
(113) Stoumpos, C. C.; Frazer, L.; Clark, D. J.; Kim, Y. S.; Rhim, S. H.; Freeman, A. J.; Ketterson, J. B.; Jang, J. I.; Kanatzidis, M. G. Hybrid Germanium Iodide Perovskite Semiconductors: Active Lone Pairs, Structural Distortions, Direct and Indirect Energy Gaps, and Strong Nonlinear Optical Properties. *J. Am. Chem. Soc.* **2015**, *137* (21), 6804–6819.
(114) Mitzi, D. B.; Kosbar, L. L.; Murray, C. E.; Copel, M.; Afzali, A. High-Mobility Ultrathin Semiconducting Films Prepared by Spin Coating. *Nature* **2004**, *428* (6980), 299–303.
(115) Huang, Y.; Sutter, E.; Sadowski, J. T.; Cotlet, M.; Monti, O. L. A.; Racke, D. A.; Neupane, M. R.; Wickramaratne, D.; Lake, R. K.; Parkinson, B. A.; Sutter, P. Tin Disulfide—an Emerging Layered Metal Dichalcogenide Semiconductor: Materials Properties and Device Characteristics. *ACS Nano* **2014**, *8* (10), 10743–10755.
(116) Sun, Y.; Cheng, H.; Gao, S.; Sun, Z.; Liu, Q.; Liu, Q.; Lei, F.; Yao, T.; He, J.; Wei, S.; Xie, Y. Freestanding Tin Disulfide Single‐Layers Realizing Efficient Visible‐Light Water Splitting. *Angew. Chem. Int. Ed.* **2012**, *51* (35), 8727–8731.
(117) Desiraju, G. R.; Gavezzotti, A. Crystal Structures of Polynuclear Aromatic Hydrocarbons. Classification, Rationalization and Prediction From Molecular Structure. *Acta Crystallogr B* **1989**, *45* (5), 473–482.
(118) Goddard, R.; Haenel, M. W.; Herndon, W. C.; Krueger, C.; Zander, M. Crystallization of Large Planar Polycyclic Aromatic Hydrocarbons: the Molecular and Crystal Structures of Hexabenzo [Bc, Ef, Hi, Kl, No, Qr] Coronene and Benzo [1, 2, 3-Bc: 4, 5, 6-B“C”] Dicoronene. *J. Am. Chem. Soc.* **1995**, *117* (1), 30–41.
(119) Arjona-Esteban, A.; Krumrain, J.; Liess, A.; Stolte, M.; Huang, L.; Schmidt, D.; Stepanenko, V.; Gsänger, M.; Hertel, D.; Meerholz, K.; Würthner, F. Influence of Solid-State Packing of Dipolar Merocyanine Dyes on Transistor and Solar Cell Performances. *J. Am. Chem. Soc.* **2015**, *137* (42), 13524–13534.
(120) He, T.; Stolte, M.; Burschka, C.; Hansen, N. H.; Musiol, T.; Kälblein, D.; Pflaum, J.; Tao, X.; Brill, J.; Würthner, F. Single-Crystal Field-Effect Transistors of New Cl2-NDI Polymorph Processed by Sublimation in Air. *Nat Comms* **2015**, *6*, 5954.
(121) Yue, W.; Suraru, S.-L.; Bialas, D.; Müller, M.; Würthner, F. Synthesis and Properties of a New Class of Fully Conjugated Azahexacene Analogues. *Angew. Chem. Int. Ed.* **2014**, *53* (24), 6159–6162.
(122) Hayashi, S.; Koizumi, T. Elastic Organic Crystals of a Fluorescent Π-Conjugated Molecule. *Angew. Chem. Int. Ed.* **2016**, *55* (8), 2701–2704.
(123) Panda, M. K.; Ghosh, S.; Yasuda, N.; Moriwaki, T.; Mukherjee, G. D.; Reddy, C.

M.; Naumov, P. Spatially Resolved Analysis of Short-Range Structure Perturbations in a Plastically Bent Molecular Crystal. *Nature Chemistry* **2015**, *7* (1), 65–72.

(124) Yang, J.; Hu, W.; Usvyat, D.; Matthews, D.; Schutz, M.; Chan, G. K. L. Ab Initio Determination of the Crystalline Benzene Lattice Energy to Sub-Kilojoule/Mole Accuracy. *Science* **2014**, *345* (6197), 640–643.

(125) Park, C.; Park, J. E.; Choi, H. C. Crystallization-Induced Properties From Morphology-Controlled Organic Crystals. *Acc. Chem. Res.* **2014**, *47* (8), 2353–2364.

(126) Miller, N. C.; Cho, E.; Junk, M. J. N.; Gysel, R.; Risko, C.; Kim, D.; Sweetnam, S.; Miller, C. E.; Richter, L. J.; Kline, R. J.; Heeney, M.; McCulloch, I.; Amassian, A.; Acevedo-Feliz, D.; Knox, C.; Hansen, M. R.; Dudenko, D.; Chmelka, B. F.; Toney, M. F.; Brédas, J.-L.; McGehee, M. D. Use of X-Ray Diffraction, Molecular Simulations, and Spectroscopy to Determine the Molecular Packing in a Polymer-Fullerene Bimolecular Crystal. *Adv. Mater. Weinheim* **2012**, *24* (45), 6071–6079.

(127) Bürckstümmer, H.; Tulyakova, E. V.; Deppisch, M.; Lenze, M. R.; Kronenberg, N. M.; Gsänger, M.; Stolte, M.; Meerholz, K.; Würthner, F. Efficient Solution-Processed Bulk Heterojunction Solar Cells by Antiparallel Supramolecular Arrangement of Dipolar Donor-Acceptor Dyes. *Angew. Chem. Int. Ed.* **2011**, *50* (49), 11628–11632.

(128) Okamoto, T.; Nakahara, K.; Saeki, A.; Seki, S.; Oh, J. H.; Akkerman, H. B.; Bao, Z.; Matsuo, Y. Aryl−Perfluoroaryl Substituted Tetracene: Induction of Face-to-Face Π−Π Stacking and Enhancement of Charge Carrier Properties. *Chem. Mater.* **2011**, *23* (7), 1646–1649.

List of Publications

<Publications related to this thesis>

(1) Guo, Y.; Shoyama, K.; Sato, W.; Matsuo, Y.; Inoue, K.; Harano, K.; Liu, C.; Tanaka, H.; Nakamura, E. Chemical Pathways Connecting Lead(II) Iodide and Perovskite via Polymeric Plumbate(II) Fiber. *J. Am. Chem. Soc.* **2015**, *137* (50), 15907–15914.

(2) Guo, Y.; Shoyama, K.; Sato, W.; Nakamura, E. Polymer Stabilization of Lead(II) Perovskite Cubic Nanocrystals for Semitransparent Solar Cells. *Adv. Energy Mater.* **2016**, *6*, DOI: 10.1002/aenm.201502317.

<Publication not related to this thesis>

(1) Mitsui, C.; Soeda, J.; Miwa, K.; Shoyama, K.; Ota, Y.; Tsuji, H.; Takeya, J.; Nakamura, E. Single-Crystal Organic Field-Effect Transistors of Naphthodifurans. *Bull. Chem. Soc. Jpn.* **2015**, *88* (6), 776–783.